Durham E-Theses

X'ray scattering from thin films and interfaces

Clarke, John

How to cite:

Clarke, John (1999) *X'ray scattering from thin films and interfaces*, Durham theses, Durham University. Available at Durham E-Theses Online: http://etheses.dur.ac.uk/4499/

X-Ray Scattering from Thin Films and Interfaces

by

John Clarke

A thesis submitted in partial fulfilment of the requirements
for the degree of Doctor of Philosophy

The University of Durham

1999

1 0 APR 2000

Abstract

The non-destructive study and characterisation of thin films and their interfaces, on an atomic scale, is a crucially important area of study in many areas of science and technology. In this thesis both high angle and grazing incidence x-ray scattering techniques have been used to study the effect of depositing thin films on surfaces with a periodic roughness, as well as studying the structure of laterally modulated surfaces themselves.

High angle diffraction measurements of the out-of-plane size of Co crystallites and the crystalline texture of the Ag lattice, in a series of CoAg granular films, has allowed a consistent growth mechanism for the Co grains to be deduced. In grazing incidence scattering studies of this series of thin, granular films it was observed that the diffuse scatter was offset from the specular condition and the position of this offset was seen to vary, sinusoidally, upon rotation of the sample. This led to the conclusion that the growth techniques employed had caused a regular step-bunching of the Si (111) substrate. As step-bunching of surfaces can affect greatly the properties of thin films deposited on them, the ability to characterise the substrate after growth is extremely important.

In spin-valves deposited on rough, tiled, silicon oxide substrates, the presence of strong interference fringes in the off-specular scatter demonstrated that vertically conformal roughness dominated the system and this was seen to result in the degradation of the magnetic sensitivity of the samples. Conversely, an enhancement in the photoluminescence from thin polymer films deposited on laterally modulated substrates led to a series of studies being made on such structures. In order to obtain information on the lateral period of such structures, as well as their roughness and thickness, existing scattering theories have been modified and a semi-kinematical code of the coherent scatter has been developed.

<u>Acknowledgements</u>

Welcome to the most read part of any thesis where, in time honoured tradition, I am able to thank all the people who have helped me over the last three years of study.

Firstly I'd like to thank my supervisor, Brian Tanner. It has been an education and pleasure to work with him for the last few years and I thank him for all the work he has put into helping me. I would also like to thank him in his capacity as head of department for providing me with all the excellent facilities of the Physics Department.

Secondly I'd especially like to thank the rest of the x-ray group for their help and friendship. Tom Hase and Ian Pape for helping me in so many areas throughout my three years and in particular Brian Fulthorpe for a plethora of shared experiences throughout our parallel track PhDs, my memory of that Bratislavian bus stop and subsequent high security accommodation will remain with me for years to come! Thanks also to Andrea Li-Bassi, Andrea Amici and Marco Poli for adding the 'Italian touch' to the group and the other erstwhile members of the x-ray crowd Amir Rozatian, Sujit Halder, Peter Hatton, Yixi Su, Guangming Luo, Stewart Wilkins and Megan Hogan.

A lot of the work presented in this thesis has been carried out in collaboration with other Universities. Special thanks go to Chris Marrows, Brian Hickey and Fay Stanley from Leeds and Matthias Gester and Sarah Thompson from York for all their help with the magnetic data taken in chapters 4 and 6 respectively. Special thanks also to Ian Pape, now at the ESRF, Grenoble, and Matt Wormington of Bede Scientific for all their help with the work in chapter 7. Thanks also to the many people who have helped out during visits to various synchrotron sources, in particular Chiu Tang and Steve Collins from Daresbury and Simon Brown, Paul Thompson, Gavin Vaughan, Andy Fitch and Eric Dooryhee from the ESRF.

Thanks must also go to the rest of the condensed matter group who have helped make my stay in physics a slightly more sane one. They are (or were) in reverse order of

List of Publications

Some of the work presented in this thesis has been published and appears in the following :-

Chapter 5 - *Influence of Step-Bunching on Grazing Incidence Diffuse X-Ray Scattering* - **J. Clarke**, I. Pape, B. K. Tanner and M. Wormington J. Phys. C **11** *2661* (1999)

Chapter 6 - *The Effect of Conformal Roughness on Spin-Valves* - **J. Clarke**, C. H. Marrows, F. E. Stanley, R. J. T. Bunyan, B. K. Tanner and B. J. Hickey J. Phys. D **32** *1169* (1999)

Declaration

I hearby declare that the work contained within this thesis is my own and has not been submitted previously for any other degree.

Much of the work presented in this thesis has been carried out as part of collaborations with other Universities and their contributions are summarised below.

Chapter 4 - Samples grown by M. Gester and S. M. Thompson, University of York.

Chapter 5 - Samples and magnetic measurements by M. Gester and S. M. Thompson, University of York.

Chapter 6 - Substrates supplied by R. J. T. Bunyan of Defence and Research Evaluation Agency (DERA), Malvern. Spin-valves grown and magnetic measurements made on them by C. H. Marrows and F. E. Stanley, University of Leeds.

Chapter 7 - GaAs grating kindly provided by U. Pietsch and N. Darowski, University of Potsdam. Etched photoresist substrates prepared by M. G. Salt and W. L. Barnes, University of Exeter and spin-coated polymers prepared by B. J. Matterson and I. D. W. Samuel, University of Durham.

Table of Contents

Chapter 1 - Aims and Outline

This chapter aims to highlight the motivation behind the work undertaken in the thesis and demonstrate, in particular, the possible technological applications of the work undertaken. In addition, a brief review of the contents of each chapter is presented to provide an overview of the whole thesis.

1.1 Aims of Study

The overlying theme throughout this study has been to use a variety of x-ray scattering techniques to investigate the morphology of surfaces and buried interfaces from a range of thin film materials. In particular, the effect of depositing thin films on surfaces which have some form of periodic structure has been investigated, as well as an in-depth study of such surfaces themselves.

X-ray scattering is a powerful, non-destructive tool which can be used to give very accurate information on the structure of a sample, down to atomic level precision. Whilst other structural characterisation techniques, such as Reflection High Energy Electron Diffraction (RHEED), Atomic Force Microscopy (AFM), Scanning Tunnelling Microscopy (STM) and Scanning Electron Microscopy (SEM), can yield detailed information on the surfaces of materials or the composition of bulk samples, they fail to give any information on the sub-surface properties of a sample and also fail to give a detailed statistical representation of the surface. Other techniques, for example transmission electron microscopy (TEM), can be used to gain information on buried interfaces. However, whilst useful in some cases, TEM is a destructive method of analysis and is therefore limited in its applications.

The scattering of either x-rays or neutrons provides the only satisfactory way of measuring buried interface structure non-destructively. Typical diffraction (high angle) experiments can yield information on crystalline structure from the bulk of the sample,

whilst grazing incidence techniques allow the statistical nature of the surface and sub-surface interfaces to be measured. Whilst, in theory, neutrons could be used for all the types of experiments described within this thesis, the incident flux is typically low compared to that from an x-ray source. X-ray scattering, therefore, allows such non-destructive characterisation to be achieved within a short time scale and with minimal sample preparation.

The driving force behind the majority of the work presented in this thesis comes from the need to be able to characterise the structure of materials on an atomic scale. In a large number of areas the technological importance of thin film devices is increasing dramatically. The spin-valve devices investigated in chapter 6, for example, are already being integrated into certain magnetic field guidance systems and the CoAg, granular films discussed in chapters 4 and 5 could be potential data storage systems in the future. Knowledge, therefore, of how to optimise the performance of such devices is crucial. Such understanding comes initially from the ability to characterise a thin film, whereby parameters such as the thickness of constituent layers and the roughness of the surface and interfaces within the sample can be determined very accurately. To then make this information useful, it is necessary to link such data to the macroscopic properties of the sample in question. In two of the four "results" chapters, the link is between the structural and magnetic properties of the samples and how these can best be optimised for the device applications in mind. Magnetism, however, is not the only macroscopic property of such samples which can be linked to such structural characterisation. In chapter 7, the enhancement of the photoluminescence spectrum from a light emitting polymer device is linked to lateral modulations within the sample and x-ray scattering techniques are used to probe this structure.

1.2 Outline of Thesis

The majority of the work presented in this thesis concentrates on grazing incidence x-ray scattering experiments performed on thin film samples, deposited on surfaces which have some form of periodic structure or are themselves laterally modulated.

Consequently, chapter 2 introduces the theory behind the interaction of x-rays with matter in the grazing incidence regime and considers how structural information about a sample can be obtained by performing certain experiments and subsequent modelling of the experimental data.

Chapter 3 then looks at the experimental requirements for the type of experiments undertaken and considers how these requirements are met at the various experimental facilities which have been used to obtain the data.

Chapters 4 and 5 concentrate on a series of grazing incidence and diffraction measurements performed on CoAg granular thin films. Such films are becoming increasingly used for their giant magnetoresistive (GMR) properties and are excellent, potential candidates for use in the high density storage recording media of the future. Chapter 4 presents the high resolution diffraction measurements performed on these samples where an in-depth analysis of the crystalline texture of both the magnetic and non-magnetic crystal matrices is reported. The way in which the embedded Co grains grow within the Ag matrix is determined by study of the out-of-plane size of the Co crystallites and resulting changes in the strain and texture of the Ag lattice. This proposed growth method is subsequently linked to magnetic measurements taken on the samples.

Chapter 5 presents the low angle measurements performed on these samples. Initially performed as a way of characterising the thickness and roughness of the samples, detailed analysis of the data revealed an asymmetry in the diffuse scatter. The nature of this asymmetry is determined through an extensive study of the diffuse scatter. The physical cause of this asymmetry is then discussed with relation to the properties of the substrate on which the samples were grown and the growth processes used.

Chapter 6 introduces an important type of GMR device, the spin-valve. Whilst such devices are already in commercial use as magnetic field sensors, there is still a great need to develop their growth techniques and so facilitate their integration into the silicon processing industry. In this series of experiments, grazing incidence scattering measurements were performed on spin-valves grown on the industrially important silicon oxide substrates necessary for their integration into a silicon circuit. By the

nature of their growth, these substrates are seen to have a regular, tiled pattern on their surface and are considerably rougher than a normal Si wafer. The nature of the vertical conformality of the roughness within such structures is determined from analysis of the diffuse x-ray scatter and the implications this has for potential silicon integration is discussed in the context of magnetic measurements performed on the samples.

Chapter 7 studies, more directly, the effects of periodically structured surfaces and, in particular, the scattering obtained from laterally modulated structures or diffraction gratings. Whilst optical diffraction gratings have been around for many years, surfaces which are laterally modulated on a nanometre scale have only recently become available due to large improvements in growth techniques. Applications for such structures are discussed with special attention given to one particular application within the polymer film area. It has been found that depositing light emitting polymers onto laterally modulated structures enhances their photoluminescent properties. In order to understand fully this result and optimise the growth process, measurements were carried out on a variety of laterally modulated structures. To model the effect of depositing a layer on such a structure and be able to follow the propagation of roughness and lateral modulations from the substrate through to the surface, a semi-kinematical code has been written. This code develops standard scattering theory to include experimental resolution and coherence factors into the model. It aims to explain all the observed effects within the experimental data and provide a quick and easy method to model the diffuse scatter without resort to a full dynamical treatment of the problem.

Chapter 2 - Review and Discussion of X-Ray Scattering Theory

The theory concerning the majority of the x-ray scattering work presented in this thesis is, by now, very well documented. In this chapter, the basic theory concerning the interaction of x-rays with matter in the grazing incidence regime, which is directly related to experiments contained within this thesis, will be discussed. Whilst this chapter does not aim to present a complete theoretical basis for x-ray scattering it will present enough information to explain the various phenomena and effects discussed in the following chapters. References allow the reader access to more complete theoretical discussions.

2.1 Introduction

Over the last 20 years or so the use of x-rays in many areas of science has increased greatly. In line with this increase in the use of x-rays as an analytical tool, theories concerning the interaction of x-rays with matter have been developed and consolidated into firm and accepted models. It is not the intention of this chapter to reproduce all of these theories but to discuss those relevant to the experiments carried out, and results obtained, within the course of this thesis.

Discussions will concentrate on the interaction of x-rays with matter in the grazing incidence regime, as it is this type of experiment which dominates the results of later chapters. Some discussion will also be made on x-ray scattering in the high angle regime as a basis for the results of chapter 4.

2.2 Reciprocal Space And How To Probe It

2.2.1 Definition of Reciprocal Space

When an x-ray is incident upon a material, it is the interaction of this x-ray with the electrons in the material which must be considered, since the electric field components of the incident radiation will force the electrons into oscillation. These forced oscillations lead to the electrons re-radiating with a frequency equivalent to that of the incident wave but with an additional phase shift of π [1,2]. An atom represents a continuous distribution of electrons, where its atomic number is the number of electrons per unit volume, averaged over the entire volume of the atom. Hence, the atomic number gives information on the number of electrons scattering within a material. Since any material is simply a series of atoms, it can be shown that the atomic scattering factor of any particular material is, in fact, the Fourier transform of its electron density [3]. In this way, the scattering power of a particular material can be calculated.

Within a crystal structure, the atoms will be arranged in a periodic manner, so the Fourier transform of their electron density will lead to a single point in Fourier or, by definition, reciprocal space. Consequently, it is useful to consider x-ray scattering experiments in such a geometry even when, as in a non-crystalline material, the Fourier transform of the electron density does not lead to a single point.

Three primitive vectors describe the reciprocal lattice, b_1, b_2 and b_3 which are linked to the three real lattice vectors, a_1, a_2 and a_3 by the relations [4] :

$$b_1 = \frac{a_2 \times a_3}{a_1 \cdot a_2 \times a_3} \qquad b_2 = \frac{a_3 \times a_1}{a_1 \cdot a_2 \times a_3} \qquad b_3 = \frac{a_1 \times a_2}{a_1 \cdot a_2 \times a_3} \qquad -(2.1)$$

Since in real space these lattice vectors have the units of length, reciprocal lattice vectors have the units of inverse length (conveniently Å^{-1}).

In reciprocal space, the geometry of an x-ray scattering experiment can be represented as in figure 2.1.
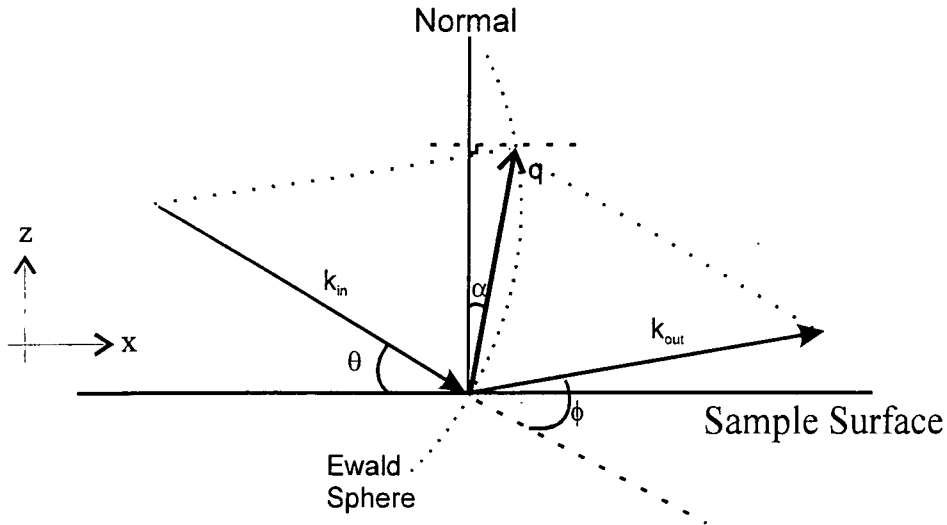
Figure 2.1 - Geometrical construction demonstrating the geometry of reciprocal space with respect to real space.

The incident wavevector, k_{in}, is defined by the angle of incidence, θ to the sample and the outgoing wavevector, k_{out}, is similarly defined by the scattering, or detector, angle ϕ.

The scattering vector, **q**, is the difference between these two wavevectors. In other words, reciprocal space can also be thought of as momentum transfer space, so, **q** $= k_{out} - k_{in}$. For the case of elastic scattering (which is being considered here) the magnitude of each of these vectors is the same and is equal to $1/\lambda$[1].

Consequently, **q** is directed normal to the surface of the sample and can be expressed in angular terms as,

$$q = \left(\frac{2}{\lambda}\right) \sin\left(\frac{\phi}{2}\right) \qquad - (2.2)$$

q can also, and indeed more usually, be expressed in terms of its in-plane (q_x) and out-of-plane (q_z) components, which from geometrical relations are,

---

[1] This is sometimes defined as $2\pi/\lambda$ depending on the convention followed

7

$$q_x = \left(\frac{2}{\lambda}\right) \sin\left(\frac{\phi}{2}\right) \sin\alpha \qquad q_z = \left(\frac{2}{\lambda}\right) \sin\left(\frac{\phi}{2}\right) \cos\alpha \qquad - (2.3)$$

$$\text{where } \alpha = \theta - \left(\frac{\phi}{2}\right)$$

A third component of $\mathbf{q}$ does exist, namely q_y, which is out of the scattering plane, if, as in this case, q_x is defined as parallel to the surface of the sample. To probe the momentum transfer in this direction it is necessary to scan in the plane of the film and this requires a multiple axis diffractometer. None of the studies presented within this thesis contain such measurements and all the data represent an integration over q_y, determined by the slit length.

2.2.2 Moving Around in Reciprocal Space

Having now defined reciprocal space in angular terms it is possible to examine how it is possible to move from one position in q to another by simply varying the angle of the sample with respect to the beam (θ) and the angle at which the detector records the scattered radiation (ϕ).

In a typical reflectivity experiment there are three types of scan which are most commonly used and all probe different areas of reciprocal space. The first scan type is the specular scan. In this case the detector angle is increased at twice the rate as that of the sample thus ensuring that $\theta = \phi/2$. By considering equation (2.3) it can be seen that the effect of scanning in such a coupled geometry is that the α term becomes zero and consequently $q_x = 0$ at all times. This means that a specular scan moves along the q_z axis, probing the momentum transfer perpendicular to the sample's surface.

Whilst it is important to measure the specular scatter in this way, there will always be a component of forward diffuse scatter present. To remove this and subsequently be able to obtain and model the *true* specular scatter it is necessary to measure the diffuse scatter just below the specular ridge. This is achieved by scanning in a coupled geometry

(in the same way as the specular) but starting with the sample angle slightly offset. In this way the sample angle becomes ($\theta + \beta$) and the detector angle 2θ, where, experimentally, β is typically -0.01°. In reciprocal space such a scan corresponds to a radial line propagating away from the q_x, q_z intercept.

In order to scan at a fixed q_z value, and consequently probe the momentum transfer in the plane of the sample, it is necessary to perform a transverse diffuse scan. In this type of scan the detector angle is fixed at a scattering angle of ϕ and the sample is then rocked from $\theta = 0$ to $\theta = \phi$. Whilst this is considered a 'fixed q_z' scan, in reality the out-of-plane component does vary slightly as a function of $\cos\alpha$. In the grazing incidence regime such a change is negligible, but it must be taken into account when performing such scans at higher scattering vectors when the scan will be decidedly curved in reciprocal space.

A fourth type of scan which is less often used in typical reflectivity experiments, is the detector only scan. In this instance the sample is fixed at some angle of incidence, θ, and the detector is then scanned out of the plane of the sample. Such a scan follows a curved trajectory through reciprocal space with both q_x and q_z varying. It is a useful scan to use when the exact position of the beam on the sample is important (as in chapter 7) since the sample need not move in the experiment.

Figure 2.2 shows a plan of reciprocal space, calculated for Si at $\lambda = 1.393$Å, with the positions of the three main scan types shown. It should be noted that there are certain areas of reciprocal space which can not be probed as these correspond to the incident or scattered x-rays penetrating below the surface of the sample. In practise, such transmission geometry measurements cannot be made for medium energy x-rays and useful information on the sample can only be obtained up to the position of the incident and exit critical angles, the positions of which are marked by the dotted arcs in the figure.
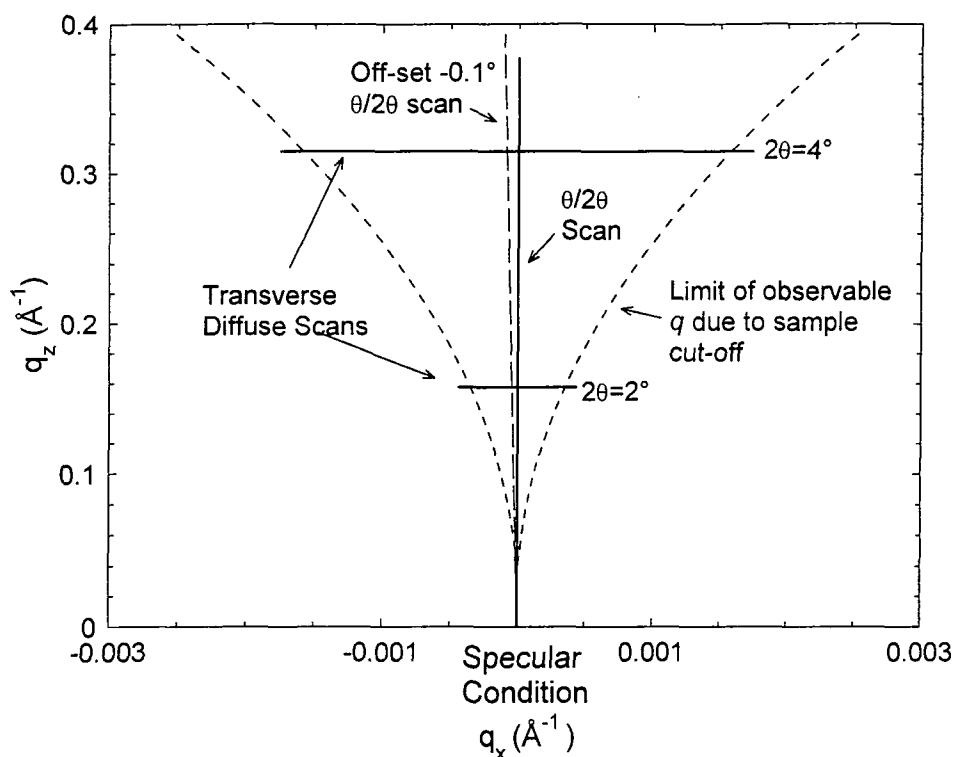
Figure 2.2 - Plot of reciprocal space showing the positions of the three major scan types. Calculated for Si at λ=1.393Å.

From this figure, and the previous discussion, it can be seen how by simple manipulation of the sample and detector positions, a full study of the scattered x-rays from a sample can be performed. In a typical reflectivity experiment it is usual to take a specular and off-specular scan along with two or three transverse diffuse scans. The off-specular can be subtracted from the specular to give the true specular scatter needed for modelling the experimental data and use of several transverse diffuse scans at different scattering vectors applies constraint to the free parameters used in modelling.

Reciprocal space does, of course, continue beyond the small projection shown in figure 2.2. When performing high angle diffraction experiments the procedures are very similar with, typically, scans being performed along the q_z axis and rocking curves ('constant' q_z) also being taken across the reflection of interest. A more detailed description of these procedures is presented in chapter 4.

2.3 Specular Scattering of X-rays from Surfaces and Interfaces

In order to obtain quantitative information from grazing incidence scattering data, it is necessary to understand the interaction of x-rays with the surface and interfaces within the sample and consequently understand how to model the recorded scatter. The theories behind these interactions are, by now, very well understood and documented, major results only being shown here. It will be shown how these theories have been used in order to develop the modelling program, which has been used in this thesis to obtain quantitative results. For a more detailed overview of the theories presented, the reader is referred to a number of recent theses and books [5-8].

2.3.1 The Region of Total External Reflection

The refractive index, n, for any given medium can be expressed as a complex number such that [9],

$$n = 1 - \delta - i\beta \qquad - (2.4)$$

where δ is related to the dispersion within the medium and β is proportional to the absorption. For the case of x-rays, δ and β are both very small, positive numbers, of the order of 10^{-5} and 10^{-7} respectively [5], resulting in a refractive index just slightly less than unity. Consequently, x-rays incident on a sample from the air (or vacuum) will observe an optically less dense medium and be refracted away from the surface normal, as shown schematically in figure 2.3.
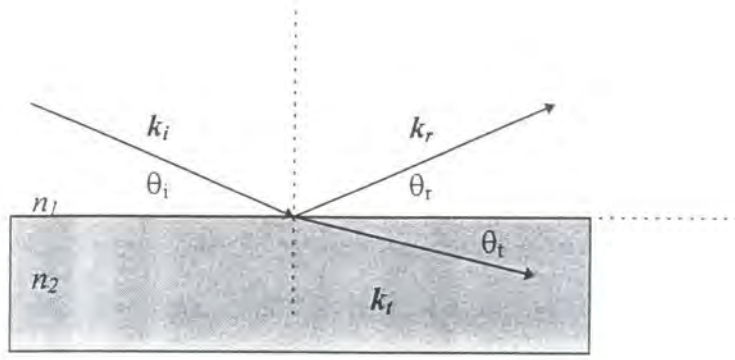
Figure 2.3 - Schematic of an x-ray incident on the surface of a sample at an angle of θ_i where the refractive index of the sample, $n_2 < n_1$. The reflected and transmitted beams make exit angles of θ_r and θ_t, with the surface, respectively.

Due to the refractive index being just less than unity for x-rays, there exists a critical angle of incidence, θ_c, below which total external reflection of the incident beam will be observed. For the situation shown in figure 2.3 it is assumed that k_i, k_r and k_t are the wavevectors for the incident, reflected and transmitted waves respectively which are considered to be plane waves of the same form.

Expressing each wave in a plane wave format [10] and requiring that, through the argument of continuity, the amplitude and gradient of the wave must match at each interface, Snell's law leads to an expression for θ_c.

It can be shown that, if absorption is ignored [9],

$$\theta_c = \sqrt{2\delta} \qquad - (2.5)$$

$$\text{where } \delta = \frac{N_A}{2\pi} r_o \lambda^2 \sum_j \frac{\rho_j}{A_j} (Z_j + f_j')$$

for a material of element j, with atomic number Z_j, atomic mass A_j and density ρ_j. N_A is Avagadros number, r_0 the classical electron radius, λ the wavelength in cm and f' is the anomalous correction to the normal atomic scattering factor, f_0.

The key point to be made about equation (2.5) is that, ignoring all the constants, for a particular element the critical angle is seen to be proportional to the square root of the electron density at any given wavelength (providing the wavelength is not close to an

absorption edge of a material in the sample and as such f' is negligible). Consequently the first piece of quantitative information which can be obtained from an x-ray scattering experiment comes from the position of the critical angle in a specular (q_z) scan. This is demonstrated in figure 2.4 where calculated reflectivity curves are shown for elements of different density at a wavelength of 1.393Å.
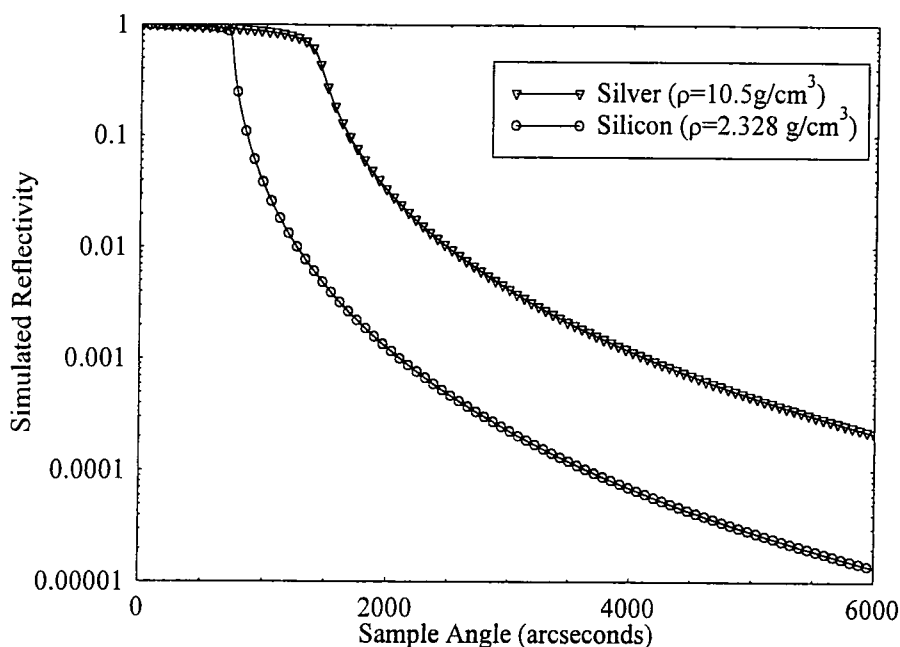
Figure 2.4 - Simulated reflectivity plots close to the critical angle for silver and silicon.

As can be seen from figure 2.4 there is a large difference in the position of the critical angle between the two simulated curves indicating how sensitive the technique of x-ray scattering is to near surface electron density.

One final point which should be made here is that for angles below the critical angle, where θ_t is complex, an evanescent wave still exists below the surface which will penetrate some distance into the sample. The distance this wave penetrates into the sample, typically ~30Å at a wavelength of 1.3Å, defines the 'near surface' regime just discussed. A sample with, for example, 5Å of Co on Si will exhibit a critical angle relating to Si. If, however the Co is 50Å thick the critical angle will be that of Co. The presence of this evanescent wave is exploited in grazing incidence fluorescence experiments [11-13] for example.

2.3.2 Beyond the Critical Angle

As the angle of the incident beam exceeds θ_c, the x-rays penetrate into the bulk of the sample, the amplitude of the transmitted radiation decreasing exponentially with depth into the material, by an amount governed by the absorption term, β. For a perfectly smooth interface, the amplitude of the reflected (and transmitted) wave is governed by Fresnel's laws and the intensity of the reflected signal is seen to fall off as $(2\theta_i)^{-4}$.

Fresnel's equations can be derived from the condition that at the interface of two media, the tangential components of the electric and magnetic field must be of equal magnitude. From these assumptions, the well known Fresnel formulae can be obtained for the reflected, F_1^R, and transmitted, F_1^T, beams. In the small angle limit they can be expressed in terms of the incident and transmitted angles such that,

$$F_l^R \approx \frac{\theta_i - \theta_t}{\theta_i + \theta_t} \qquad F_l^T \approx \frac{2\theta_i}{\theta_i + \theta_t} \qquad - (2.6)$$

These expressions are for a single surface and so do not describe the interaction of the x-rays with the multiple interfaces found in a real sample.

Parrat [14], however, used a recursive form of Fresnel's laws to describe the total reflection from a multi-planar system, as shown schematically in figure 2.5.
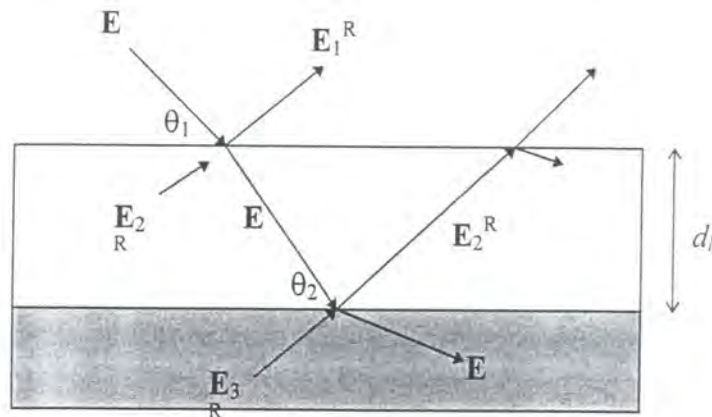
Figure 2.5 - Schematic representation of the incident, transmitted and reflected electric field within a multi-planar system.

By considering the situation shown in figure 2.5, Parrat again used the fact that the tangential components of the electric fields must match at each interface. He then began at the substrate, which he considered to be infinitely thick and from which there would be no reflected beam, and summed the reflected components of the scattered radiation back up through the stack to give a final expression for the scattered radiation. From these calculations the depth of individual layers can be obtained since the depth of each layer determines the phase factor introduced into each transmitted wavefront. The resulting scatter from such a layered system hence contains important information on the thickness of the deposited layers.

Consider a layer deposited onto a substrate. As indicated in figure 2.5, there will now be two reflected waves, one from the surface and one from the layer / substrate interface. These waves will subsequently interfere, leading to the presence of interference fringes, called Kiessig fringes [15], in the specular scatter. The period of these fringes in radians, $\Delta\theta$, is related to the thickness of the layer, d, via Bragg's law, which, in the small angle approximation, is,

$$d = \frac{\lambda}{2\Delta\theta} \qquad - (2.7)$$

Close to the critical angle, refraction effects will effect the period of the fringes so equation (2.7) is only valid for angles approximately twice the critical angle.

In addition to the period of the fringes, information can also be obtained from their intensity. The greater the difference in electron density between the layer and substrate (for example) the greater the amplitude of the fringes. This is a direct result of the atomic scattering factors used in the Fresnel reflection coefficients.

The presence of Kiessig fringes in the specular scatter is demonstrated in figure 2.6 where calculated reflectivity plots are shown for a perfectly smooth, pure layer of Co and a 500Å layer of Co deposited on Si at a wavelength of 1.393Å.
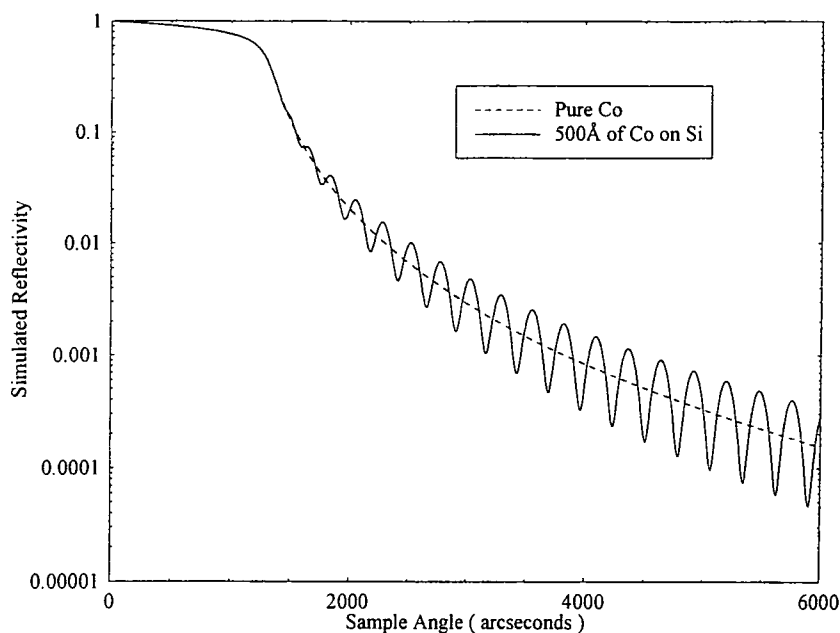
Figure 2.6 - Simulated true specular scans showing the effect of the presence of a layer in the system.

As can be seen from figure 2.6 the reflectivity from the pure Co film falls off in the expected way, with a critical angle corresponding to that expected for Co. When, a 500Å layer of Co, grown on Si is simulated, clear interference fringes appear in the specular scatter. Analysis of the period of these fringes, using equation (2.7), does indeed return a layer thickness of 500Å. In addition it should be noted that even though there is only 500Å of Co deposited on the Si, the critical angle is the same as that for the pure Co sample. This, once again, demonstrates how the critical angle is sensitive to *near* surface electron density.

2.3.3 Inclusion of Roughness

So far only the case of perfectly smooth surfaces and interfaces has been addressed. In any real system, however, some form of roughness will exist within the system. The term roughness is used here in the context of a change in the electron density profile across the interface. Such a change can either be brought about by random, atomic

16

misorientation at an interface (which leads to the 'traditional' idea of a 'rough' surface) or by a graded variation in the electron density normal to the surface of the sample, or both. Figure 2.7 shows, schematically, the difference between these two types of roughness.
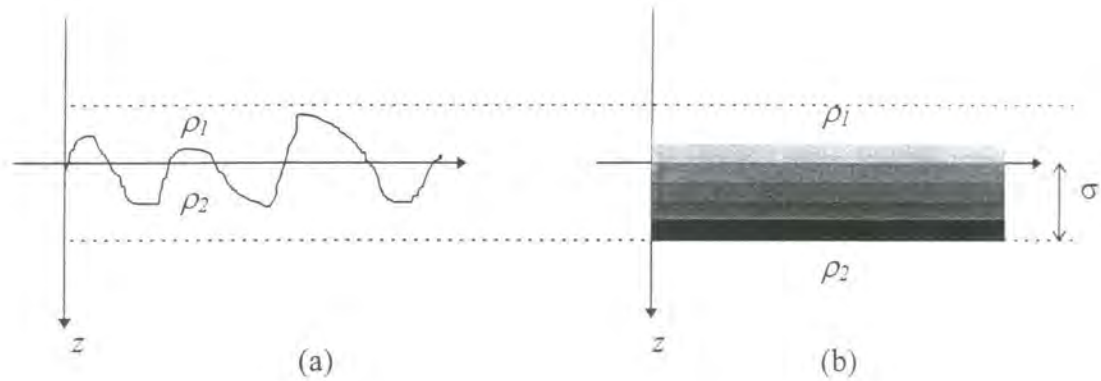
Figure 2.7 - Schematic representation between 'real' roughness, (a), and grading, (b) at an interface between two media of density ρ_1 and ρ_2. In both cases the mean interface width is the same, characterised by σ. Both cases would lead to an identical specular profile.

The first type of roughness ((a) in figure 2.7) causes the x-rays to be scattered in directions other than that of the specular reflection, with a subsequent decrease in the specular intensity. A similar effect is observed in the specular scatter for grading ((b) in figure 2.7). In this case, however, the graded profile leads to additional phase shifts in the scattered x-rays which leads to the drop in the specular intensity due to destructive interference. Therefore, from the study of the specular scatter alone, it is not possible to distinguish between an atomically rough interface and one which is graded. In order to distinguish between these two cases it is necessary to study the non-specular scatter.

A rough surface can be modelled by the application of perturbation techniques. The rough surface is replaced by a series of flat surfaces which have a distribution about an average position of the surface. The reflectivity, calculated using the Fresnel method just discussed, is then modified by a Debye-Waller factor [16] which acts as an exponential damping term. This term is defined as $-\exp(q_z\sigma)^2$ where the distribution of surface

positions is assumed to be Gaussian in nature with the mean deviation being σ. In other words, while σ can be thought of as a term which describes the roughness of an interface it does, in reality, describe the mean width of that interface which includes both 'real' roughness and grading.

Névot and Croce [17] introduced a more general form, applicable at lower q values, for the modification of the Fresnel reflection coefficients between two media, l and l-1, to account for this roughness. $F_{l-1,l}^{R}$, the Fresnel reflection coefficient between layers l-1 and l is then given by [17],

$$F_{l-1,l}^{R} = \frac{(f_{l-1} - f_l)}{(f_{l-1} + f_l)} \exp\left(-\frac{k_l k_{l-1}\sigma_l^2}{2}\right) \quad - (2.8)$$

where f_l relates to the absorption and dispersion terms in layer l and k_l is wavevector in that layer.

The effect of including this roughness term into the expression for the specular scatter can be seen in figure 2.8 where simulated reflectivity plots are shown for 500Å of Co deposited on Si calculated at a wavelength of 1.393Å. In one case all the surfaces and interfaces are assumed to be perfectly smooth and then a total roughness (or rather a mean interface width) of 5Å is specified for the Si / Co interface and 10Å for the surface.
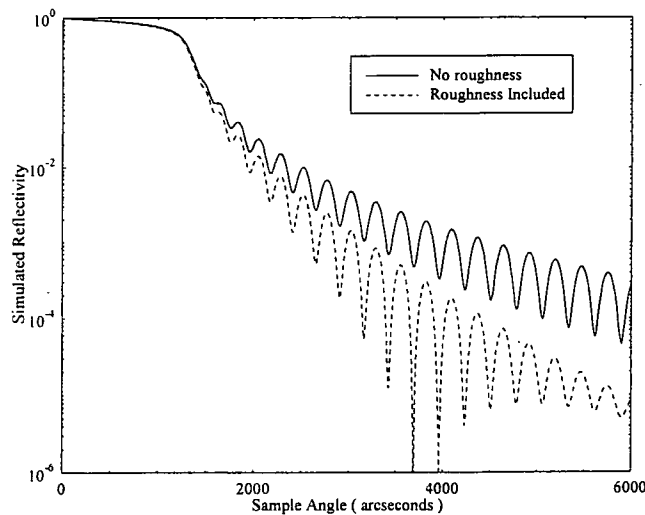
Figure 2.8 - Simulated reflectivity plots of 500Å of Co on Si, demonstrating the effect of roughness on the specular scatter.

As can be seen in figure 2.8, the effect of including roughness into the model has two clear effects. The first is that the overall rate of fall in the specular intensity is much greater when roughness is present. Additionally, the intensity of the Kiessig fringes is also modulated by the increase in roughness. It should be noted that neither the period of the interference fringes nor the position of the critical angle change upon the addition of roughness.

Whilst, in this example, specific roughness has been attributed to each interface, the exact location of roughness within a layered system can be easily obtained. There is a large difference in the shape of the specular scatter, for example, in adding roughness to the surface compared to adding roughness to the substrate (for detailed examples see, for example, [5]).

Additional effects can also be observed in the specular scatter when more layers are added. Of particular importance in many areas of x-ray scattering, is the presence of Bragg peaks, which arise from multilayered structures consisting of many bilayer repeats. In addition to the Kiessig fringes, which give information on the total stack thickness, Bragg peaks appear from the large, out-of-plane, pseudo lattice spacing of the repeated bilayers. Consequently, detailed information on the exact thickness of individual layers can be obtained. No multilayered structures are explicitly studied in this thesis so no further comments will be made on such structures.

2.4 Diffuse Scattering of X-rays from Surfaces and Interfaces

2.4.1 The Distorted Wave Born Approximation

It has been shown how the specular scatter from even a complex layered system can be easily calculated using relatively simple formalism. However, it has also been demonstrated that while the total roughness can be modelled using the Debye-Waller factor, this does not distinguish between 'true' roughness and grading. In addition it has

been shown that in order to distinguish between these two important types of electron density change, it is necessary to look at the non-specular or diffusely scattered radiation.

The modelling of the diffuse scatter is much more mathematically involved, since both in and out-of-plane roughness correlations must be taken into account, unlike, with the specular, where only momentum transfer perpendicular to the surface of the sample was being considered. In addition to this, the model for the diffuse scatter must also describe accurately the statistical nature of the interface.

Two theories used to model the diffuse scatter define the differential cross section, which describes the way in which a potential will scatter radiation in three dimensions. The first, the Born wave approximation, assumes only weak interactions, meaning the reflected wave must, by definition, be very small. This renders the Born approximation invalid for small angles of incidence when clearly such an approximation is not true. In addition, the Born approximation does not allow for multiple scattering events within the sample, so again fails to provide a complete picture of the scattering. The distorted wave Born approximation (DWBA) is a much more exact solution to the problem, which accurately predicts the form of the scattered radiation and, as such, is the most commonly used theory in modelling both the diffuse and specular scatter. The basis for this theory was first fully derived and explained by Sinha *et al* in 1988 [18] and the results presented in his paper are now commonly used for almost all modelling of grazing incidence x-ray scattering.

The Born wave approximation describes the way a potential $V(r)$ scatters radiation into three dimensions. The form of this scattering potential is assumed to be a constant within the medium and is defined as, $V = k_0^2(1-n^2)$ where n is the refractive index and k the wavevector in the layer.

In such a system, the differential cross section is expressed as a volume integral which is then converted into a surface integral using Stokes's theorem to give the differential cross section in terms of the illuminated area of the sample, L_xL_y. It is calculated to be [18],

$$\frac{d\sigma}{d\Omega} = \frac{N^2 b^2}{q_z^2} L_x L_y \iint_{S_o} dX dY \exp\left[-q_z^2 g(X,Y)/2\right] \exp\left[-i\left(q_x X + q_y Y\right)\right] \qquad - (2.9)$$

where N is the number density of scattering particles and b the coherent scattering length.

The form of the surface of the sample is described by $g(X,Y)$ which is termed the height difference function. It comes about from expressing the out-of-plane components of the surface vector as Gaussian random variables and consequently it describes the fluctuations of the sample's surface.

In fact, one of the main points to come out of Sinha's model was the way in which the surface is treated. Sinha introduced the idea of treating the surface using a fractal model. Thus, the height difference function can be defined as, $g(X,Y) = A(X,Y)^h$. The texture of the surface is then defined by the fractal exponent, h, where, as h tends to zero a highly jagged surface results and as h tends to unity the surface consists of much smoother 'hills and valleys'. However, as can be seen, this purely fractal expression is non-physical, since for large surface distances, (X,Y), the roughness tends to infinity. To avoid this, a cut-off length, beyond which the roughness saturates to $2\sigma^2$, was introduced. This length is called the correlation length and given the symbol, ξ, where,

$$g(X,Y) = 2\sigma^2 \left[1 - \exp\left[-\left(\frac{\sqrt{\left(X^2 + Y^2\right)}}{\xi}\right)^{2h}\right]\right] \qquad - (2.10)$$

In modelling x-ray scattering experiments, it is preferable to use a height-height correlation function to describe the surface as opposed to just the height difference function, since the former gives the degree of knowledge that one point on the surface has of another, a distance $R = (X,Y)$ away. This new function, $C(X,Y)$ is defined as [18],

$$C(X,Y) = \sigma^2 \exp\left[-\left(\frac{\sqrt{\left(X^2 + Y^2\right)}}{\xi}\right)^{2h}\right] \qquad - (2.11)$$

Detailed analysis has been carried out of the form of both the height difference function and the height-height correlation function as a function of surface vector R [see e.g. 5 or 6]. By definition, the lateral or in-plane correlation length, ξ, corresponds to a length scale on the surface when the correlation between two points has reduced to a value of $1/e$. In other words, it defines the area of the sample over which the surface can be considered fractal.

Other forms of the height-height correlation function have been suggested since 1988, for example, those suggested by Palasantzas *et al* in the early 1990's [19-21]. However, the form used in Sinha's paper is more mathematically convenient and is incorporated into the simulation software which has been used in the modelling carried out in this thesis.

Consequently, the differential cross section, equation (2.9), as calculated within the Born approximation can be rewritten to include this new term and becomes [18],

$$\frac{d\sigma}{d\Omega} = \frac{N^2b^2}{q_z^2} L_x L_y \exp\left[-q_z^2\sigma^2\right] \iint\limits_{S_o} dXdY \exp\left[q_z^2 C(X,Y)\right] \exp\left[-i\left(q_x X + q_y Y\right)\right]$$

$$- (2.12)$$

This term can then be split up to yield the specular and diffuse components explicitly.

However, whilst this theory provided a good base for the calculation of scattered x-rays, it fails at low angles. The DWBA circumvents the problem by using perturbation theory on the exact solution of the wave equation for a perfectly smooth surface. In this way it is assumed that the roughness of the sample acts as a perturbation on the exact Fresnel solutions, and the scattering potential (V) splits into two parts, the first (V_1) representing the ideal undisturbed system and the second (V_2) being the disturbance. In other words, $V = V_1 + V_2$.

The form of the two scattering potentials is then,

$$V_1 = \begin{cases} k_0^2(1-n^2) & -a < z < 0 \\ 0 & z > 0 \end{cases}$$

$$V_2 = \begin{cases} k_0^2(1-n^2) & 0 < z < z(x,y) & \text{if } z(x,y) > 0 \\ -k_0^2(1-n^2) & z(x,y) < z < 0 & \text{if } z(x,y) < 0 \\ 0 & \text{elsewhere} \end{cases}$$

where a is the thickness of the layer and $z(x,y)$ represents the statistical average of the surface.

The solution to the ideal wave equation $\nabla^2\phi + k_0^2\phi = V_1\phi$ can be determined exactly. An incident plane wave, ϕ_1, is scattered by the potential V_1. Since, by definition, there is an exact solution to the scattering from this ideal potential, Fresnel theory produces the exact eigenstate, ψ_1, representing a series of plane waves which have been reflected and transmitted at the interface. The waves are subsequently perturbed by the roughness, represented by V_2, and also from scattering with waves originating within the sample, represented by the time reversed eigenstate, $\tilde{\psi}_2$, leading to a final, unique solution. The transition probability from the initial to the final state, can then be shown to be [18],

$$\langle 2 \,|T|\, 1 \rangle = \langle \tilde{\psi}_2 \,|V_1|\, \phi_1 \rangle + \langle \tilde{\psi}_2 \,|V_2|\, \psi_1 \rangle \qquad \text{- (2.13)}$$

By following the detailed maths outlined in the paper of Sinha *et al* [18], an expression for the differential cross section of the diffuse scattering is reached where,

$$\left[\frac{d\sigma}{d\Omega}\right]_{Diff} = L_x L_y \frac{\left|k_0^2(1-n^2)\right|^2}{16\pi^2} \left|T(k_1)\right|^2 \left|T(k_2)\right|^2 S(q_t) \quad \text{- (2.14)}$$

where $\left|T(k_i)\right|$ are the Fresnel transmission coefficients for the incident (i=1) and scattered (i=2) waves. The inclusion of these coefficients, which the Born wave does not contain, ensures that the diffuse scatter in the region of the critical angle is

accurately modelled. $L_x L_y$ defines the illuminated area of the sample, as before, and k_0 is the incident wavevector with $S(q_t)$ defined as [18],

$$S(q_t) = \frac{\exp\left(-\frac{\left[\left(q_z^t\right)^2 + \left(q_z^{t*}\right)^2\right]\sigma^2}{2}\right)}{\left|q_z^t\right|^2} \iint\limits_{S_o} \left[\exp\left(\left|q_z^t\right|^2 C(X,Y)\right) - 1\right]\left[\exp i\left(q_x X + q_y Y\right)\right] dXdY$$

$$- (2.15)$$

where $C(X,Y)$ is the height-height correlation function already discussed.

It should be added, as a final note, that the DWBA is also used to obtain an expression for the specular scatter from a sample. The full form of the specular scatter is given in [18] but if this is expanded, assuming a Gaussian distribution of roughness, the modification to the Fresnel coefficients is the same as that obtained by Névot and Croce [17].

2.4.2 The Bede Modelling Software

Throughout this thesis, modelling software has been kindly provided, by Bede Scientific [22], to allow simulation of the x-ray reflectivity data. Several versions of this commercially available code, which has been developed by M. Wormington of Bede, have been used throughout the course of this thesis, GIXA and REFS [22] being the two main ones. While these differ in the user interface, the maths behind them is identical and follows the theory just outlined in 2.4.1, using a fractal model of the interfaces. The full mathematical treatment used in this code can be found elsewhere [23]. However, there is one key point about the code which makes it such a useful tool. Since the Fourier transform in equation (2.15) has no simple analytical solution it represents the most time consuming part of any computation, especially when calculating the large number of points needed to model experimental data. To get around this time constraint, Wormington has developed a code which is based on a series of look-up tables [23,24] enabling simulations to be undertaken in a reasonable time on basic PC's. All the

simulations presented in this chapter (and indeed in all the chapters) have been obtained using his model.

In order to obtain quantitative information on a sample using this code, the true specular scatter is modelled first. This allows information to be obtained rapidly on the thickness of the layers present in the system and also gives a measure of the overall roughness at the interfaces within the sample. The transverse diffuse data is subsequently modelled using the parameters obtained from the specular simulation. This allows the true roughness to be separated from the grading and a measure of the degree of correlated roughness to be obtained. Using such a technique, detailed quantitative information can be obtained on relatively complex samples within a short time period. An excellent example of the success of such modelling procedures comes from experimental work undertaken recently on three epitaxially grown samples from the University of Cambridge [25,26]. The samples studied were from a three-step system grown by molecular beam epitaxy, shown schematically in figure 2.9.
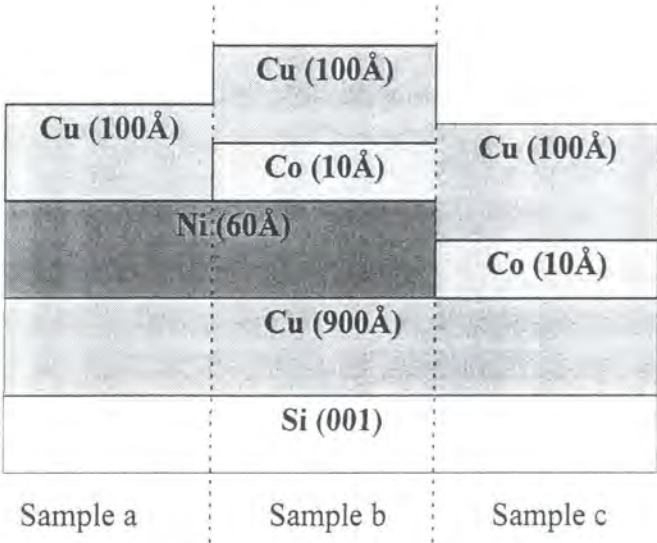
Figure 2.9 - Schematic representation of the three samples studied. All thickness values are the nominal 'as deposited' values.

The individual samples were cut from the same structure and had, therefore, all experienced identical deposition conditions. This meant that in modelling the grazing incidence scatter, identical parameters for the layer thickness and common interface

roughness values had to be used. Figure 2.10 shows the specular scatter obtained from the three samples along with the best fit simulation obtained using the Bede REFS software.
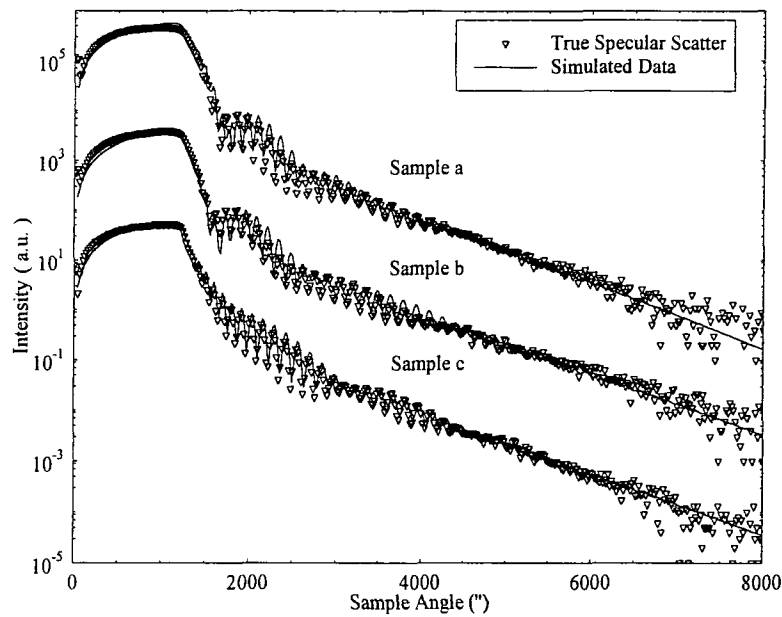
Figure 2.10 - Experimental and simulated true specular scatter from samples a, b and c

As can be seen excellent agreement between the experimental and simulated data is obtained for all three samples. Within experimental errors, the thickness of the layers, d, were identical for all three of the simulations and were in good agreement with the nominal values, as demonstrated in figure 2.11.

Layer	Nominal Thickness, d (Å)	Sample a Measured d (Å)	Sample b Measured d (Å)	Sample c Measured d (Å)
Cu	100	80 ± 2	82 ± 2	83 ± 2
Co	10	-	8 ± 1	8 ± 1
Ni	60	55 ± 2	54 ± 2	-
Cu	900	840 ± 2	840 ± 2	840 ± 2

Figure 2.11 - Table showing the nominal layer thickness and those calculated from the x-ray scattering experiments.

In addition both thickness and roughness values agreed well with those obtained from polarised neutron reflectivity and, within the experimental errors, the roughness values were identical for the common interfaces as shown in figure 2.12.

Interface	Sample	$\sigma(\text{Å})$
Si / Cu	a	6 ± 0.5
	b	6 ± 0.5
	c	6 ± 0.5
Cu / Ni	a	11 ± 2
	b	12 ± 2
Cu / Co *	c*	11 ± 2
Ni / Cu	a	16 ± 2
Ni / Co *	b*	14 ± 2
Co / Cu **	c**	10 ± 2
Co / Cu	b	10 ± 2
Cu (surface)	a	18 ± 3
	b	20 ± 3
	c	16 ± 3

Figure 2.12 - Table of roughness values obatined from the simulations.

Using the self-fitting routine 'MERCURY' which is combined with the REFS program, these simulations were obtained in only a few hours. The parameters obtained from these simulations were then used in modelling the diffuse scatter, the results of which are shown in figure 2.13.
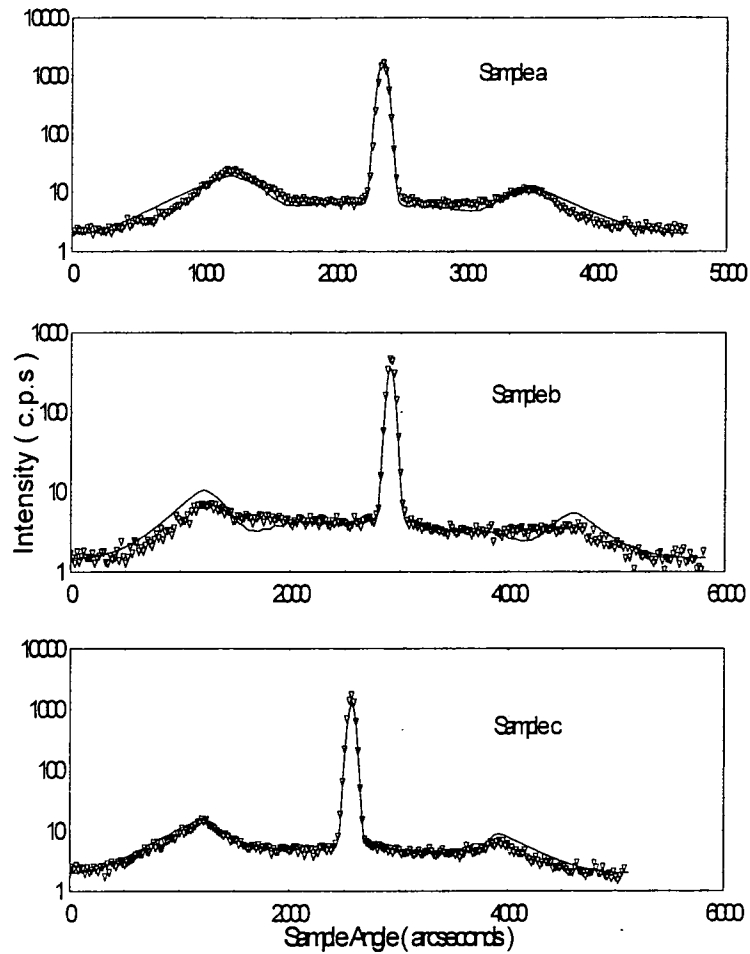
Figure 2.13 - Experimental and simulated transverse diffuse scans
from samples a, b and c.

Once again, using the parameters obtained from the specular simulations, excellent agreement is seen between the experimental and simulated data. By modelling the diffuse scatter in this way it was possible to determine that uncorrelated roughness dominated all the samples. Whilst the exact values obtained from these experiments are not of importance here, this serves as an excellent example of the power and accuracy of the simulation package used in the data analysis.

2.4.3 Examples of Diffuse Scatter from a Single Surface

By using the code described above, it is possible to look at some of the common features of the diffuse scatter from a single interface. Such features are also common to more complicated systems but, for simplicity, the diffuse scatter from just a single interface will be presented.

The most common way of probing the diffuse scatter, as discussed in 2.2.2, is the transverse diffuse scan. Such a scan probes reciprocal space at an almost constant q_z value. Figure 2.14 shows a typical transverse diffuse scan simulated for Si at a wavelength of 1.393Å.
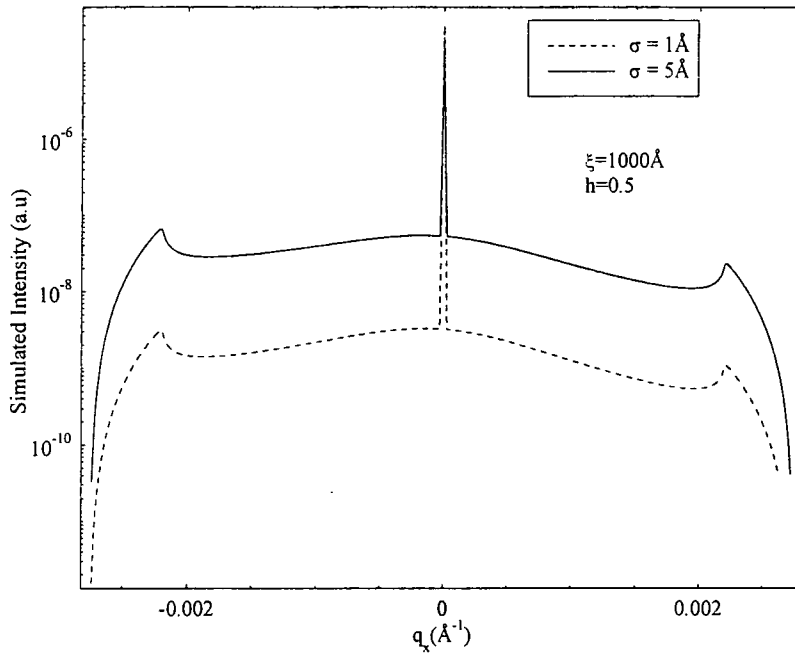
Figure 2.14 - Two simulated transverse diffuse scans for different values of total roughness.

From figure 2.14, several features common to all transverse diffuse scans can be seen. The sharp, instrument defined peak at $q_x = 0$ is the specular ridge, which can be viewed as a cross-section of the normal specular scan. Positioned symmetrically on either side of this peak are two smaller peaks at q_x values which correspond to the critical angle for Si. These peaks are known as Yoneda wings and arise due to the fact that at the critical

angle the transmitted beam lies along the surface of the sample. This means that the electric field at the surface doubles in intensity and consequently an increase in the intensity of the diffuse scatter is seen at these points. It should be noted that such a feature would not exist if the Born wave approximation was used, as it is a direct result of the inclusion of the transmission coefficients. Figure 2.14 also demonstrates the effect of increasing the total roughness on the diffuse scatter. A large increase in diffuse intensity is seen when the total surface roughness is increased from 1Å to 5Å. This indicates that a larger number of x-rays are being scattered out of the specular reflection, and their observation in the diffuse scatter is simply a consequence of the conservation of energy.

Figure 2.15 demonstrates the effect that changing ξ and h has on the diffuse scatter. In these simulated transverse diffuse scans, the specular ridge has been missed out for reasons of clarity.
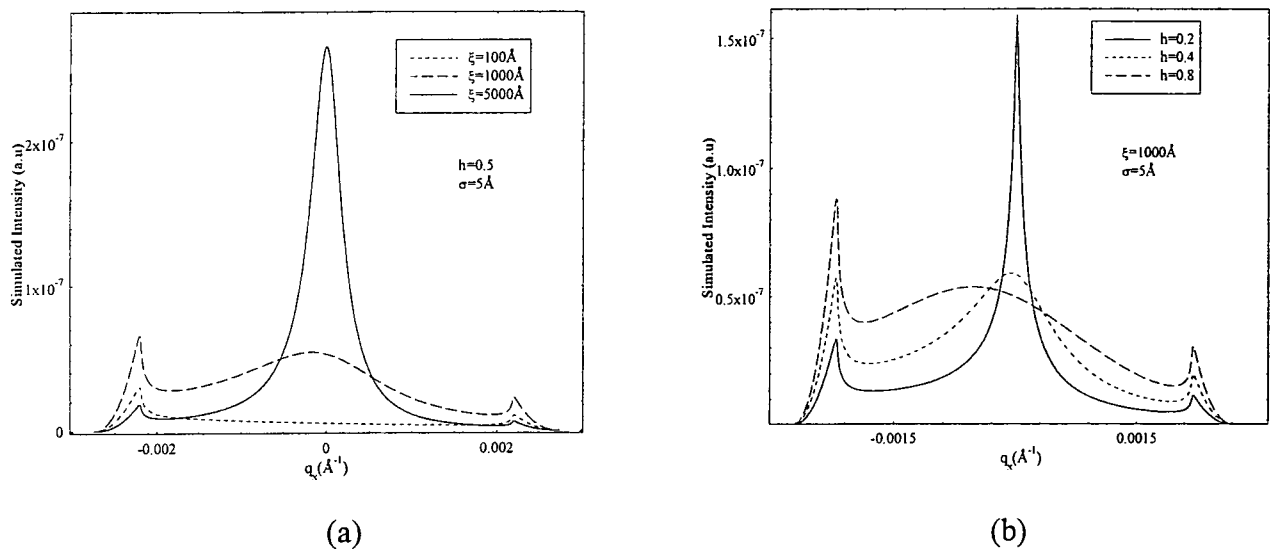
Figure 2.15 - Simulated transverse diffuse scans showing the effect of changing ξ (a) and h (b).

As can be seen in figure 2.15 (a) changing the lateral correlation length, ξ, has a marked effect on both the shape and overall intensity of the diffuse scatter. As ξ increases the diffuse intensity at low q_x increases, as it also does around $q_x = 0$, where it becomes much more sharply peaked.

This level of sensitivity to the lateral correlation length can be understood by considering the fact that the diffuse scatter is proportional to the Fourier transform of the roughness length scale. As discussed previously (2.2.1) any lateral periodicity on the surface of a sample will be transformed into a single point in reciprocal space. Consequently, the periodicities of the roughness on the surface will affect the distribution of the diffuse scatter with long frequency roughness increasing the distribution at low q_x. This explains why an increase is observed in the diffuse scatter at low q_x for larger, lateral correlation lengths.

Following on from this argument, it would be expected that for short correlation lengths an increase in the diffuse scatter would be observed at high q_x. This, however, can prove problematic to measure since the area of q which is of interest, is often inaccessible due to the cut-off introduced by the sample surface (as shown in figure 2.2). In order, therefore, to access the region of interest, it is necessary to maximise the range of q_x which is being probed - i.e. perform the transverse scan at a high scattering vector. This, however, introduces a new problem since the higher the scattering vector used, the lower the scattered intensity. This can be overcome by moving the detector out of the plane of the scattering and probing q_y. In this way, lower scattering vectors can be utilised with the associated higher flux and no cut-offs are present, allowing a much larger range of q_y to be probed. Although such a method has not been utilised in any of the studies presented here, it is an important technique in grazing incidence x-ray scattering and the reader is refereed to the original series of articles relating to this technique by Metzger and Salditt [27-30].

The effect of changing h is less marked than that of changing ξ. It is seen that as h is increased the large central peak, visible in the diffuse scatter for very low h, becomes much flatter and the overall shape of the diffuse scatter becomes far more level. Once again, Salditt *et al* have shown that it is necessary to probe a large range of q if information on the fractal nature of such a surface is to be satisfactorily obtained.

2.5 Roughness in Multilayered Systems

2.5.1 Correlated and Uncorrelated Roughness

Since introducing the idea of roughness in 2.3.3 only the effect of total roughness (or the mean interface width) has been considered. It was shown that in order to distinguish between grading and true roughness it was necessary to look at the diffuse scatter in detail and model it using the theories just discussed. However, where true roughness (i.e. not grading) exists at interfaces within a mutilayered sample, it is possible to subdivide the roughness type yet again from consideration of the out-of-plane correlations of this roughness [31-33]. The two subdivisions of roughness are correlated (conformal) and uncorrelated (non-conformal) roughness and the distinction between the two types is shown schematically in figure 2.16.

surface

substrate

(a)   (b)
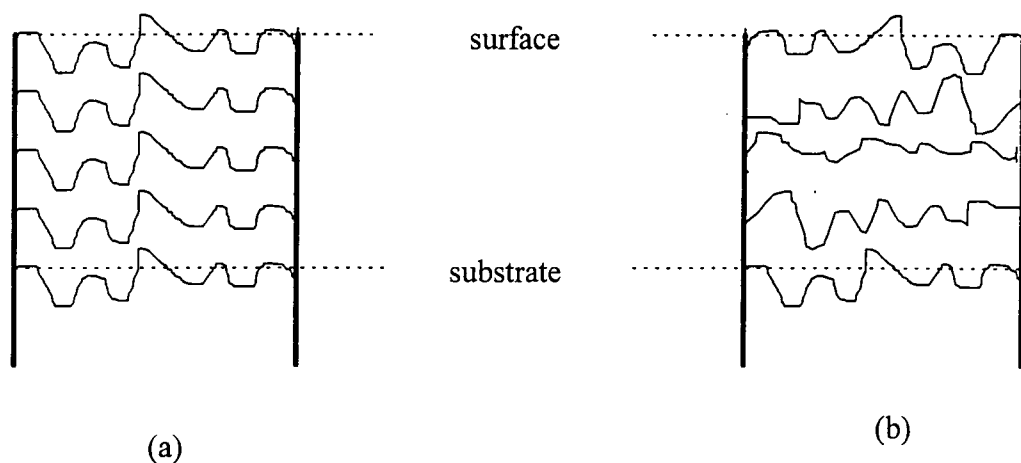
Figure 2.16 - Schematic representation of the difference between a sample with totally correlated roughness (a) and totally uncorrelated roughness (b).

As shown in figure 2.16, correlated roughness is defined as when the roughness from one interface propagates exactly to the next interface. Conversely, no replication of the interfacial roughness is seen in a totally uncorrelated sample. It should be noted that in reality it is rare to find a sample in which either type of roughness completely

dominates, the most common case being a partially correlated system with a mixture of both types.

The DWBA proposed by Sinha [18] has been extended by other groups to include the effect of depositing a number of layers on a substrate. The most notable advances in this area have been by Hóly [34-36]. In order to model these out-of-plane correlations mathematically, a covariance function is introduced [24], as was the case in modelling the in-plane correlations on the surface of the sample. The covariance function in the models used in this thesis is given as,

$$C_{j,k}(R) = \left(\sigma_{u,j} \sigma_{u,k} \delta_{j,k} + \sigma_{c,j} \sigma_{c,k} \right) \exp\left[-\left(R / \xi \right)^{2h} \right] \quad - (2.16)$$

Here, σ_c is defined as the correlated roughness between successive interfaces j and k and σ_u the uncorrelated roughness. The total roughness, σ_j, at the interface j is given by adding, in quadrature, the correlated and uncorrelated roughness, that is

$$\sigma_j^2 = \sigma_{cj}^2 + \sigma_{uj}^2 \quad - (2.17)$$

The lateral correlation length and the fractal parameter, h, remain the same for all interfaces. This model scales linearly with the number of layers, unlike other covariance functions which scale as the square of the number of interfaces, meaning computation time is kept to a minimum. This theory has been extended to incorporate the effects of compositional grading by the inclusion of an error function electron density profile at the interface [37]. It has been shown that the compositional grading and true roughness, can therefore be separated through measurement of the specular and diffuse scatter and the true roughness can further be split into its correlated and uncorrelated parts.

2.5.2 Effect of Correlated and Uncorrelated Roughness on the Diffuse Scatter

In many systems it is very important to be able to determine the extent of roughness correlations within a sample. This is especially true of magnetic multilayers where the level of roughness correlation can have a large effect on the magnetic properties of the system. A review of the diffuse scatter from such structures can be found elsewhere [5].

From the previous discussion it is clear that in order to ascertain the level of out-of-plane conformality within a multilayered sample it is necessary to study the diffuse scatter from the sample. One of the easiest ways of doing this is to study the off-specular $\theta / 2\theta$ scans. Figure 2.17 shows a specular and two off-specular scans simulated for varying degrees of vertical conformality in the roughness of a three layered sample, as described in the figure caption. All these plots have been calculated using the covariance function just discussed.
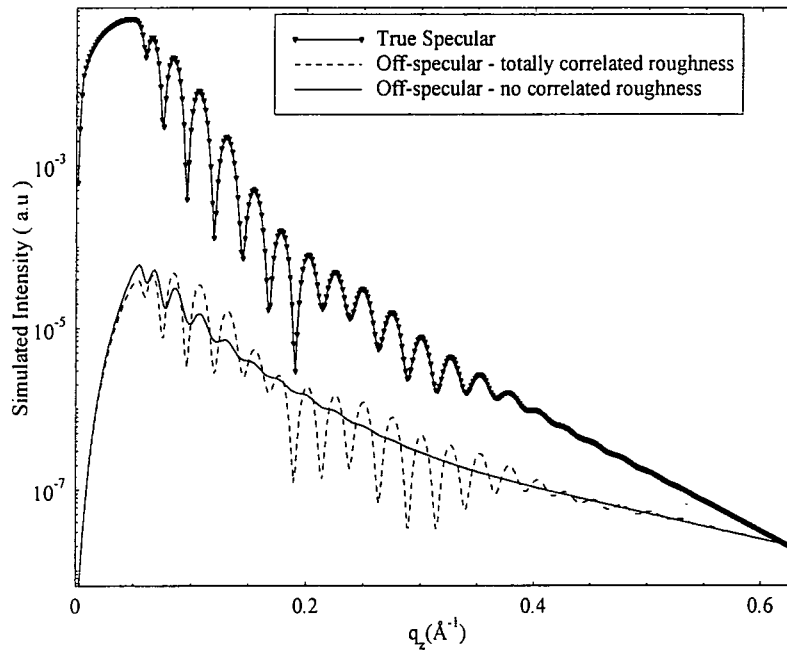
Figure 2.17 - Simulated specular and off-specular scans for a sample consisting of a 41Å layer of Ta on Si, followed by a 172Å layer of $Fe_{0.5}Mn_{0.5}$ and then a 30Å layer of Ta simulated at λ=1.393Å. The off-specular scans have been simulated with a -0.01° offset. ξ was set to 5000Å and h to 0.5.

As can be seen from figure 2.17 the specular scan contains Kiessig fringes corresponding to the total stack thickness. If the off-specular scatter is simulated with all the roughness at the interfaces uncorrelated a very smooth curve results with only a few weak oscillations at low q_z. If, however, all the roughness is specified as being totally correlated, high intensity fringes are again observed in the off-specular scatter. The period of these fringes correspond exactly to those in the specular scatter, indicating they result from the total stack thickness. In reciprocal space, the observation of these fringes in the off-specular scatter indicates that they have extended out into q_x.

The extension of this periodicity into q_x is dependent on the frequency of the roughness correlations with the lowest frequencies being propagated most easily [35,38]. Since highly correlated roughness is, by nature, low frequency, the presence of Kiessig fringes in the off-specular scatter, with the same period as those in the specular scatter, is a strong indication of highly conformal out-of-plane roughness for the entire thickness of the sample. These results are especially important when considering the work presented in chapter 6.

2.6 Theory of High Angle X-Ray Diffraction

The results contained within chapter 4 of this thesis relate to a series of high angle diffraction experiments.

High angle diffraction experiments are performed using the same geometry as the specular scan, only at much higher angles and after initially aligning the diffractometer on a known reflection from the sample. Once again, with the sample and detector being scanned out-of-the plane of the sample, such experiments are sensitive to the out-of-plane structure and hence measure the spacing of the crystal planes scattering normal to the surface of the sample. As expected from Bragg's law, diffraction peaks occur in such high angle scans at a position corresponding to these out-of-plane lattice spacings. By comparing the position of the reflections in these scans with those calculated from tabulated values it is also possible to obtain information on out-of-plane lattice strain

within the sample. Information on out-of-plane grain size and sample mosaicity can also be obtained from such scans and this is discussed in more detail in chapter 4.

The theory surrounding x-ray diffraction is, if anything, even better known and documented than that of grazing incidence scattering. It is not the intention of this section to reproduce such theory but mearly to point the reader to some excellent books on the subject [39,40].

2.7 Conclusions

This chapter has presented the basic theoretical ideas behind the x-ray scattering techniques which will be subsequently used to obtain a quantitative analysis of samples throughout the rest of this thesis. All the results and discussion contained within this chapter are discussed in great detail in two excellent review articles, to which the reader is referred to for any further information [41,42].

References for Chapter 2

[1] The Crystalline State (Vol. 2) : The Optical Principles of the Diffraction of X-Rays - R. W. James (G. Bell & Sons) (1948)

[2] B. K. Tanner - Kinematical Theory of X-Ray Diffraction (lecture notes)

[3] Theory of X-Ray Diffraction in Crystals - W. H. Zachariasen (Dover Pub.) (1994)

[4] Introduction to Solid State Physics, 6th Edition - C. Kittel (John Wiley & Sons) (1991)

[5] T. P. A. Hase - PhD Thesis, University of Durham (1998)

[6] I. Pape - PhD Thesis, University of Durham (1997)

[7] High Reolution X-Ray Diffractometry and Topography - B. K. Tanner and D. K. Bowen (Taylor and Francis) (1998)

[8] High Resolution X-Ray Scattering from Thin Films and Multilayers - V. Hóly, U. Pietsch and T. Baumbach (Springer) (1999)

[9] B. Lengeler in Photoemission and Absorption Spectroscopy in Solids and Interfaces with Synchrotron Radiation, eds. M. Campagna and R. Rosei (North Holland) (1990)

[10] Electricity and Magnetism (4th Edition) - W. J. Duffin (McGraw-Hill) (1990)

[11] M. Brunel and B. Gilles J. Phys. (Paris) Colloq. **50** *C785* (1989)

[12] D. K. G. de Boer Phys. Rev. B **44** (2) *498* (1991)

[13] T. P. A. Hase, B. K. Tanner, P. Ryan, C. H. Marrows and B. J. Hickey IEEE Trans. Mag. **34** (4 Pt. 1) *831* (1998)

[14] L. G. Parrat Phys. Rev. B **95** (2) *359* (1954)

[15] H. Kiessig Ann. Phys. (Leipzig) **10** *769* (1931)

[16] A. Braslau, M. Deutsch, P. S. Pershan, A. H. Weiss, J. Als-Nielsen and J. Bohr Phys. Rev. Lett. **54** *114* (1985)

[17] L. Névot and P. Croce Revue. Phys. Appl. **15** *761* (1980)

[18] S. K. Sinha, E. B. Sirota, S. Garoff, H. B. Stanley Phys. Rev. B **38** (4) *2297* (1988)

[19] G. Palasantzas and J. Krim Phys. Rev. B **48** (5) *2873* (1993)

[20] G. Palasantzas Phys. Rev. B **48** (19) *14472* (1993)

[21] G. Palasantzas Phys. Rev. B **49** (15) *10544* (1994)

[22] http://www.bede.com/

[23] M. Wormington PhD thesis University of Warwick (1999)

[24] I. Pape, T. P. A. Hase, B. K. Tanner and M. Wormington Physica B **253** *278* (1998)

[25] Samples kindly provided by C. A. F. Vaz, University of Cambridge

[26] Interface Dependent Magnetic Momnets in Cu/Co, Ni/Cu/Si(001) Epitaxial Structures C. A. F. Vaz *et al* - submitted to Phys. Rev. B (August 1999)

[27] T. Salditt, T. H. Metzger and J. Peisl Phys. Rev. Lett. **73** (16) *2228* (1994)

[28] T. Salditt, T. H. Metzger, J. Peisl C. H. Morawe and H. Zabel Mat. Res. Soc. Symp. Proc. **355** *269* (1995)

[29] T. Salditt, T. H. Metzger, J. Peisl and G. Goerigk J. Phys. D **28** *A236* (1995)

[30] T. Salditt, D. Lott, T. H. Metzger, J. Piesl, G. Vignaud, P. Hoghoj, O. Schärpf, P. Hinze and R. Lauer Phys. Rev. B **54** (8) *5860* (1996)

[31] Y. H. -Phang, D. E. Savage, T. F. Kuech, M. G. Legally, J. S. Park and K. L. wang Appl. Phys. Lett. **60** (24) *2986* (1992)

[32] E. E. Fullerton, J. Pearson, C. H. Sowers, S. D. Bader, X. Z. Wu and S. K. Sinha Phys. Rev. B **48** (12) *17432* (1993)

[33] A. P. Payne, B. M. Clemens Phys. Rev. B **47** (4) *2289* (1993)

[34] V. Hóly, J. Kubena, I. Ohlidal, K. Lishka and W. Plotz Phys. Rev. B **47** (23) *15896* (1993)

[35] V. Hóly, T. Baumbach Phys. Rev. B **49** (5) *10668* (1994)

[36] V. Hóly, T. Baumbach and M. Bessiere J. Phys. D **28** *A220* (1995)

[37] M. Wormington, I. Pape, T. P. A. Hase, B. K. Tanner and D. K. Bowen Phil. Mag. Lett. **74** *211* (1996)

[38] D. E. Savage, J. Kleiner, N. Schimke, Y. -H. Phang, T. Jankowski, J. Jacobs, R. Kariotis and M. G. Legally J. Appl. Phys.**69** (3) *1411* (1991)

[39] X-Ray Diffraction in Crystal, Imperfect Crystals and Amorphous Bodies - A. Guinier (Dover pub.) (1994)

[40] X-Ray Diffraction - B. E. Warren (Dover pub.) (1990)

[41] D. K. G. de Boer, A. J. G. Leenaers and W. W. van den Hoogenhof X-Ray Spectroscopy **24** *91* (1995)

[42] S. K. Sinha Acta. Physica Polonica A **89** *219* (1996)

Chapter 3 - Discussion of Experimental Requirements for X-Ray Scattering Experiments

The data presented in this thesis have been taken on a variety of dedicated x-ray scattering instruments based both in the laboratory and at synchrotron radiation sources (SRS). The basic criteria and experimental procedures on each of these instruments are very similar and a brief, general discussion will consider them together. Specific reference will be made to how these criteria are met on the main instruments used, namely the laboratory reflectometer (GXR1), station 2.3 (2.3) of the Daresbury SRS and beamline 16 (BM16) of the European Synchrotron Radiation Facility (ESRF), Grenoble.

3.1 Introduction

In this chapter a brief outline of the type of experimental apparatus used for the data collection in this thesis will be presented along with sufficient references for those wishing to read round the subject area in more detail. Two references in particular [1,2] provide excellent, in-depth discussions of all the alignment and experimental procedures for the GXR1 and 2.3. Additionally, a brief description of how both a diffractometer and sample are aligned prior to an experiment will be given.

3.2 General Experimental Requirements

In all x-ray scattering experiments certain criteria must be satisfied if a successful experiment is to be performed. A typical x-ray scattering experimental set-up is shown, schematically, in figure 3.1. The slit sizes shown are typical for reflectivity experiments and such a set-up is subsequently referred to as a 'typical reflectivity set-up'.
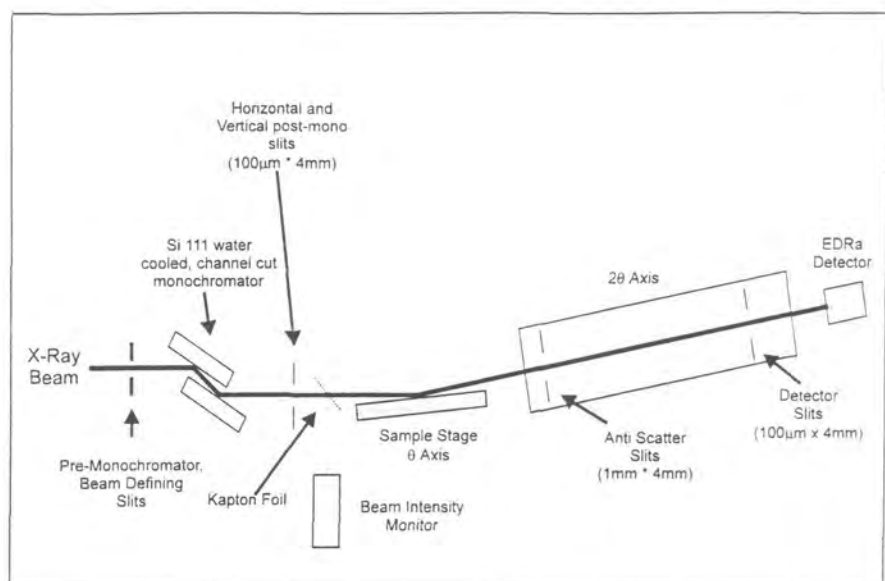
Figure 3.1 - Schematic of typical two circle x-ray scattering experiment.

All of the x-ray scattering experiments presented in this thesis rely on the basic components shown in figure 3.1 although the exact nature of each component does vary from instrument to instrument. Figure 3.2 shows a photograph of the experimental set-up of BM16, of the ESRF, showing some of the components from figure 3.1.
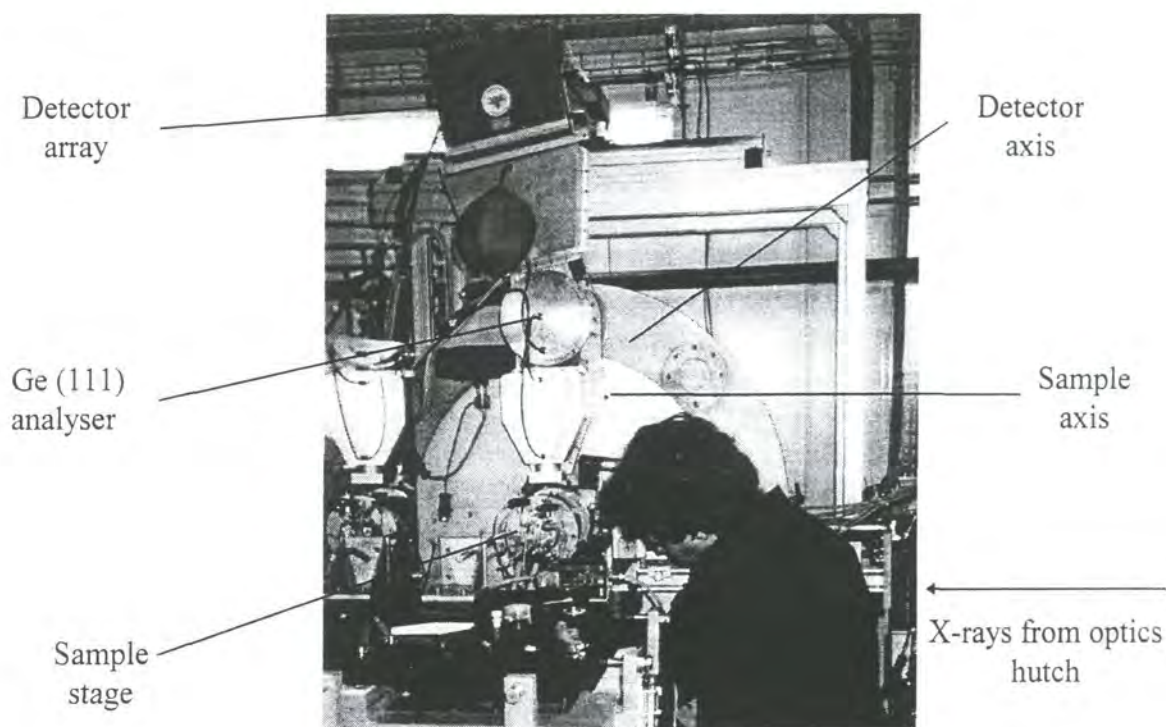
Figure 3.2 - Photograph of the experimental set-up of BM16.

3.2.1 Generation of X-rays

All x-ray scattering experiments must, by definition, have a source of x-rays. The x-ray sources used in this thesis fall into two categories.

The first type of source is the electron impact source, such as that found on the GXR1 in Durham. It consists of a sealed and evacuated tube containing a target material, typically copper. Electrons are generated via thermionic emission and accelerated through a high potential (typically several kV) before being incident onto the target. These impacts generate a wide spectrum of emitted x-rays with high intensity emission lines at energies characteristic of the target material. For the experiments performed in this thesis, a copper target was used with a wavelength of 1.393Å being selected by the monochromator, and a typical incident intensity of $\sim 10^6$ counts per second (c.p.s) at the sample. A more detailed review of the nature of electron impact devices can be found elsewhere [3,4] .

The second source of x-rays used is the storage ring. In the last twenty years there has been a widespread increase in both the number and quality of synchrotron radiation sources throughout the world with the photon flux available from such sources climbing all the time. Figure 3.3 shows an aerial shot of the ESRF in Grenoble (from [5]). The various parts of the storage ring are labelled.
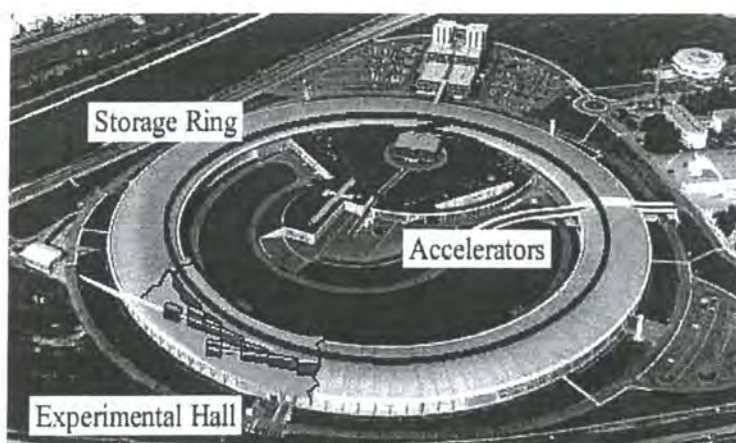
Figure 3.3 - Aerial photograph of the ESRF, Grenoble, showing the various parts of the synchrotron [5].

Synchrotron radiation is produced when charged particles undergo a relativistic acceleration process. In a typical synchrotron radiation source, charged particles are accelerated in a linear accelerator before being injected into a booster ring where they are accelerated further. When they have reached the required energy they are injected into the storage ring, which forms the major part of the source. The size of the storage ring is governed by the field strength of the bending magnets and the desired energy of the electrons within the ring. For example, at Daresbury SRS the energy of the electrons is 2GeV and the ring has a circumference of 96m [3]. In contrast the storage ring at the ESRF has a 850m circumference with the booster ring delivering electrons of 6GeV, resulting in a much shorter critical wavelength than Daresbury with more intensity at the higher end of the energy spectrum. These fast moving particles are guided round the storage ring by means of a series of steering magnets and their energy maintained by means of radio frequency cavities which are set to a harmonic frequency of revolution of the charged particles, typically a few hundred MHz. As these charged particles accelerate round the storage ring they emit x-rays which are delivered to an experimental hutch via beamlines. In addition to x-rays produced at the bending magnets in the ring, insertion devices, such as wigglers and undulators, can also be used to generate different spectra of x-rays. For example, BM16, situated 56m away from a bending magnet, allows access to energies in the range 5-40keV (λ = 2.6-0.32Å) whereas next door, ID15a is served by an asymmetric multipole wiggler and has an energy range of 40-300keV (λ = 0.32-0.04Å). A detailed discussion of insertion devices and synchrotron radiation in general can be found elsewhere [6,7].

In addition to the high photon flux generated at synchrotron sources (typical incident flux of $\sim 10^8$ c.p.s at 2.3), the collimation and frequency spectrum of the emitted x-rays make them useful to the scientific community. In the laboratory frame, the emitted x-rays from the relativistic electrons are Lorentz contracted, resulting in a cone of radiation with a small solid angle. Consequently, the majority of the generated x-rays can be collected and used, increasing the efficiency of the source. In addition to this, the wide range of wavelengths covered by the emitted radiation allows energy dependent experiments to be performed on a single beamline.

3.2.2 Beam Conditioning

For experimental purposes, a monochromatic, low divergent beam is required before the generated x-ray beam can be incident onto the sample. As discussed previously, due to the relativistic nature of the electrons, this low divergence is achieved inherently at a synchrotron. For example, 2.3, situated 15 metres tangentially away from a pair of 1.2T dipole magnets, results in an incident white beam on the water cooled, Si (111) monochromator of approximately 200'' vertical divergence [8,9]. The wavelength can then be selected by using the double bounce Si monochromating crystal. After monochromation the angular divergence of the incident beam, at this station, is typically only ~10'' [10].

At BM16 the monochromator comprises of two Si (111) crystals. The first is flat whilst the second can be bent to focus sagittally the beam. A horizontal focusing system is adopted with the source to crystal distance being equal to the sample distance. Such sagittal focusing does not effect the vertical collimation of the beam, meaning the angular divergence is also unaffected. Use of a further mirror placed directly down-stream of the monochromator allows the beam to be focused vertically increasing the incident flux. In contrast to 2.3, all the optics at the ESRF are housed in a separate hutch to the experimental apparatus resulting in a much lower experimental background noise. A schematic of the layout of the beamline is shown in figure 3.4 (from [11]).
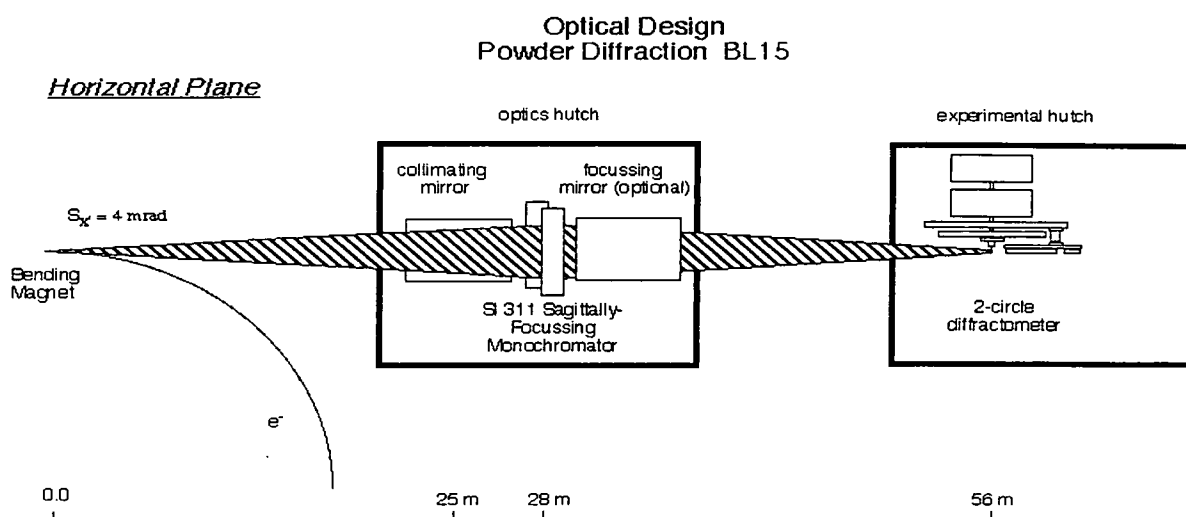
Figure 3.4 - Schematic of the layout of BM16, ESRF [11].

Additionally, it should be noted that prior to the monochromator there typically exists a series of slits which define the size and shape of the white beam.

In the laboratory the emitted x-ray spectrum has a large divergence. The x-rays from the copper tube pass through a 75μm slit before passing into an asymmetrically cut Si (111) crystal with an incident angle of 2°. This grazing incidence geometry gives a higher count rate than a symmetrically cut crystal due to its larger angular acceptance. The incident beam is finally defined as 100μm high with ~100'' divergence. A more detailed description of the GXR1 can be found elsewhere [1,2].

For all the instruments, after monochromation the conditioned beam passes to the sample through a set of beam defining slits. These can be varied in height and width to give the required beam size on the sample. At synchrotron sources the typical incident beam is defined as 4mm wide by 100μm high, as shown in figure 3.1.

Since at any synchrotron source the intensity of the incident beam will decay over time it is crucial to record its intensity to allow data taken over a long time period to be normalised. This is typically achieved using a scatter foil (for example Kapton®) placed in the incident beam with a detector recording the scattered intensity. Such monitoring is not required in the laboratory where the flux is governed by the manually controlled voltage and current settings of the tube and is consequently not a function of time.

3.2.3 Control of Sample and Detector Angles

It has already been shown, in chapter 2, that the all x-ray scattering experiments are performed by careful manipulation of the incident and detector angles. The ability, therefore, to be able to alter these quantities in very small steps and also to know accurately their position is crucial to the running of any x-ray scattering experiment.

At both synchrotron sources used, the detector and sample arms are encoded circles driven independently with accurate servo-drive motors. At 2.3 the sample arm has a resolution of 0.72'' whilst the detector's resolution is even better at 0.36'' [1]. Such a high degree of resolution is critical in order to maintain good alignment throughout an experiment and hence obtain an accurate data set. The motors on the laboratory reflectometer are stepper motors which, while being sufficiently accurate when driving the motors, are not encoded so do have the potential of losing their absolute position.

In addition to the sample and detector arms all the instruments have motors capable of translating the sample vertically and rocking the sample perpendicular to the incident beam direction (a chi rotation). These motors are not encoded and often suffer from a high degree of backlash. However, as they are typically only used during sample alignment, they do not affect the running of the experiment.

In general all the motor driving and data collection is controlled though a piece of instrument-specific computer software. Such software allows for much simpler data collection and often allows for several scans to run automatically in succession.

3.2.4 Detection of Scattered X-Rays

From considering the typical types of experiment discussed in chapter 2, it is clear that the choice of detector used in such experiments is crucial. In a typical reflectivity experiment, for example, the detector must be able to cope with detecting, in one case, a totally reflected beam and then be accurate enough to handle the low intensity of the diffuse scatter. The difference in intensity between these extremes can be as much as 8 orders of magnitude.

The detector used in all these experiments was the Bede EDRa [12]. This high dynamic range detector has a minimum count rate of ~0.15 counts per second and was found to be non-linear for count rates greater than 4×10^5 counts per second. In addition the dead time of the detector was calculated to be 350ns. Although offering one of the better performances of available x-ray detectors, it was still often necessary to attenuate the

incident beam. This was achieved using a series of aluminium foils placed before the sample and resulted in having to scale the data to account for this attenuation. Such scaling was performed without any noticeable differences in the data.

In order to define the resolution of the experiment, that is to say the acceptance of the detector, a series of slits are placed in front of it, as shown in figure 3.1. Resolution slits are situated immediately in front of the detector and are set to the 100μm high and 10mm wide, the height of the slits being the same as the defined incident beam. In addition, anti-scatter slits are placed on the detector arm near to the sample. These are typically set to 1mm in height and 10mm wide and serve to reduce the noise at the detector by eliminating extraneous scatter. Such a set-up gives, at 2.3 for example, an angular detector acceptance of ~620''. In order to reduce further the absorption, the air path from the sample to the detector is typically evacuated.

At BM16 there is the option of using a set of analyser crystals in preference to the slit geometry just described. The analyser system comprises of 9 germanium (111) crystals, separated by 2°, the scatter collected by each crystal being recorded by an independent detector. These crystals, therefore, then define the acceptance of the detector. This analyser set-up was used to obtain the high angle diffraction data discussed in chapter 4. In order to use a slit configuration instead of the analyser, all the analyser crystals can be set to a 'straight through' position and only one of the nine detectors be used to record the scatter.

3.3 Running an Experiment

3.3.1 Alignment of a Sample

The most important factor in the alignment of a diffractometer at the start of an experiment is to ensure that the sample is in the centre of rotation of the diffractometer. This is achieved through a manual, optical alignment procedure. The sample arm is rotated though 180° and the position of the surface of the sample holder is monitored to

ensure it does not more either laterally or vertically. If it is seen to move in either of these directions small, iterative changes are made to the sample holder goniometer until no movement is observed upon rotation. This typically ensures the alignment is accurate to 25μm. Once in the centre of rotation the whole diffractometer is shifted vertically to ensure that the sample table itself half cuts the incident beam meaning the centre of rotation of the diffractometer is now exactly in the centre of the incident beam.

With a well aligned diffractometer, aligning a sample is relatively straight forward. With no sample initially in place the detector is scanned through the full incident beam and set to zero at the point of maximum intensity. The sample is then moved into the beam until it is half cutting it. To ensure the surface of the sample is flat with respect to the x-ray beam the sample is rocked and set to zero at the point of maximum intensity. The detector is then moved to a small angle (typically 2°) and the sample rocked, in very fine steps, around half of this value until a maximum in the intensity is found. This position of maximum intensity is then set to half the detector angle. By performing this process, iteratively, at increasingly higher detector angles, the detector and sample arms are consequently coupled to the position of the specular reflection and the sample is considered aligned.

Whilst monochromators at all synchrotron sources are typically highly encoded, a check is always performed on the calibration of the wavelength prior to the start of an experimental run. This is achieved by recording the near edge x-ray fluorescence from a standard Cu sample in the vicinity of the Cu absorption edge. The standard sample reproduces a clear peak in the spectrum just beyond the Cu edge for all experiments and this peak provided an excellent reference point for all experiments [13].

3.4 Conclusions

The basic requirements for x-ray scattering experiments have been discussed. How these requirements are met on the various instruments used for data collection in this thesis has also been discussed. It should be added that some of the data presented in this thesis were taken on station 16.3 of the Daresbury SRS. Whilst the diffractometer on this

beamline has multiple axes and can be used in a variety of configurations it was only ever used in the typical reflectivity set-up which has been described in this chapter and, as such, is not discussed specifically.

References for Chapter 3

[1] I. Pape - PhD thesis, University of Durham (1997)

[2] J. M. Hudson - PhD thesis, University of Durham (1994)

[3] X-Ray Science and Technology - ed. A. G. Michette and C. J. Buckley (IOP) (1993)

[4] W. -J. Lin PhD thesis - University of Edinburgh

[5] http://www.esrf.fr/info/ESRF/about/machine/

[6] G. Margaritondo J. Synchrotron Rad. **2** *148* (1995)

[7] Neutron and Synchrotron Radiation for Condensed Matter Studies Vol. 1 - ed. J. Baruchel, J. -L. Hondeau, M. S. Lehmann, J. R. Ragnard and C. Schlenker (Springer-Verlag) (1993)

[8] C. C. Tang, S. P. Collins, B. M. Murphy, N. D. Telling, R. A. Wogelius and S. J. Teat - Review of Scientific Instruments Vol. 69 no. 3

[9] C. C. Tang, M. Miller, D. Laundy *Station 2.3 Manual*, CCLRC Daresbury Laboratory

[10] R. J. Cernik, P. K. Murray, P. Pattison, A. N. Fitch J. Appl. Cryst. **23** *292* (1990)

[11] http://www.esrf.fr/exp_facilities/BM16/handbook/handbook.html

[12] S. Cockerton and B. K. Tanner Adv. in X-Ray Anal. **38** *371* (1995)

[13] B. K. Tanner, D. E. Joyce, T. P. A. Hase, I. Pape, P. J. Grundy Adv. X-Ray Anaylsis **41** *CD-Rom Edition* (1997)

Chapter 4 - High Resolution X-Ray Diffraction Studies of CoAg Granular Films

High resolution x-ray diffraction (HRXD) studies have been carried out on a series of cobalt / silver (Co / Ag) granular systems where the concentration of Co in the systems has been varied from 0 to 32 atomic percent (at. %). Results from these HRXD studies have been analysed with a view to determining the evolution of the shape and size of the Co grains within the Ag matrix as a function of increasing Co concentration. The proposed growth is discussed in relation to the magnetic properties of the samples as is the role that the size and shape of such grains play in determining the giant magnetoresistive properties of these systems.

4. 1 Introduction

4.1.1 Magnetoresistance and Giant Magnetoresistance

Magnetoresistance (MR) is the change in electrical resistivity of a sample due to an external magnetic field. Although in the free electron model of metals there is no MR, the effect exists in all real metals, its magnitude and behaviour varying between materials. In ordinary, non-magnetic metals, such as Au, the effect is quite small and is known as 'ordinary MR'. The magnitude of the effect is proportional to the square of the applied field and does not reach a saturation point. In ferromagnetic metals, such as Fe and Co, substantial MR can be observed. This 'anisotropic MR' is a result of the motion of ferromagnetic domains within the sample under the application of a magnetic field and, as such, is seen to saturate. Typical values of this AMR are 1% at 5K in Fe or Co although in alloys, such as permalloy, AMR values up to 15% can be achieved. Such AMR alloys have formed the basis for most low field magnetoresistive applications,

such as magnetic tapes. The term giant magnetoresistance (GMR) was introduced when much larger changes in resistance, over a factor of 2, were observed.

GMR was first observed experimentally in transition metal multilayers in the late 1980's [1,2] where magnetic layers were initially coupled, antiferromagnetically, across a non-magnetic spacer layer. It was observed that changes in resistance of up to 65%, at room temperature [3], could be achieved on the application of a magnetic field to such structures. Widespread research into this phenomena soon showed that this effect was not confined to multilayered systems. Careful spin engineering allowed 'sandwiches' of magnetic layers to be formed where the layers were forced to align antiparallel in zero field. These 'spin-valve' structures were also shown to exhibit GMR [4]. Although such spin-valves had much lower GMR values, typically 4-6%, [5] the switching fields needed were much smaller, making them potentially far more useful in magnetic sensors. A full review of such structures and their applications is given in chapter 6. Such experiments demonstrated that GMR was simply a feature of electron transport between non-aligned ferromagnetic regions in a sample and did not rely on a multilayer structure.

The work on, and mechanism behind the GMR phenomenon in both multilayers and spin-valves will not be discussed here but the reader is referred to chapter 6 where a more complete discussion of spin dependent scattering is presented. In this chapter, the effect of GMR in granular systems will be concentrated on.

4.1.2 GMR in Granular Systems

Following the work with spin-valves, which indicated that GMR was solely a consequence of misaligned ferromagnetic regions within a system, several groups began to turn their attention to granular, alloyed systems [6,7]. Granular, magnetic solids consist of single-domain, ferromagnetic particles, typically Co or Fe, embedded in an immiscible medium. Isolated, magnetic particles occur in such materials where the metal volume fraction of the magnetic material, x_v, is less than the percolation volume, typically ~55% [8]. Below this percolation volume it is found that the grains are

typically single domain, well separated and magnetically hard. Above the percolation volume the grains tend to form an infinite network of interlinked grains and, as such, demonstrate softer magnetic properties.

Such particles were initially embedded in an insulating matrix, such as SiO_2 or Al_2O_3, making them no use for the study of magnetoresistance. Childress and Chien [9,10] then began to study the properties of granular systems where the matrix was metallic, typically Cu or Ag, which allowed magnetoresistive properties to be studied. This work led to the first reported GMR in such a system. Although most of the original work involved Co / Cu systems [6,7] the remainder of this discussion will concentrate on the CoAg system, with which this investigation is concerned. The majority of the comments, however, are applicable to all granular systems.

At equilibrium, Co is totally immiscible in Ag [11]. However, using vapour quenching deposition techniques, where Ag and Co are co-deposited onto cooled substrates, a metastable alloy of CoAg can be formed [12]. The use of ambient substrate temperatures, or the annealing of the metastable alloy, leads to the production of Co-rich clusters within the Ag matrix and, eventually, phase segregation, such that single domain regions of Co are present within the now granular film. It has been shown that such ultrafine magnetically ordered particles must exist as single domains below a critical size, ~100's Å for Co [13,14]. Consequently, the resulting structure can be imagined as consisting of grains of Co randomly distributed throughout the Ag matrix. Using this as a model of an ideal granular system, the mechanism behind the GMR effect in such a structure can now be discussed.

As has been suggested previously, GMR originates from the presence of non-aligned ferromagnetic regions within a material. In the case of a granular film, grown in zero field, there is no preferred orientation for the moments of the magnetic grains within the system. This means that the moments in the magnetic grains will adopt a random orientation within the sample leading to no overall magnetic moment.

Electrical resistance is, effectively, a measure of the degree of electron scattering within a material. The more times an electron is scattered as it passes through a material the greater will be the resistance. Consequently, to develop the idea of GMR within a

granular film it is necessary to consider what happens to an electron travelling through such a system before and after applying an external magnetic field.

It is well documented in much of the original work on multilayered systems [1-5], that the mechanism of GMR relies on the spin-dependent scattering of electrons at the ferromagnetic / non-ferromagnetic interfaces. Electrons travelling through a magnetic material can be classed as either having their spins aligned parallel or anti-parallel to the magnetic moment within the magnetic material. Electrons whose spins are aligned parallel to the direction of the magnetisation within the ferromagnetic material are scattered less strongly than those which are aligned antiparallel. It is the difference in the degree of scattering between these different spin states which is the key to GMR.

In the case of the 'as deposited' sample, with its randomly orientated magnetic entities, the situation is as illustrated in figure 4.1.
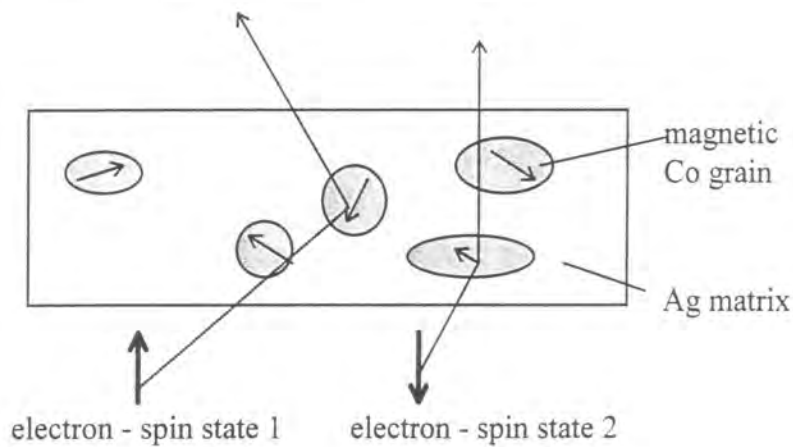
Figure 4.1 - Randomly orientated, 'as deposited', granular film

The magnetic, single domain Co grains are randomly oriented within the Ag matrix. This results in both spin orientations of the electron being scattered equally as they pass through the sample leading to a high resistive state. If an external magnetic field is now applied to the sample the magnetic moments in the Co grains will rotate to align with the applied field resulting in the situation show in figure 4.2.
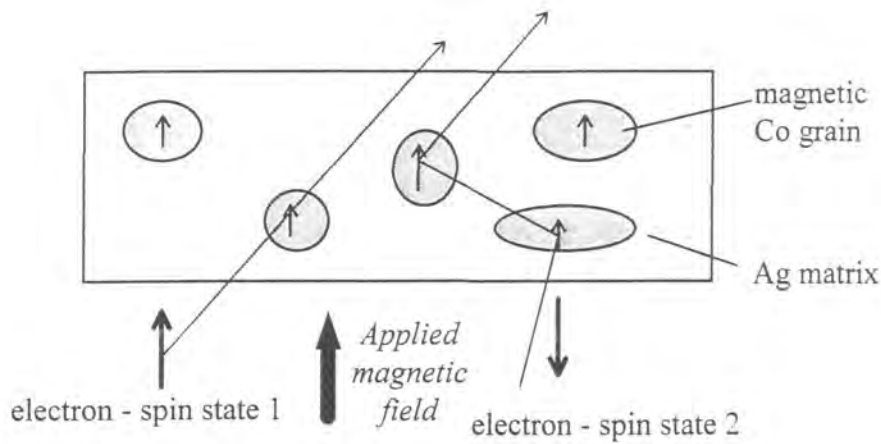
Figure 4.2 - Orientation of the Co grains within the Ag matrix on the application of an external magnetic field

With the magnetic domains now aligned in one direction a low resistance path is created for one of the electron spin states - in this case the spin state 1. Although the other spin state will be strongly scattered, the resulting overall resistance will be much lower than previously due to this low resistance shunt. On the removal of the applied field the magnetic moments will once again become randomly aligned, along the easy axes of the sample, leaving a high resistive state. It should be noted that the maximum misalignment between moments is realised before any field is applied. Once a field has been applied some alignment will remain, meaning the high resistive state the sample returns to will not be as high as its original. In other words, the GMR is history dependent.

The rotation of the magnetic moments within the Co grains upon the application of an external field is hindered by the local anisotropies of the grains themselves. As the sample resistance is a measure of the degree of alignment of the moment with the field, it is to be expected that the change from the high to low resistive state will show a field dependence and a degree of hysteresis. The strength of the field required to change between the resistive state is thus related to the local crystal anisotropy as well as a degree of coupling between the grains. This is demonstrated in figure 4.3 where the resistance of a typical granular film is shown as a function of applied magnetic field.
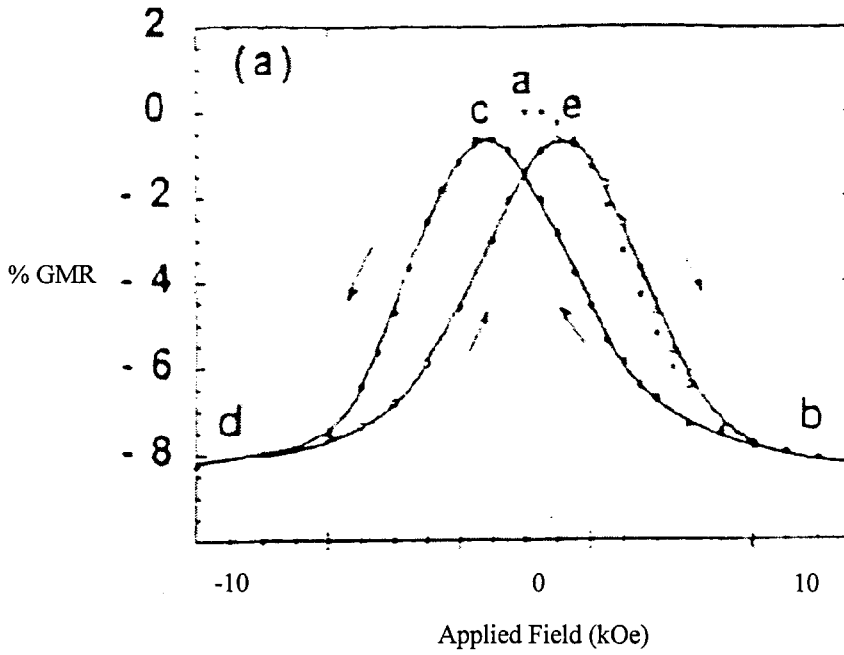
Figure 4.3 - Demonstration of the change in the resistance of a granular sample upon the application of a magnetic field. Reproduced from [15].

The magnitude of the GMR is typically defined as a percentage such that,

$$\%GMR = 100 * (R_0 - R_{sat}) / R_{sat}$$

where R_0 is the resistance of the sample in zero applied field and R_{sat} is the resistance in a saturating field.

In such a system, the magnitude of the GMR is heavily dependent on certain physical factors, one of the key ones being the size and separation of the magnetic inclusions. It is crucial that the ferromagnetic clusters occur on a lengthscale comparable to the mean free path of the electron and that the clusters themselves are of a similar size. A few, small Co particles result in a few, far apart scattering events in the time taken for the electron to travel along its mean free path, leading to a small GMR. As the particles grow and consequently become closer together the GMR will increase as the scattering due to the Co increases. Beyond a certain point, however, the size of the Co regions will become large compared to the mean free path of the electron and the GMR will degrade [16]. A similar view point [17] highlights the importance of the spin-diffusion length, maintaining that the spin information on the electron must be conserved between the

ferromagnetic regions. This means that the grains have to be closer together than the spin-diffusion length of the electron. As well as just considering the separation of the grains however, it must be noted that the spin diffusion length can change. As the grains grow there will be fewer impurities within the Ag lattice so the spin diffusion length will increase. However, in this case, as the separation of the grains decreases there will be more ferromagnetic interaction between the grains and the GMR will therefore decrease.

As well as these effects there is one other crucial point to consider, namely whether interfacial or bulk scattering dominates in such a system. As the particles get bigger the surface / volume ratio decreases, reducing the spin-dependent interfacial scattering relative to the bulk scattering process [18], acting in the opposite way to the previous mechanism. Dieny maintains [19] that in granular systems interfacial scattering dominates but the whole issue of interfacial versus bulk scattering is still an area of great debate. Despite the lack of agreement in this area, it is clear that if the GMR of such a sample is to be maximised, key physical parameters of the system must be optimised, namely the size, shape and separation of the embedded clusters. Consequently, the ability to determine how such clusters grow, as well as determining the crystalline texture of the materials within the system, is crucial in the understanding and predicating of the magnetic properties of granular films.

4.2 Experimental Procedures

4.2.1 Sample Fabrication and In-Situ Characterisation

Three samples were grown for this study by molecular beam epitaxy (MBE) at the University of York. Two CoAg granular films and one pure Ag reference film were deposited onto 7x7 reconstructed Si(111) wafers in the ultra high vacuum (UHV) system at York. Approximately $1x1cm^2$ Si(111) substrates were cut from a commercially available wafer and were heated by electron bombardment under UHV.

The heating power was increased gradually over 20 minutes until the 7x7 reconstruction temperature could be observed by in-situ RHEED measurements. The metal films were then deposited onto the substrates which were held at a temperature of 150°C which was above that at which the 7x7 reconstruction had been observed. The Co was evaporated from an electron beam source at the bottom of the MBE chamber providing a beam of Co normal to the substrate surface. The Ag was evaporated from a Knudsen source at an angle of 47° with respect to the surface normal. Further information on the growth and in-situ characterisation techniques used at York University can be found elsewhere [20,21].

The concentration of Co in each of the CoAg granular samples was determined from energy dispersive x-ray (EDAX) measurements to be 18 at. % and 32 at. %. The flux from the metal sources were measured using a quartz crystal monitor with a precision of 10%. The nominal thickness of the deposited samples were obtained from these flux measurements to be :-

$$Ag \text{ reference film - } 420\text{Å}$$
$$Co_{18}Ag_{82} \text{ film - } 453\text{Å}$$
$$Co_{32}Ag_{68} \text{ film - } 370\text{Å}$$

These thickness include a 20Å thick Ag layer which was deposited onto each granular film to prevent oxidation of the Co grains within the film.

4.2.2 Description of X-Ray Measurements

A series of experiments were conducted on these samples at stations 2.3 and 16.3 of the Daresbury SRS and also at BM16 of the ESRF, Grenoble.

Wavelengths of 1.381Å and 0.8Å were selected at stations 2.3 and 16.3 respectively in order to obtain maximum incident flux. A wavelength of 1.381Å was selected at BM16 in order to allow direct comparison between these data and those taken at station 2.3 of the Daresbury SRS.

In order to obtain data of sufficiently high quality it was necessary to maximise the resolution of the instrument being used. By defining a very narrow beam before the sample and having narrow slits directly in front of the detector a very high resolution can be obtained. However, the diffracted intensity obtained using such a configuration can be quite low, so the resolution is lowered by opening up the two sets of slits, increasing the diffracted signal. An optimal condition combining these two effects has to be reached. Figure 4.4 shows the effect of using 100µm and 300µm, beam defining and detector slits.
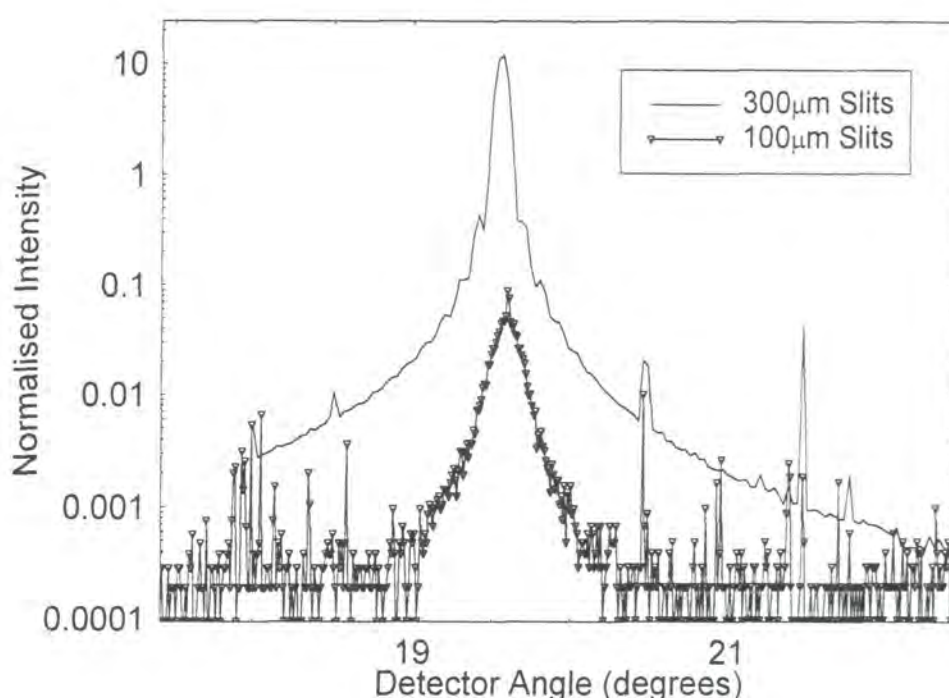
Figure 4.4 - Coupled $\theta/2\theta$ scans over the Ag(111) peak for different slit geometries

As can be seen in figure 4.4 when the 100 µm slits are used the tails of the peak are quickly lost in the inherent, experimental noise. By increasing the slits to 300µm the resolution of the peak remains the same but its overall shape improves as it is now possible to observe the full tails above the level of the noise. This makes the measured peaks far easier to fit.

Whilst a slit configuration was used at both Daresbury SRS stations a Ge(111) analyser was used at the ESRF (see chapter 3) where it was found that the optimal resolution

and signal to noise ratio could be obtained by using this as opposed to a slit configuration.

The majority of the results presented are from BM16 since this is where the best quality data, needed for peak analysis, were obtained. Only the full reciprocal space maps, presented at the end of this section, were taken at the Daresbury SRS.

At each beamline, the form of the experiments undertaken were identical. An initially coarse, coupled $\theta / 2\theta$ scan was performed around the known position for the Si(111) reflection. Once this reflection had been identified and the θ and 2θ axes calibrated, a more accurate coupled scan was performed over both the Si(111) reflection and the expected position of the Ag(111) reflection. The experimental configuration was optimised so that a maximum reflected intensity was recorded at the peak of the Ag reflection. This was achieved by repeatedly scanning the 2θ and θ axes independently and maximising the counts recorded, calibrating the θ axes to be equal to half of the 2θ value at the point of maximum intensity. Figure 4.5 shows the effect of performing such an optimisation.
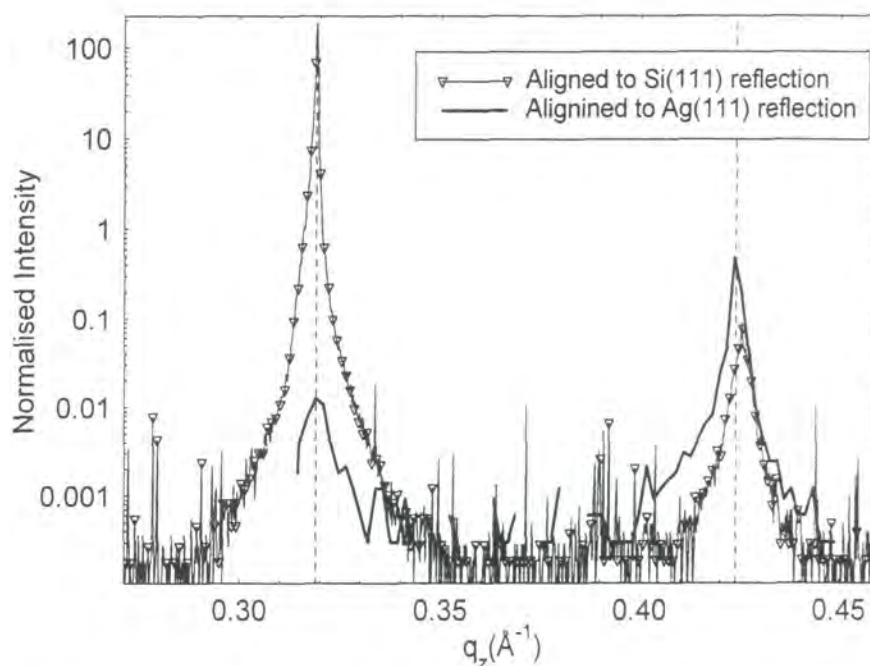

Figure 4.5 - q_z scans shown over the same range when aligned to the Si(111) reflection (at $q_z \sim 0.32 \text{Å}^{-1}$) and Ag(111) reflection (at $q_z \sim 0.42 \text{Å}^{-1}$) . Dotted lines show the positions of these reflections calculated from tabulated values.

Figure 4.5 shows that the effect of such an optimisation is to increase the intensity recorded at the Ag(111) reflection. The intensity of the much sharper Si(111) reflection is lost in such an alignment, due to the misalignment of the Ag and Si (111) planes, but since the Si reflection is only used as an initial reference point in these experiments, this is not a problem.

High resolution q_z scans were performed over both the Ag and Co reflections, ensuring the statistics obtained were sufficiently good to allow the peaks to be fitted. Transverse scans along q_x were recorded across each peak with the detector fixed at the 2θ angle of the required reflection and the sample rocked about its mean position in θ. By performing such rocking curve scans and incrementing the position of the detector, so that all scattering vectors over the reflection are covered, full reciprocal space maps (FRSM) of the Ag(111) reflection were also recorded with the scatter being simultaneously viewed in both q_x and q_z .

4.3 Presentation of Experimental Results

In the presentation of these results the experimental data has generally been normalised to the thickness of the three samples to give information independent of the amount of material present. Several methods were used to determine these thickness. Grazing incidence x-ray scattering measurements were performed on all three samples and the results of these experiments are presented in chapter 5. Due to the nature of the roughness in these samples is was only possible to determine the thickness of the pure Ag and $Co_{18}Ag_{32}$ granular film as no Keissig fringes were present in the other granular sample. Similarly, tallystep measurements performed on the samples did not lead to a full thickness dataset. Consequently, the thickness used are the ones obtained from the flux monitor which have been discussed previously in section 4.2.1 Since the thickness obtained from the flux monitor agree very well with the two grazing incidence x-ray results they can be taken to be a good representation of the true thickness.

Figure 4.6 shows q_z scans for all three samples taken over both the Ag and Co reflections, normalised with respect to the film thickness.
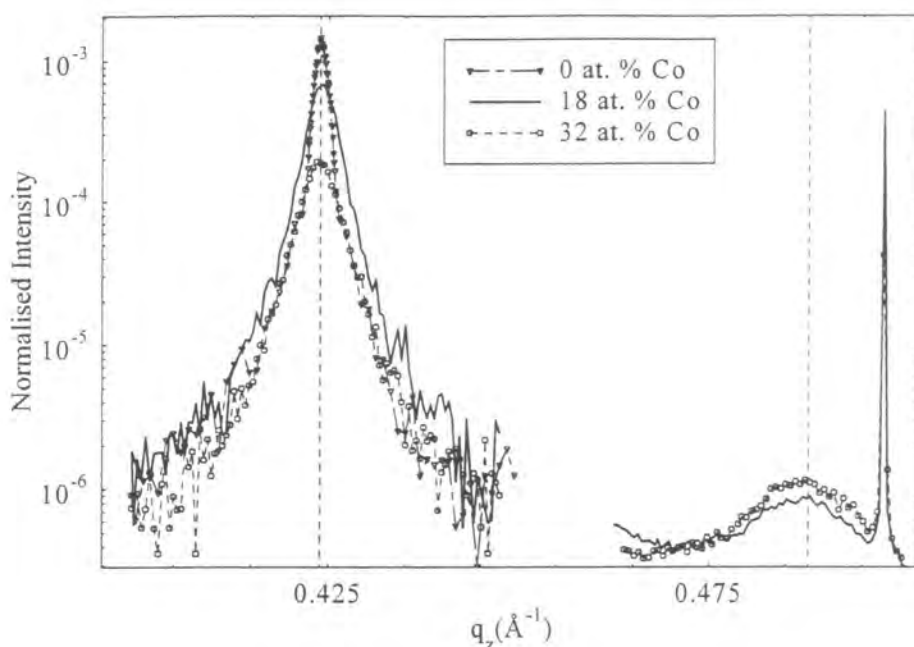
Figure 4.6 - q_z scans taken over the Ag(111) reflection (at $q_z\sim0.42\text{Å}^{-1}$) and the Co (111) reflection (at $q_z\sim0.49\text{Å}^{-1}$). Dotted lines show the positions of these reflections calculated from tabulated values. The sharp, high intensity peaks to the right of the Co reflection are stray reflections from the Si substrate.

The diffraction peaks visible at $q_z = 0.42$ and 0.49Å^{-1} arise from the fcc (111) orientated Ag and Co crystallites respectively. Within the experimental error, the positions at which these diffraction peaks occur correspond extremely well to the bulk lattice spacing for both metals, indicating little strain is present in either material. The Ag (111) reflection was measured to be at a q_z value of $0.424 \pm 0.0005\text{Å}^{-1}$ compared to a value of 0.423878Å^{-1} calculated from tabulated values. The Co (111) reflection was found to be at a q_z value of $0.4875 \pm 0.002\text{Å}^{-1}$ compared to a tabulated value of 0.487902Å^{-1}. In addition, the position of the Si(111) reflection (figure 4.5) was also in extremely good agreement with tabulated values. No change in the position of these peaks is observed between the samples, a result which is in agreement with the RHEED data.

Within the kinematical approximation, the integrated area under each Bragg peak corresponds to the amount of diffracting material present within the sample. Figure 4.7 shows the total integrated intensity under each of the diffraction peaks plotted as a function of Co concentration. These intensities, obtained from integrating the curves in figure 4.6, have been further normalised by dividing for the atomic fraction of each

material present. A constant background was also removed from each peak prior to integration.
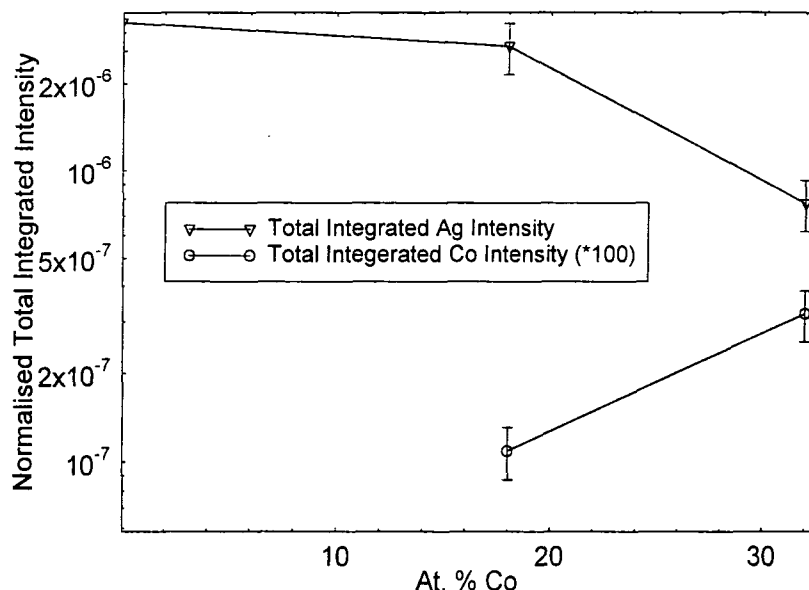

Figure 4.7 - Total integrated intensity under each of the Ag and Co (111) reflections shown as a function of at. % Co.

Given the uncertainties in the thickness of the films, the integrated intensity of the Ag(111) reflection for the pure Ag film and the $Co_{18}Ag_{82}$ granular system remains constant showing that the normalised amount of diffracting Ag does not change significantly upon the addition of 18 at. % Co. In contrast, a sharp decrease in the overall diffracted intensity from the Ag(111) reflection is seen between the $Co_{18}Ag_{82}$ and $Co_{32}Ag_{68}$ samples indicating the amount of Ag which is observed to be diffracting decreases significantly. The integrated intensity of the Co(111) reflection is seen to increase between the two granular samples demonstrating an increase in the normalised amount of diffracting Co.

While the integrated intensity represents the amount of diffracting material present in the sample, the width of the Bragg peaks in q_z depends on the vertical (out-of-plane) size of the coherently diffracting crystallites and on the local variation of the lattice spacing due to strain. Since it has already been shown that there is little overall strain in the samples it is possible to determine the size of the crystallites accurately.

In order to evaluate the peak width, each diffraction peak in figure 4.6 was fitted to a Lorentzian squared function. This function was chosen as it gave the best consistent fit to the various peaks. In the case of the Co peaks a single function was sufficient to obtain a good fit, whereas two length scales were needed to fit the Ag(111) peak (figure 4.8).
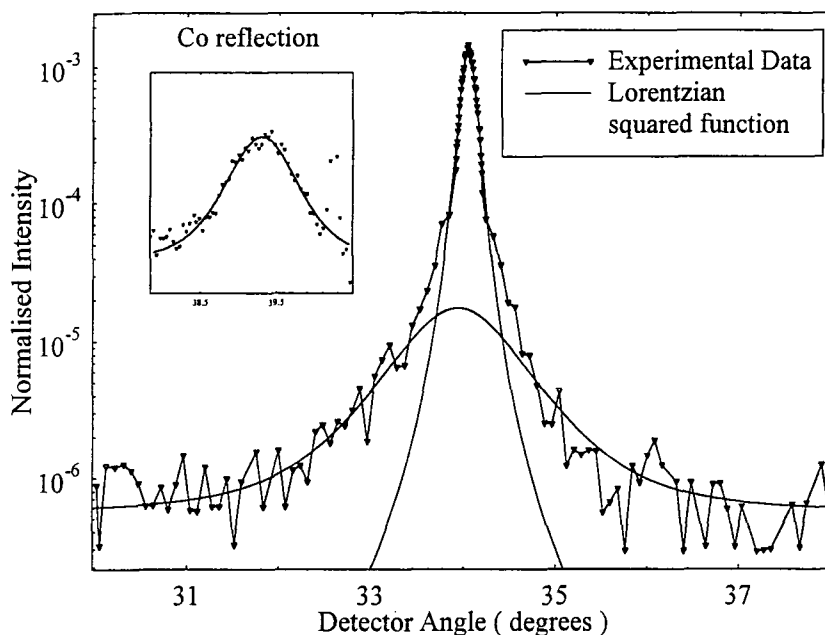

Figure 4.8 - Graph showing both the Ag and Co (inset) reflections as a function of detector angle, fitted to Lorentzian squared functions. The Ag reflection is shown on a log scale to emphasise the two length scales present.

It can be assumed that the sharp central peak in the Ag reflection arises from well oriented (111) regions and does not contain a contribution due to strain. This assumption is based on the fact that all three epitaxial films show no change of lattice spacing with respect to the bulk lattice parameter. The broad diffuse scattering is a result of local strains and dislocations within the Ag lattice. This broad contribution, on which the sharp central peak is observed to sit, begins to dominate as Co is added to the Ag film. This suggests that although overall the Ag lattice remains unstrained there is a significant increase in short range, vertical disorder as Co is added to the system. Such a diffuse hump in the Ag diffraction peaks has been observed elsewhere in similar samples by Ounadjela *et al* [22]. There, the broad peak was explained in terms of a mixing of Ag and Co crystallites. This can not be the case here since the positions of both the Ag and Co peaks are not observed to change. Instead, the inclusion of Co into

the Ag lattice must be causing localised areas of strain by vertically distorting the Ag lattice.

The extent of the crystalline grains, out of the plane, can be obtained from the fitted peaks in 2θ (the sharp central contribution in the case of the Ag). The vertical grain sizes, d_z, have been obtained using the Scherrer equation [23],

$$d_z = 0.94 \: \lambda \: / \: \delta 2\theta \: \text{x} \: \cos\theta$$

where λ is the incident wavelength, $\delta 2\theta$ the FWHM of the diffraction peak (in radians), and θ the Bragg angle of the reflection. The resulting grain sizes are shown in figure 4.9.
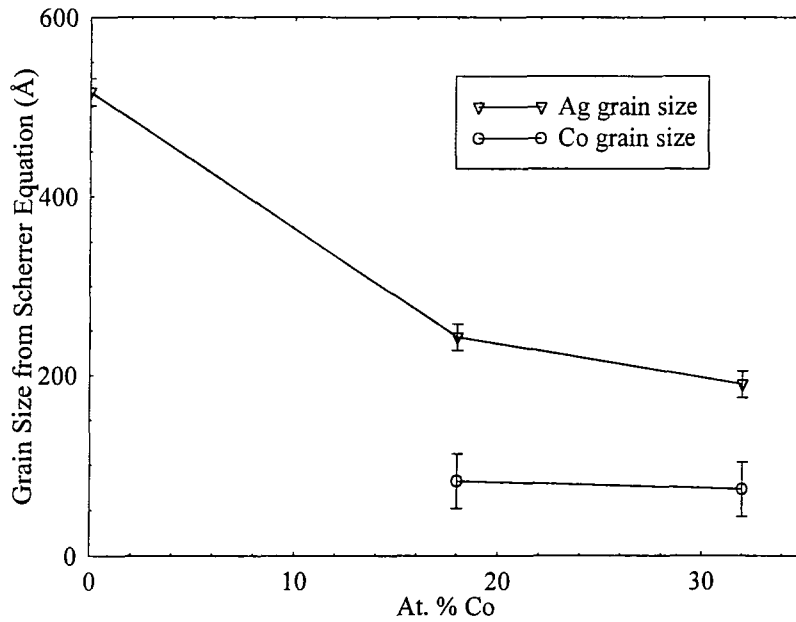
Figure 4.9 - Grain size calculated from the Co and Ag diffraction peaks shown as a function of at. % Co.

From figure 4.9 it can be seen that the calculated grain size for the pure Ag film is just over 500Å. This is comparable with the total thickness of the film calculated from both the flux monitors and x-ray reflectivity (see chapter 5). This, once again, suggests that there is no overall strain in the Ag lattice, as any strain would lead to a broadening of the diffraction peak and consequently, an underestimate of the film thickness.

Upon the addition of 18 at. % Co the vertical extent of the Ag grains is observed to crash dramatically suggesting the out-of-plane crystalline coherence of the Ag has been destroyed. However, it has already been shown that the overall amount of diffracting Ag does not change between these two samples. Since there is no change in the total amount of Ag diffracting, the lateral coherence of the Ag matrix must be conserved in this initial addition of Co.

Further addition of Co, up to 32 at. %, leads to only a small further reduction in the calculated size of the Ag crystallites. With this addition of Co, however, the observed amount of diffracting Ag reduces rapidly (figure 4.7), indicating that, in this case, the lateral coherence of the Ag matrix has also been reduced.

Within the experimental errors associated with fitting the shape of the Co peaks to a Lorentzian squared function, the vertical size of the Co crystallites is not seen to change between the 18 and 32 at. % samples. The average vertical grain size calculated for both samples is $77\pm15\text{Å}$. However, whilst it is noted that these crystallites do not grow out of the plane, the normalised amount of diffracting Co increases significantly. Such an increase can only be caused by an increase in the size of the diffracting Co regions. Since it has been shown they do not expand vertically by an amount sufficient to explain this rise in diffracted intensity, they must be spreading out in a lateral direction, in the plane of the film. Such observations have been made elsewhere [24,25] where the growth of Co grains within a Ag matrix have been investigated as a function of annealing temperature. In these studies it was shown that on annealing, the Co grains grew (as has already been shown in many other studies) but that their growth direction was predominantly along the plane of the film. This lateral growth of the Co grains and subsequent vertical degradation of the Ag lattice in these experiments is further supported by observations of strain and mosaicity within the sample.

Mosaicity was observed by study of the rocking curves taken at scattering vectors corresponding to the Ag and Co peak positions. Mosaicity is a measure of the angular spread of ordered crystallites within a sample. In contrast to a strained sample, where a variety of different Bragg conditions are present, in a sample with a high degree of mosaicity only one Bragg reflection is allowed. However, there will be several orientations of the samples surface at which these reflections occur. Consequently if the

detector is fixed and the sample rocked, a sample with a high degree of mosaicity will have a significantly wider rocking curve than one with little or no mosaic structure. Since only one Bragg condition exists there will be no change in the q_z scan for a sample with a high degree of mosaicity.

Figures 4.10 and 4.11 show the rocking curve scans taken across the Ag and Co reflections respectively. The scans are shown normalised to the film thickness and have been corrected for the footprint of the beam, which can be significant at these angles, by multiplying the raw data by $\sin(\theta)$. Figure 4.12 shows the measured trend of the FWHM of these rocking curves, obtained by fitting of the peaks to a psuedo-Voigt function.
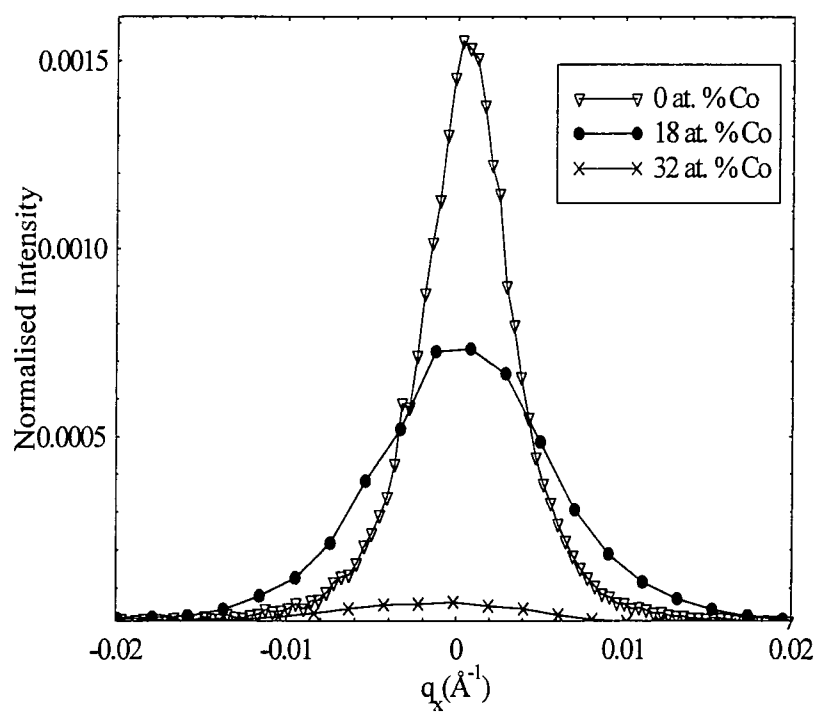
Figure 4.10 - Rocking curves taken across the Ag (111) reflection for varying Co concentrations shown as a function of q_x.
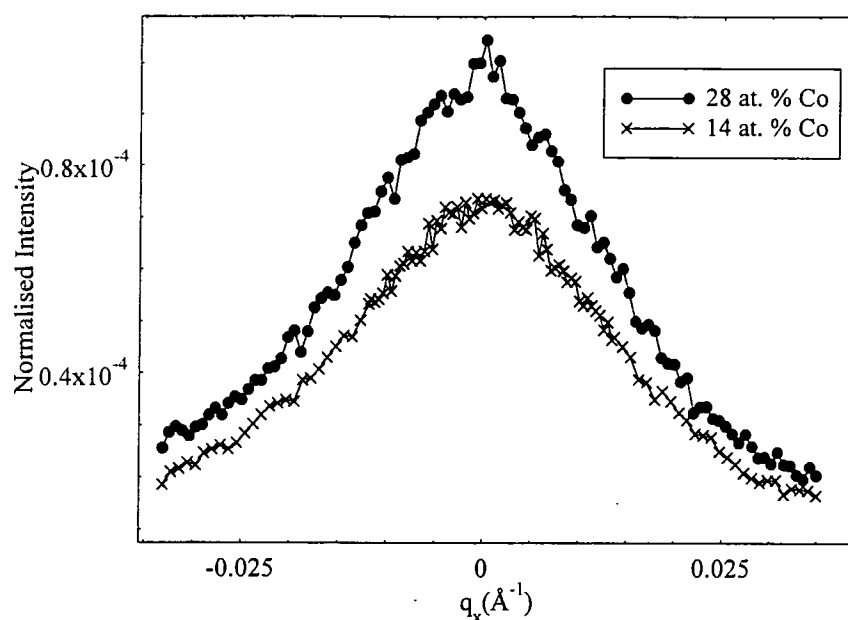
Figure 4.11 - Rocking curves taken across the Co (111) reflection for varying Co concentrations shown as a function of q_x .
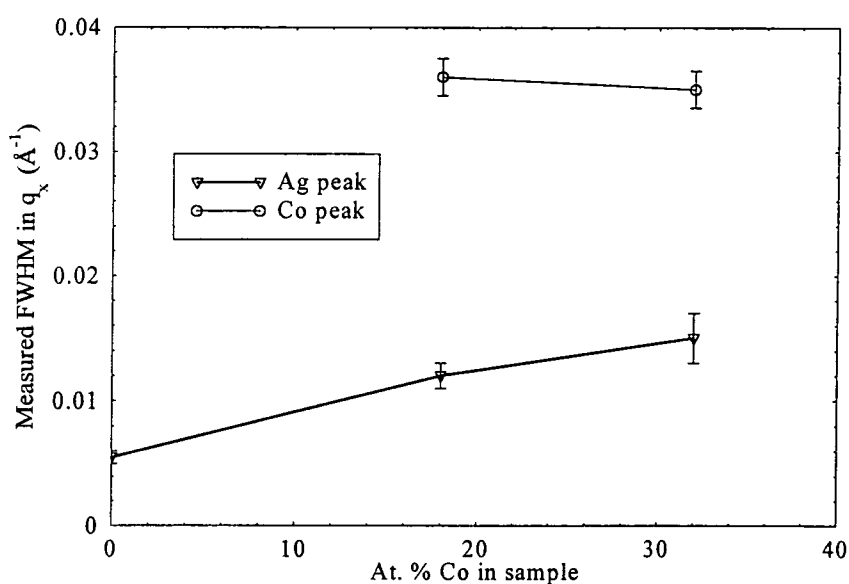
Figure 4.12 - Plot of the measured FWHM of both the Ag and Co rocking curves as a function of q_x.

From this analysis of the rocking curves it is seen that the addition of 18 at. % Co into the Ag lattice causes a large increase in the FWHM of the Ag diffraction peak. For the addition of 32 at. % Co the FWHM of the Ag peak again increases, reaching three times its initial value. This shows that the effect of adding Co to the Ag lattice is to induce a

large increase in its mosaicity. Physically, this indicates that the Ag planes within the granular samples have been disturbed in such a way as to increase their angular spread. In contrast, no change is seen in the measured FWHM of the Co rocking curves between the two granular samples showing the mosaicity must be the same between samples.

4.4 Discussion and Comparison of Results with Magnetic Data

As a starting point to this discussion it is useful to look at the pure Ag film and consider what happens when Co is added to such a system. The position of the Ag diffraction peak is in excellent agreement with the calculated value for the bulk, unstrained (111) reflection. The central part of the reflection is extremely narrow indicating the system is not highly strained. Furthermore, when the vertical grain size is calculated from the FWHM of this peak, the value obtained is just over 500Å, in good agreement with the total film thickness. This gives a further indication, along with the RHEED measurements, that the system is unstrained. A small diffuse hump is observed underneath the sharp, central peak which is attributed to a small amount of regional strains within the lattice. On the addition of Co to the sample, the contribution of this broad hump to the overall scatter increases significantly. This shows that local areas within the Ag lattice are becoming strained which would be expected due to the large lattice mismatch [26] between the Ag and Co. In addition, as the Co is added, the mosaicity of the Ag is seen to increase significantly showing the Ag planes within the sample have been disrupted by this inclusion. Furthermore, the vertical size of the diffracting Ag crystallites also drops, showing that the out-of-plane coherence of the crystallites has been destroyed.

Such effects can be explained if the Co inclusions are thought of as forming spherical inclusions within the Ag, as shown schematically in figure 4.13.
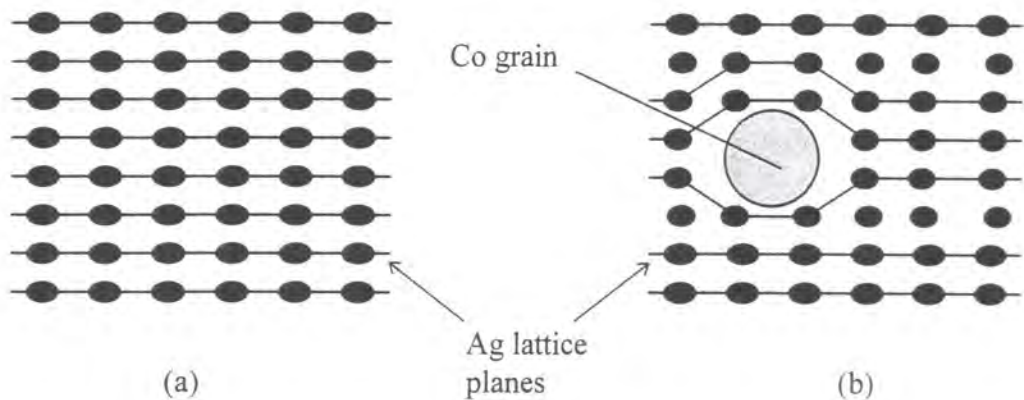
Figure 4.13 - Schematic illustration of the effect of introducing Co clusters into the Ag lattice where (a) represents the pure Ag film and (b) the 18 or 32 at. % granular film

From this schematic representation the effects of introducing Co grains into the Ag matrix can be seen. Although overall the lattice spacing of the Ag remains constant, there are small fluctuations around the grain itself. This results in an increase of localised strains and consequently the increased prominence of the broad hump sitting under the sharper Ag (111) reflection. The disruption of the Ag planes around this inclusion also explains how the mosaicity of the sample increases, as the Ag planes adopt a wide angular spread around the grain. In addition, it can be seen how the inclusion of such a Co grain serves to destroy the vertical coherence of the Ag lattice, effectively breaking it up into several parts resulting in a lower, calculated average vertical grain size.

Further evidence which supports this proposed type of inclusion can be obtained from studying the diffuse scatter around the diffraction peak. Figure 4.14 shows q_x-q_z contour maps of the Ag (111) reflection for the pure Ag film and the 18 at. % sample. These full reciprocal space maps were taken at station 16.3 of the Daresbury SRS at a wavelength of 0.8Å. These contour maps provide an excellent summary of the data presented to date, allowing the scatter to be studied simultaneously in both q directions. The data are presented normalised to the film thickness and corrected for the beam footprint by multiplying the q_x scans by $\sin(\theta)$.
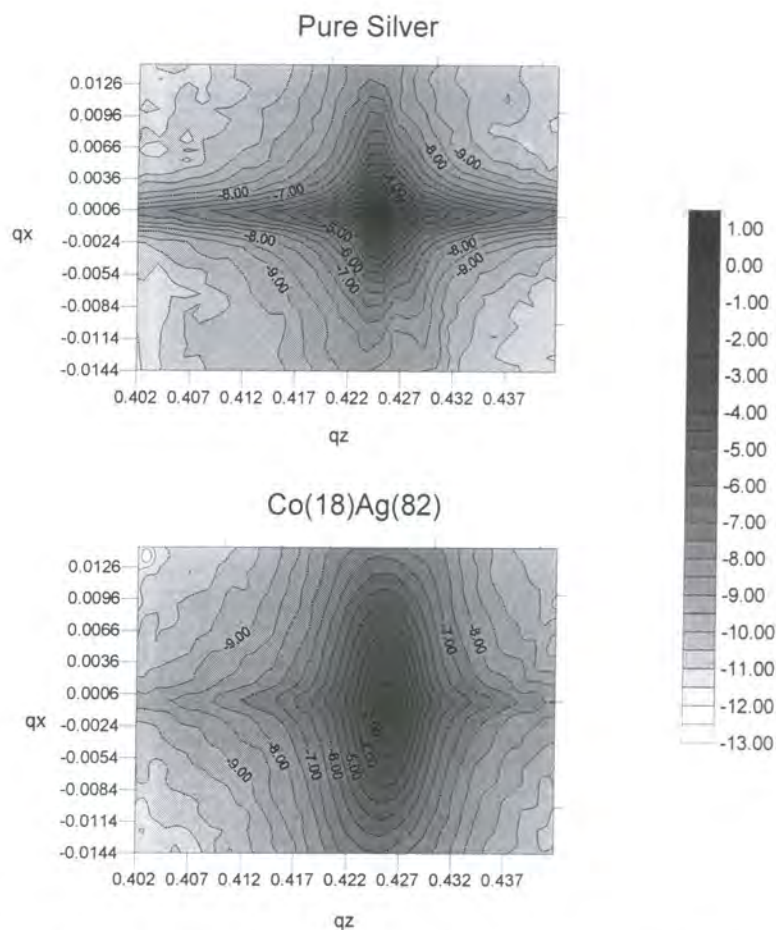
Figure 4.14 - FRSM taken around the Ag (111) reflection for two of the samples.

The FRSM for the pure Ag sample shows a sharp, well defined diffraction peak. When Co is added to the system two main effects are noticed. Firstly there is a large reduction in the intensity of the peak as has been discussed previously. Secondly, the shape of the peak become much more rounded with the observed scatter spreading out, spherically, into both q_x and q_z. Such a distribution of the scatter around the reflection is consistent with the proposed form of Co inclusion.

The inferred growth direction of these Co clusters, as more Co is added to the system, is along the plane of the film. If this was true it would be expected that the out-of-plane dimensions of the crystallites would remain constant whilst the amount of the material diffracting would increase. In addition, whilst such a development of the grains would not reduce the vertical coherence of the Ag any further, a loss of lateral coherence, reflected in a drop in the amount of Ag diffracting, would be expected. Furthermore, the growth of such grains along the plane of the film would lead to an increase in the disruption of the Ag lattice plane, in this direction, leading to an increase in the

observed mosaicity. All these arguments are entirely consistent with the data presented to date.

Magneto Optic Kerr Effect (MOKE) measurements were performed at the University of York, on both the granular films, in a longitudinal geometry. The maximum magnetic field used was 3.2kOe which was not sufficient to saturate either film. Figure 4.15 shows the MOKE curves for the two granular films as a function of applied field.
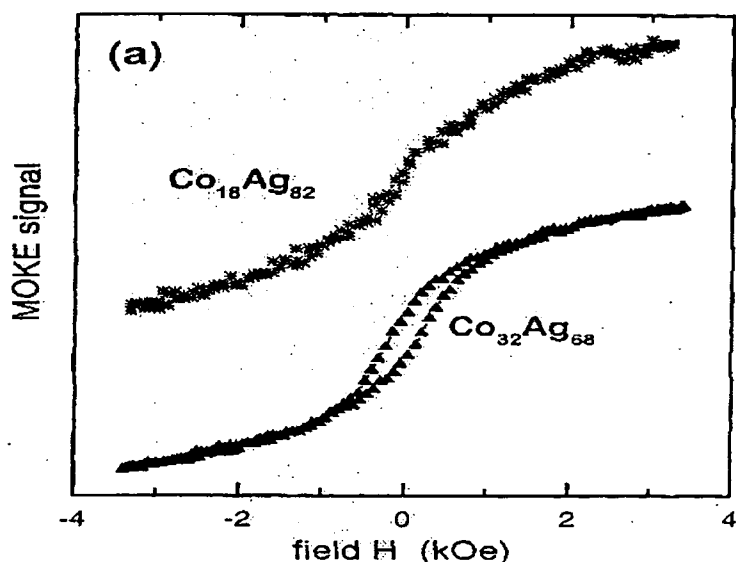
Figure 4.15 - MOKE curves taken in the longitudinal geometry for the two granular films. The thickness, as measured by the in-situ flux monitors, of the 18 and 32 at. % Co films respectively are 453Å and 370Å.

The 18 at. % sample shows superparamagnetic behaviour while for the 32 at. % sample a coercive field of approximately 180 Oe is observed. This suggests that in-the-plane of the film, the 32 at. % sample contains some larger magnetic particles which are blocked at room temperature. Such large particles are not present in the 18 at. % sample.

The magnetic data from these sample has been modelled very recently by R. W. Chantrell at the University of Bangor. The model used in these simulations is described in detail elsewhere [27]. It uses a Monte-Carlo approach in which the reversal probability is governed by a relaxation time given by the Arrhenius Neel law. This distinguishes between the superparamagnetic and ferromagnetically stable particles and means the model is able to predict both temperature and time dependent properties. The

results of detailed simulations of the magnetic data, taken on the samples at the University of York, are shown in figure 4.16.

18 at. % sample   32 at. % sample

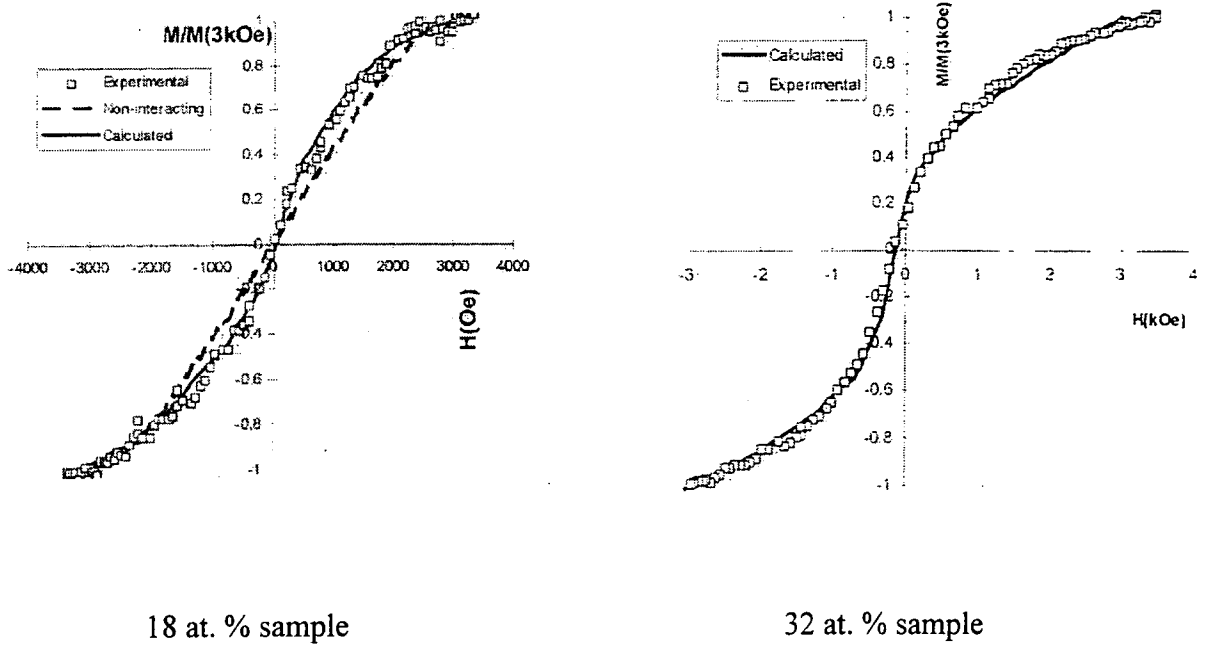Figure 4.16 - Experimental magnetic data taken from the two granular samples and the best simulated fit obtained using the model discussed above. A median Co particle diameter of 4 nm was used in modelling the 18 at. % sample whilst a range of 3 - 6 nm gave good fits for the 32 at. % sample. The difference between the non-interacting and calculated curves for the 18 at. % sample are discussed elsewhere [27].

As can be seen in figure 4.16, excellent agreement is obtained between the experimental and simulated data. Whilst a median diameter for the Co particles of 4nm was used in the simulation of the 18 at. % sample, a range of 3 - 6nm gave similarly good results for the 32 at. % sample. Detailed analysis of these simulations by S. M. Thompson of York University, indicates an in-plane elongation of the magnetic Co grains by a factor of 1.2 [28]. Such a result is in excellent agreement with the proposed growth method of the Co grains as deduced from analysis of the x-ray data.

Four point DC GMR measurements were also carried out on the samples at the University of York. The current was applied in-the-plane of the film for different orientations of the applied magnetic field upto 10kOe. The behaviour of the GMR, as a function of applied magnetic field, is shown in figure 4.17.

72
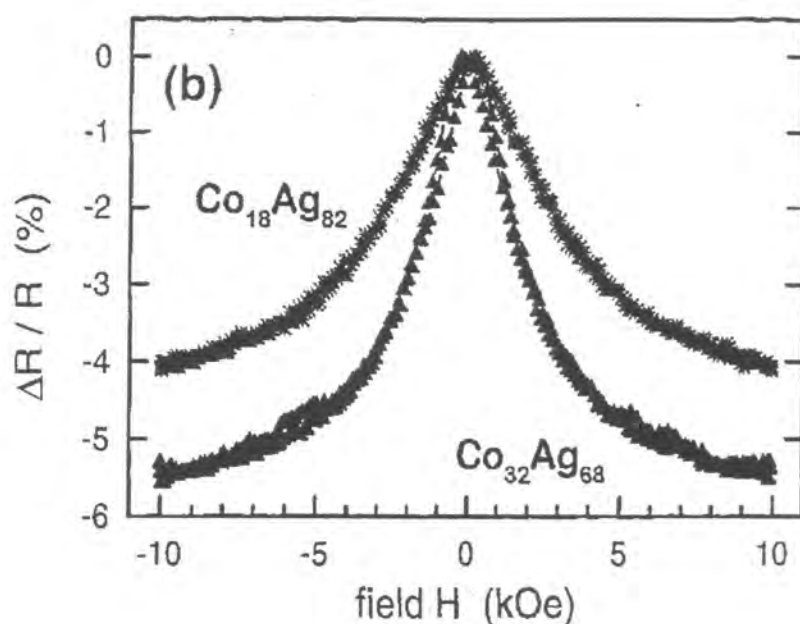
Figure 4.17 - Plot of GMR as a function of applied magnetic field.

The normalised GMR is approximately 4 and 5.5% for the 18 and 32 at. % samples respectively, the 32 at. % sample showing hysteresis in agreement with the MOKE data. With the magnetic field applied in-the-plane of the film and parallel or perpendicular to the current, no anisotropy is observed in the GMR. The shape of the GMR curves changes slightly if the field is applied perpendicularly to the sample indicating a small amount of magnetic anisotropy where the easy axis is perpendicular to the film plane.

The fact that the GMR increases slightly with increasing Co concentration and particle size, suggest that the increased spin depolarisation due to the poorer texture of the Ag matrix (reducing the GMR) is compensated for by the smaller grain separation of the Co grains (enhancing the GMR). Once again, this behaviour is entirely consistent with the mode of growth of the Co clusters, proposed from analysis of the x-ray data.

4.5 Conclusions

A detailed HRXD study has been carried out on a series of CoAg granular films. Careful analysis of the scatter around the Ag and Co (111) diffraction peaks in these samples has allowed a growth method for the Co clusters to be determined. All three samples, grown by MBE, are found to be unstrained and extremely well (111) ordered. It is observed that the Co forms grains of ~77Å in height within the film which consequently destroy the out-of-plane crystalline coherence of the Ag lattice. The vertical dimensions of the Co grains are not seen to change as the amount of Co in the system increases. The additional Co causes the grains to elongate along the plane of the film thus destroying the lateral coherency of the Ag matrix, as well as the vertical.

This lateral expansion of the Co grains causes a significant increase in the mosaicity of the Ag and also increases the localised strains within the Ag matrix although, overall, the entire structure remains unstrained.

This proposed form of growth is seen to agree extremely well with magnetic measurements taken on the granular samples. MOKE curves indicate the presence of large particles in the 32 at. % sample whereas none are observed when the Co concentration is only 18 % and detailed simulations of torque magnetometry data indicate an elongation of the Co grains in-the-plane of the sample by a factor of 1.2. Additionally, a higher GMR is measured for the 32 at. % sample showing the increase in lateral grain size, and consequently the reduction of the grain separation, has led to such an increase in the GMR.

References for Chapter 4

[1] G. Binasch, P. Grunberg, F. Saurenbach and W. Zinn Phys. Rev. B **39** *4828* (1989)

[2] M. N. Baibich, J.M. Broto, A. Fert, F. Nguyen Van Dau, F. Petroff, P. Etienne, G. Creuzet, A. Friederich and J. Chazelas Phys. Rev. Lett. **61** *2472* (1988)

[3] S. S. P. Parkin Appl. Phys. Let. **60** *512* (1992)

[4] V. S. Speriosu, B. Dieny, P. Humbert, B. A. Gurney and H. Lefakis Phys. Rev. B **44** *5358* (1991)

[5] B. Dieny J.M.M.M **136** *335* (1994)

[6] A. E. Berkowitz, J. R. Mitchell, M. J. Carey, A. P. Young, S. Zhang, F. E. Spada, F. T. Parker, A. Hutten and G. Thomas Phys. Rev. Lett. **68** *3745* (1992)

[7] J. Q. Xiao, J. S. Jiang and C. L. Chien Phys. Rev. Lett. **68** *3749* (1992)

[8] B. Abeles, P. Sheng, M. D. Couts and Y. Arie Adv. Phys. **24** *407* (1975)

[9] J. R. Childress, C. L. Chien and M. Nathan Appl. Phys. Lett. **56** *95* (1990)

[10] J. R. Childress and C. L. Chien J. Appl. Phys. **70** *5885* (1991)

[11] M. Hansen in *'Constitution of Binary Alloys'* (McGraw-Hill, New York, 1958)

[12] M. L. Watson, J. A. Barnard, S. Hossain and M. R. Parker J. Appl. Phys. **73** (1993)

[13] A. H. Morrish in *Physical Principles of Magnetism* (Wiley, New York, 1965)

[14] I. S. Jacobs and C. P. Bean in *Magnetism III* (Academic, New York, 1963)

[15] C. L. Chien, J. Q. Xiao and J. S. Jiang J. Appl. Phys. **73** (10) *5309* (1993)

[16] J. Q. Xiao, J. S. Jiang and C. L. Chien Phys. Rev. Lett. **68** (25) *3749* (1992)

[17] S. S. P. Parkin, R. F. C. Farrow, T. A. Rabedeau, R. F. Marks, G. R. Harp, Q. Lam, C. Chappert, M. F. Toney, R. Savoy and R. Geiss Europhys. Lett. **22** (6) *455* (1994)

[18] A. E. Berkowitz, J. R. Mitchell, M. J. Carey, A. P. Young, S. Zhang, F. E. Spada, F. T. Parker, A. Hutten and G. Thomas Phys. Rev. Lett. **68** (25) *3745* (1992)

[19] B. Dieny J. Phys. C **4** (40) *8009* (1992)

[20] S. M. Thompson *et al* Phil. Mag. B **68** (6) *923* (1993)

[21] http://www-users.york.ac.uk/~phys18/GROWTH.htm

[22] K. Ounadjela, S. M. Thompson, J. F. Gregg, A. Azizi, M. Gester and J. P. Deville Phys. Rev. B **54** (17) *12252* (1996)

[23] A Guinier *X-Ray Diffraction in Crystals : Imperfect Crystals and Amorphous Bodies* (Dover Publications Ltd., New York, 1994)

[24] H. Sang, N. Xu, J. H. Du, G. Ni, S. Y. Zhang and Y. W. Du Phys. Rev. B **53** (22) *15023* (1996)

[25] H. Sang, S. Y. Zhang, H. Chen, G. Ni, J. M. Hong, X. N. Zhao, Z. S. Jiang and Y. W. Du Appl. Phys. Lett. **67** (14) *2017* (1995)

[26] S. S. P. Parkin, R. F. C. Farrow, T. A. Rabedeau, R. F. Marks, G. R. Harp, Q. Lam, C. Chappert, M. F. Toney, R. Savoy and R. Geiss Europhys. Lett. **22** (6) *455* (1993)

[27] M. El-Hilo, R. W. Chantrell and K. O'Grady J. Appl. Phys. **84** (9) *5114* (1998)

[28] S. M. Thompson, University of York - *private communication*

Chapter 5 - The Influence of Step-Bunching on Grazing Incidence Diffuse X-Ray Scattering

A series of grazing incidence x-ray scattering measurements have been performed on a pure Ag film and on two CoAg granular films all grown on vicinal Si (111) wafers. Full reflectivity profiles were taken for each sample as a means of characterising their thickness and effective roughness. An asymmetry was observed in the diffuse scatter for two of the samples and a detailed investigation of this asymmetry was performed. The characterisation of each of the samples is presented and the asymmetry is discussed is terms of step-bunching of the Si substrate.

5.1 Introduction

It has been well documented in recent years that under specific conditions Si(111), misorientated towards certain crystallographic orientations, will undergo the process of step-bunching [1-3]. The form of the step-bunched surface is generally described as consisting of long terraces, orientated along the (111) direction, split by bunches of monatomic steps in the surface. An example of the structure of such a surface is given in figure 5.1 where a reflection electron microscopy (REM) image of a step-bunched Si (111) surface is reproduced [1].

The presence of step-bunching on the surface of Si (111) was predicted and identified over 10 years ago from studies of the orientational stability of vicinal Si surfaces [1]. Vicinal surfaces are those which have been cut by a few degrees away from a low index crystallographic orientation. They are favoured in many growth areas as they are often quite thermally stable.
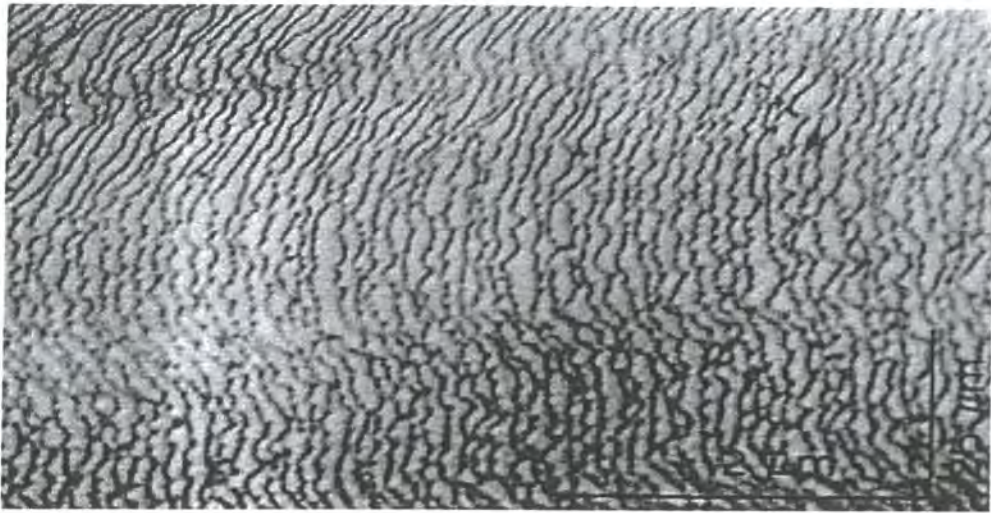
Figure 5.1 - REM image of a step-bunched Si (111) surface, from [1]. The presence of long, flat terraces (white) interspersed with short steps (black) can be clearly seen.

A lot of the early work into the step-bunching of Si was carried out in the late 1980's by Bartlet and Williams [2,3] who were interested in the orientational stability of various Si surfaces. They concluded that when a vicinal Si (111) wafer undergoes its 7x7 reconstruction, step-bunching occurs on its surface. Several structures were proposed for such a step-bunched surface which were dependent on the direction and angle of the offcut and the temperature to which the sample was heated. Several models were proposed for this temperature-induced faceting, discussing the changes in the surface structure in terms of the equilibrium crystal shape. The details of such models are not relevant to the discussions here, apart from demonstrating that the process of step-bunching in vicinal Si (111) is relatively well understood.

As the experimental techniques available to study surfaces in detail improved, further work into the step-bunching of Si occurred. Atomic force microscopy (AFM) and scanning tunnelling microscope (STM) studies of such surfaces [4,5] confirmed the presence of long, flat terraces and bunched regions of atomic steps on the 7x7 reconstructed Si (111) surface. Later work also began to address the exact shape and form that these step-bunched regions took [6] and the effect, on the bulk properties of the sample, of depositing layers [7-10]. In particular the growth and study of giant magnetoresistive devices [11,12] grown on such structured surfaces has become a very active area. Since the physics of the step-bunching is quite well understood, it is possible, by varying the miscut angle of the vicinal surface and the heating treatment of

the substrate, to engineer the period and overall form of the step-bunches. Magnetic thin films, deposited subsequently onto such surfaces, are found to have very different properties when the current in the film is applied either parallel or perpendicular to the direction of the steps. Consequently, by altering the miscut angle and thermal treatment of the initial substrate, the magnetic properties of films deposited onto such surfaces can be controlled.

Alongside these developments in the understanding of Si (111) step-bunching, a number of reports have documented the presence of asymmetries in grazing incidence diffuse x-ray scattering experiments where the asymmetries have been attributed to the presence of terraced structures on the surface of the samples [7,13,14]. Previous experiments have been carried out at the University of Durham studying Co / Cu superlattices grown by molecular beam epitaxy (MBE) on $CuSi_3$ buffered (001) Si substrates [15]. In these experiments, a sharp peak was observed in the diffuse scatter whilst rocking the sample at a fixed scattering vector and this peak was seen to be offset from the specular scatter. In addition, it was noted that this offset varied upon rotation of the sample about its surface normal. The diffuse scatter data could be fitted extremely well to a model of the interfaces based on the fractal model proposed by Sinha [16], and since, by definition, a single, regular stepped surface is not fractal, it was suggested that the diffuse scatter must therefore originate from non-uniformly bunched steps on the surface of the sample [17].

In the studies presented here similar, but more detailed observations, have been made on single layers grown on an offcut Si(111) substrate which has been subject to conditions comparable with those known to induce step-bunching [11,12]. Since this is a relatively simple system to study, it has been possible to affirm the original identification of the origin of the asymmetry in the diffuse scatter. In addition these studies confirm the fact that under the correct growth conditions, offcut Si(111) does indeed undergo step-bunching and such an effect can be readily observed by x-ray scattering even after deposition of a thin film.

5.2 Experimental

5.2.1 Description of Sample Fabrication

The three samples studied in these experiments are those previously discussed in chapter 4. They consist of two Co / Ag granular films with 18 and 32 atomic % (at. %) Co respectively and a single layer of Ag. All three samples were grown, at the University of York, on vicinal Si (111) substrates which had been offcut by 0.1° from the (111) orientation. Prior to deposition of the sample the substrates were heated under ultra high vacuum until the 7x7 reconstruction could be observed by in-situ RHEED measurements. During deposition the substrates were maintained at an elevated temperature of 150°C. Whilst these fabrication methods were actually chosen to enhance the growth of the granular films, as discussed in chapter 4, they are crucial to the discussions that follow in this chapter as well. For a more detailed description of their fabrication the reader is referred to section 4.3.1 of the previous chapter.

5.2.2 Description of the X-Ray Measurements

A series of grazing incidence scattering experiments were performed on these samples on both stations 16.3 and 2.3 of the Daresbury SRS. A conventional reflectivity set-up, as discussed in chapter 3, was used on both stations.

Initially, typical reflectivity profiles were obtained for each sample with specular and off-specular scans being taken, along with transverse diffuse scans. These experiments were performed on station 16.3 where a wavelength of 0.8Å was selected, being the maximum flux for the station. An in-depth study of the pure Ag film was subsequently carried out after the observation of asymmetry in the diffuse scatter. In this series of experiments it was important to study the sample at a variety of azimuthal rotations about its surface normal. In order to achieve this, a rotation stage was modified such that it could be fitted onto the usual mount on the θ axis of station 2.3. This rotation stage

allowed manual rotation of the sample about its surface normal to a resolution of ±0.5° which was sufficient for the needs of this experiment.

Transverse diffuse scans were taken at each of the chosen azimuthal angles and specular scans were also taken at a selection of these angles. In addition, a number of transverse diffuse scans were taken at a fixed azimuthal angle for a variety of scattering vectors. In this way a detailed investigation of the diffuse scatter was carried out. All these rotation experiments were carried out on station 2.3 where a wavelength of 1.54Å was used.

5.3 Presentation of Experimental Data

These data will be presented in two sections. Firstly, by way of an introduction to the samples, and to provide a complete picture for chapter 4, the specular data will be presented along with the best fit simulations used in their characterisation. A brief discussion of these results will be presented alongside the data. Secondly, the detailed study of the diffuse scatter from the pure Ag film, on which this chapter concentrates, will be presented.

5.3.1 Specular Data

Specular and off-specular scans taken at 0.8Å are presented for each of the three samples along with the best fit simulation obtained to the true specular scatter. All the simulations obtained were generated using the Bede REFS simulation program with identical instrument parameters, characteristic of the station.
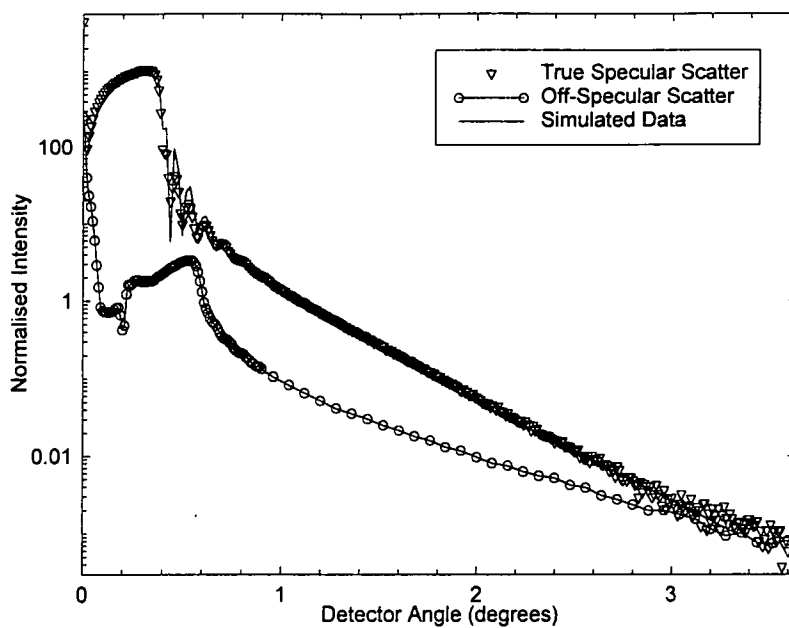
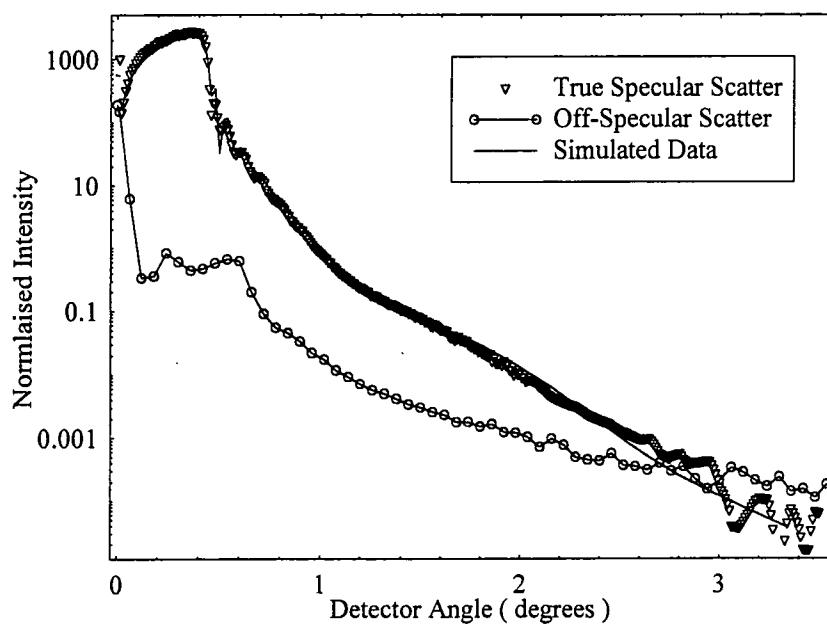Figure 5.2 - Experimental and Simulated Data for the Pure Ag Film

Figure 5.3 - Experimental and Simulated Data for the 18 at. % Granular Film
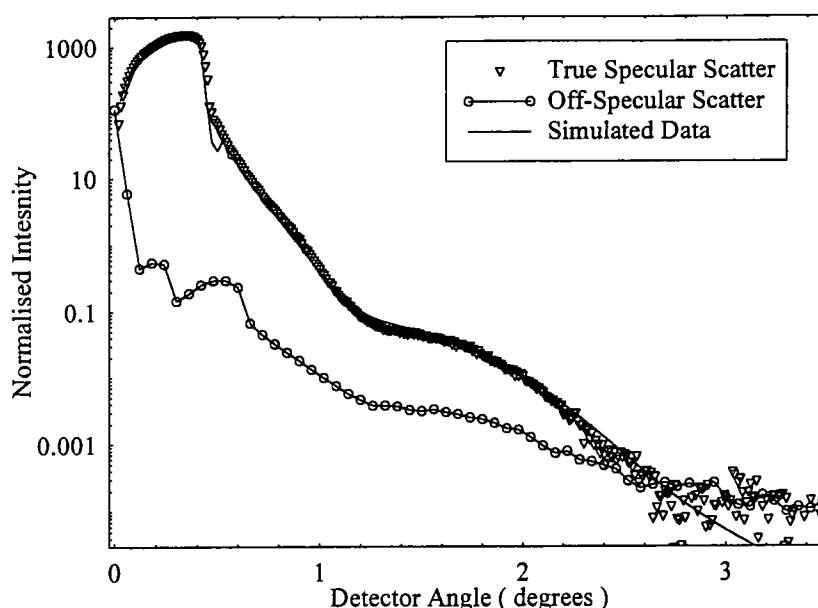
Figure 5.4 - Experimental and Simulated Data for the 32 at. % Granular Film

As can be seen, excellent agreement is obtained between experimental and simulated data for all three samples. The only discrepancy is the presence of a weak Keissig fringe in the simulation of the 32 at. % sample whereas no such fringe is observed in the experimental data. This is attributed to the extreme overall roughness of the surface of this sample which can not be completely replicated in the simulation program.

The parameters obtained from these simulations are shown below. σ is the mean interface width of the surface or interface (as discussed previously in chapter 2), d is the thickness of the layer and ρ represents the density of the layer in question. For the case of the granular films an alloy of Ag and Co, with the correct weighting, has been specified and the value of this alloys bulk density varied.

Pure Ag Film

Si	-	$\sigma = 3.8 \pm 0.4$Å
Ag	$d = 420 \pm 2$Å	$\sigma = 30 \pm 2$Å [$Ag_\rho = 70\%$ bulk]

18 at. % Sample

Si	-	$\sigma = 4.5 \pm 0.5\text{Å}$	
Ag$_{50}$Co$_{50}$	$d = 21 \pm 3\text{Å}$	$\sigma = 8.2 \pm 0.5\text{Å}$	[(Ag$_{18}$Co$_{82}$)$_\rho$ = 38% bulk]
Ag$_{18}$Co$_{82}$	$d = 360 \pm 5\text{Å}$	$\sigma = 34 \pm 2\text{Å}$	[(Ag$_{18}$Co$_{82}$)$_\rho$ = 93% bulk]

32 at. % Sample

Si	-	$\sigma = 4.5 \pm 0.5\text{Å}$	
Ag$_{50}$Co$_{50}$	$d = 22 \pm 3\text{Å}$	$\sigma = 8.2 \pm 0.5\text{Å}$	[(Ag$_{32}$Co$_{68}$)$_\rho$ = 45% bulk]
Ag$_{32}$Co$_{68}$	$d = 520 \pm 50\text{Å}$	$\sigma = 45 \pm 5\text{Å}$	[(Ag$_{32}$Co$_{68}$)$_\rho$ = 96% bulk]

From these simulated results several points need to be made. Firstly the thickness of the pure Ag film and the 18 at. % granular sample have been accurately determined by matching the period of the Keissig fringes in the true specular scatter. The lack of Keissig fringes in the 32 at. % sample is due to the very rough nature of the surface of this sample, meaning the thickness obtained has a much higher associated error. Consequently, it is not possible to get a full set of thickness values for these samples. These problems have been discussed previously, in chapter 4, with regard to the normalisation of the high angle diffraction data from these samples. Overall roughness values have been successfully obtained for all the layers by accurately matching the fall in the true specular intensity in the samples.

Two points of interest arise from these studies with regard to the observed densities of the layers. The pure Ag film can only be fitted if the density of the Ag layer is assumed to be 70% of its nominal bulk value of 10.5 g/cm^3. This is demonstrated in figure 5.5 where a comparison of two simulations at 100% and 70% bulk density are shown. The physical explanation of such an effect most probably lies in the presence of holes within the Ag layer. The specular scatter is then giving an average density of the Ag and holes present.
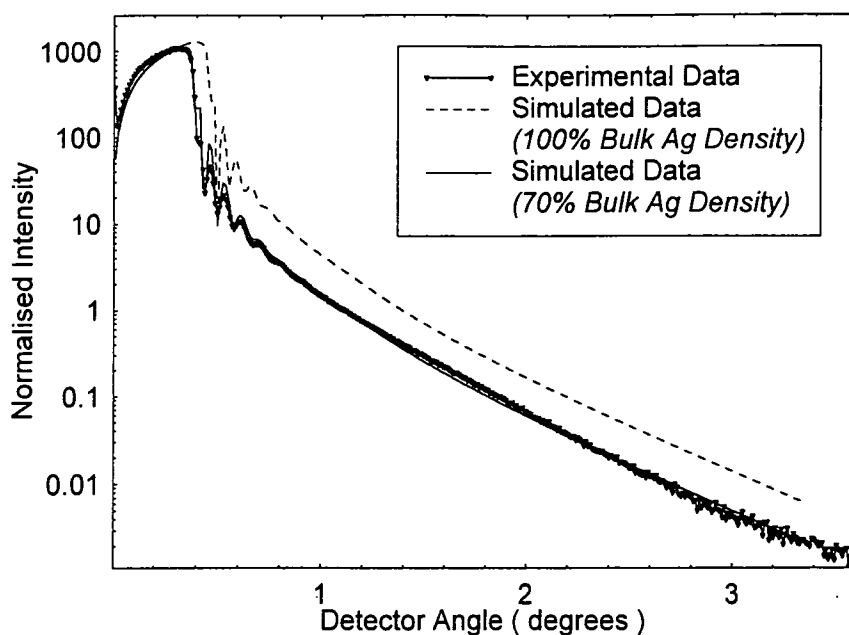
Figure 5.5 - Comparison of Simulations of the Pure Ag Film

The second point of interest comes from the simulation of the granular films. In both cases a thin, low density layer of the nominal CoAg alloy observed. The density of this film, which is ~20Å thick in both samples, is around 40% of the bulk density. In contrast, the majority of the Co / Ag granular film is observed to have a density very close to the bulk value expected.

5.3.2 Transverse Diffuse Data from the Ag Film

Transverse diffuse scans were taken for each sample at similar scattering vectors. Figure 5.6 shows these scans, normalised in q_x allowing a more direct comparison of the form of the scatter.
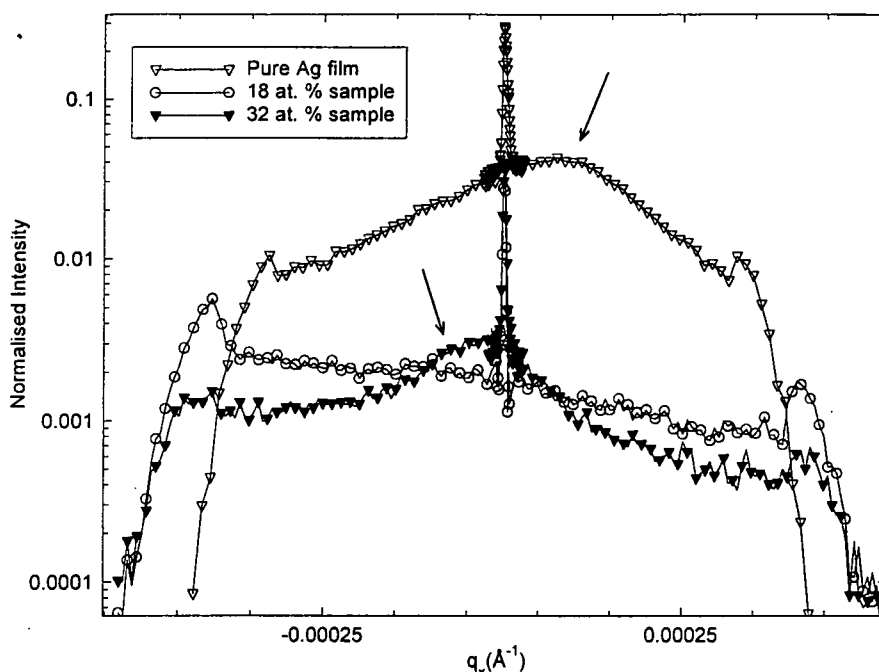
Figure 5.6 - Transverse diffuse scans, shown as a function of q_x, for each of the three samples. The arrows indicate the position of the asymmetry in the diffuse scatter.

It is immediately apparent that for two of the samples, namely the pure Ag film and 32 at. % granular film, an asymmetry exists in the detected scatter. In both cases the broad peak in the diffuse scatter is offset from the sharp specular ridge at $q_x = 0$. The offset peak occurs on different sides of the specular ridge for the two samples and no offset peak is seen at all for the 18 at. % sample and, indeed, there is no clear peak in the diffuse scatter at all when compared to the other two samples.

Following the observation of this asymmetry, a detailed investigation was carried out on the pure Ag film. This sample was chosen as it possessed the simplest structure and consequently was the most simple to model. Figure 5.7 shows two transverse diffuse scans taken from the pure Ag film at two azimuthal angles. The first scan is taken at a 0° orientation, the orientation at which all the previous data on this sample had been taken, and the second is taken after rotating the sample by 180° about its surface normal.
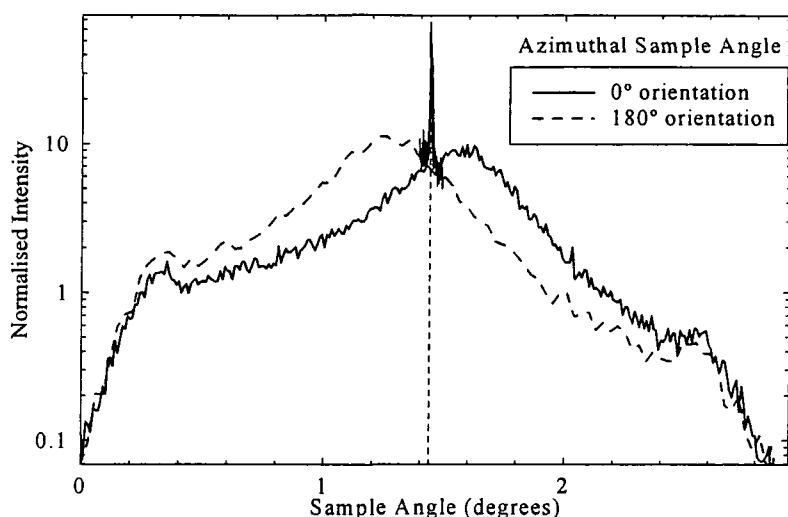
Figure 5.7 - Transverse diffuse scans shown for the pure Ag film taken at a fixed scattering vector but with the sample rotated 180° around its azimuth. The position of the specular ridge is marked by the dotted line.

Once again, a broad peak is observed in the diffuse scatter which is offset from the sharp specular peak. It is observed that when the sample is rotated by 180° about its azimuth, the position of the offset peak shifts to the opposite side of the specular ridge. Whilst this offset peak is seen to move, the specular ridge does not change in position, but lies midway between the Yoneda wings, which do not change their position either.

Starting with the sample mounted at its 0° orientation, transverse diffuse scans were taken for every 45° of azimuthal angle and the position of the offset diffuse hump was measured with respect to the specular ridge. Figure 5.8 shows how the position of the offset peak changes as a function of azimuthal angle. It is observed, from figure 5.8, that the peak in the diffuse scatter precesses sinusoidally around the specular peak exhibiting a maximum offset of 0.13 ± 0.02°. In this series of measurements neither the Yoneda wings or the specular peak change in position as the sample was rotated.
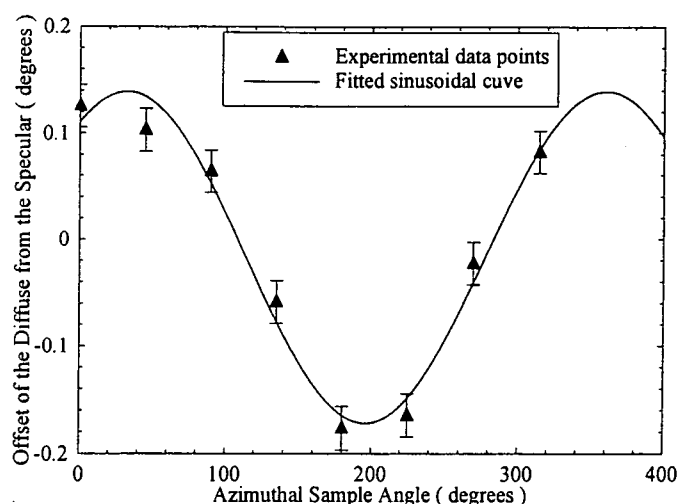
Figure 5.8 - Position of the offset diffuse peak with respect to the specular ridge as a function of sample azimuthal angle. The data points have been fitted to a sinusoidal function.

Transverse diffuse scans as a function of scattering vector are shown in figure 5.9. From these data it was observed that there is no offset peak visible in the diffuse scatter at low scattering vectors. As the scattering angle is increased, the offset diffuse peak becomes increasingly prominent, the most intense offset peak being observed at the highest scattering vector.

Figure 5.9 - Series of transverse diffuse scans taken as a function of scattering vector at a fixed sample azimuth.

Simulations of this experiment have been undertaken using the Bede GIXS code, the theory behind which has been described in chapter 2. This code has been phenomenologi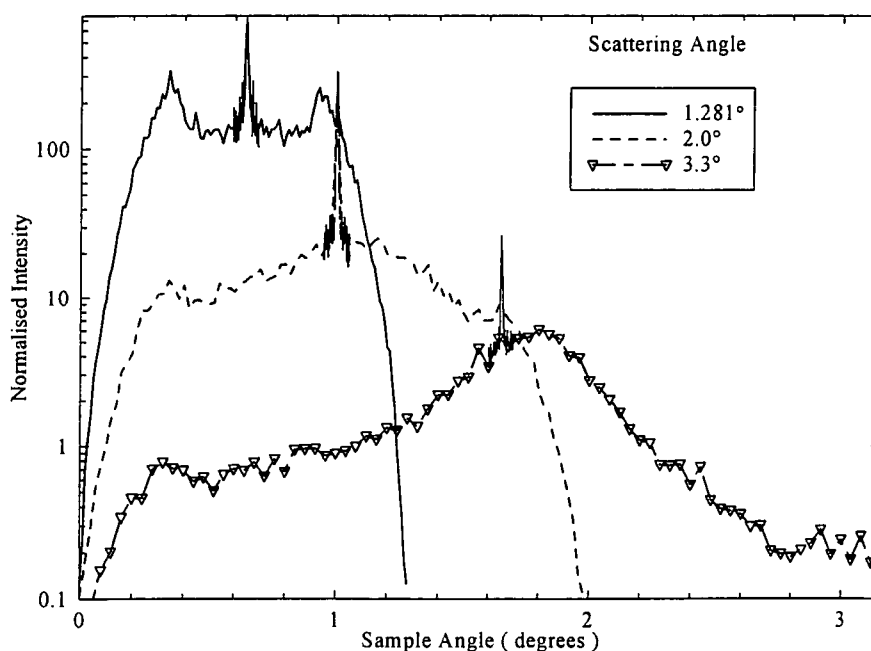caly modified, by M. Wormington of Bede Scientific, to include different correlation lengths between interfaces and also allows a terrace angle to be specified for the substrate. This terrace angle is defined to be the angle between the average plane of the interface and the mean surface of the terraced regions. This is achieved within the code by calculating the electric fields with respect to the mean interface position but calculating the wavevectors, and corresponding scattering vectors, relative to the terraces. Full details on this modification can be found elsewhere [17].

Figure 5.10 shows simulated transverse diffuse scans, obtained using this modified code, taken at identical scattering vectors to those in the figure 5.9.
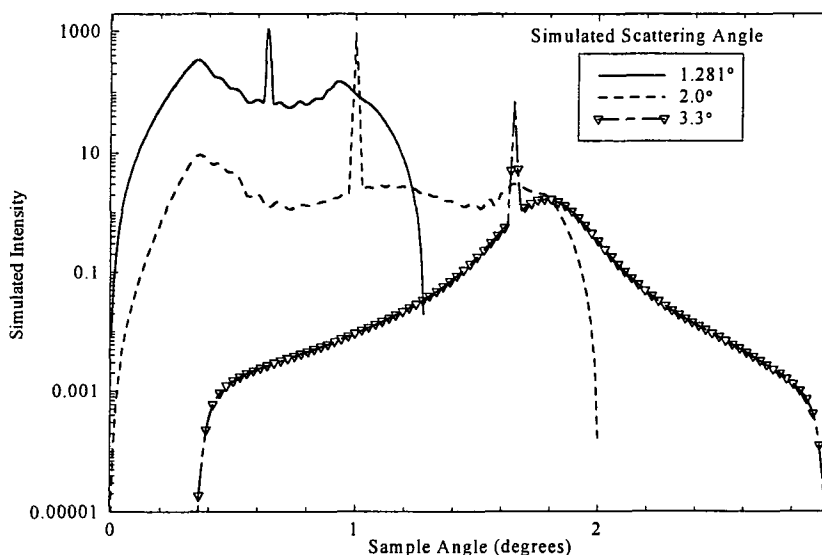
Figure 5.10 - Simulated transverse diffuse scan taken at identical scattering vectors to those obtained in the experiment.

As can be seen, there is excellent agreement in the overall shape of these scans when compared with the experimental data. No offset peak in the diffuse scatter is observed at low scattering vectors, but as the scattering angle is increased, so the peak in the diffuse scatter becomes more prominent.

These simulations were obtained using top and bottom surface correlation lengths of 1000Å and 3000Å respectively and a fractal parameter of 0.8. In addition a terrace angle

of 0.139° was specified in order to accurately match the position of the offset diffuse peak.

The effect of using these two correlation lengths is show in more detail in figure 5.11 where a simulation of the low scattering angle diffuse scan is shown.
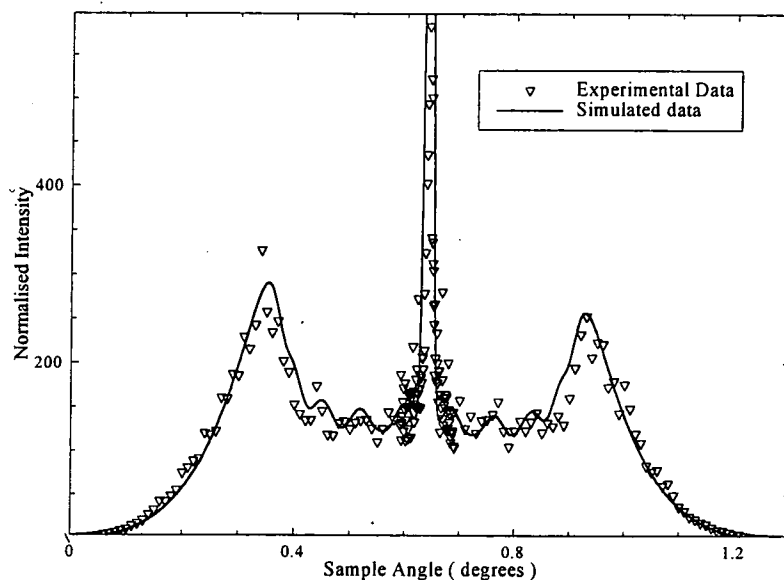
Figure 5.11 - Simulated transverse diffuse scan for a scattering angle of 1.281°

As is demonstrated in this figure, excellent agreement is obtained between the simulated and experimental data. The parameters used were the same as those used to obtain the specular best fit simulation but with the two correlation lengths just discussed. It should be noted that it is not possible to fit any of the transverse diffuse scans, where an offset in the diffuse scatter is observed, if a single correlation length is assumed. This is in sharp contrast to the 18 at. % granular film where there is no offset in the diffuse scatter. In this case only a single correlation length is needed to obtain a good fit to the experimental data, as shown in figure 5.12.
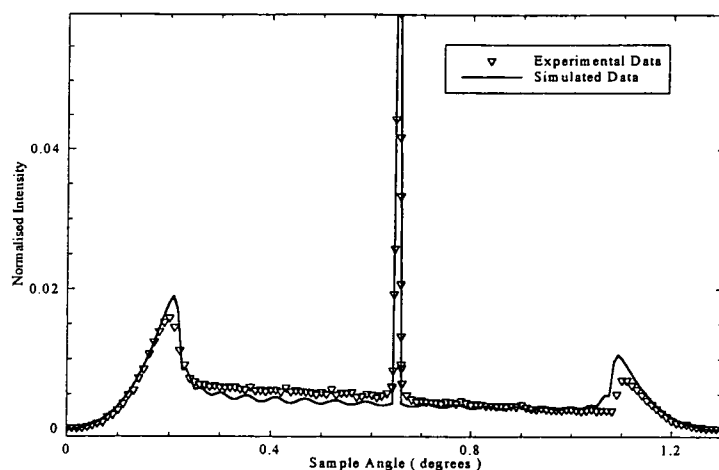
Figure 5.12 - Experimental and simulated transverse diffuse data from the 18 at. % granular film taken at a scattering angle of 1.3°

Here, identical parameters to those obtained from the specular simulations were used (figure 5.3) but only a single correlation length of 1000 ± 20Å was necessary to obtain the fit.

Ideally it would also be possible to determine the level of out-of-plane conformality in the roughness by modelling the diffuse scatter. In this case, however, it was not possible to do so. Simulations show that for large difference in roughness present between lower and upper surfaces (here 3 and 30Å respectively) identical, very weak Keissig fringes occur in the off-specular scatter for both highly correlated and uncorrelated roughness, as demonstrated in figure 5.13

Figure 5.13 - Simulated off-specular scans for the single Ag layer. All parameters are as used in the specular simulation with the type of interfaces varied from being totally correlated to totally uncorrelated.

Although the presence of Keissig fringes in the off-specular scatter is normally an indication of a high degree of out-of-plane conformality in the roughness the present case is an important exception.

5.4 Discussion and Conclusions
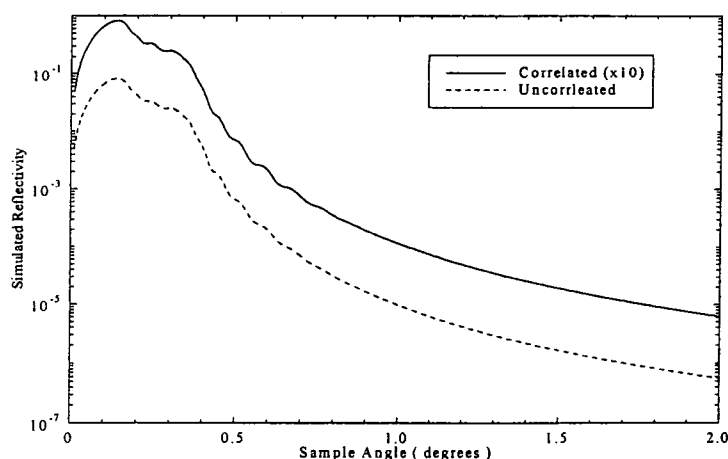
The presence of asymmetries in the diffuse scatter has been observed previously by several other groups. In all these previous cases the asymmetry has been ascribed to a preferential orientation of roughness at the interfaces and by implication, terracing within the layers. As the specular scatter arises from the average plane of these terraced regions the effect of terracing is to introduce an offset between the diffuse and specular components. In the previous studies, the diffuse scatter was concentrated into two symmetric peaks on either side of the specular ridge [18-20]. These are characteristic of lateral periodicities on interfaces within the sample, which give rise to this diffraction grating effect. In the case of these studies, however, only a single peak was observed, implying that no regular periodicities exist on the interfaces. Furthermore, whereas previous studies found that the diffuse scatter exhibited a marked difference in shape along the q_x axes, the shape of the diffuse scatter from the silver sample was invariant as a function of azimuthal angle and just shifted in position. The constancy of the shape of this scatter implies an isotropic distribution of roughness length scales on the interfaces. This behaviour is very similar to that observed previously by the Durham group on a series of Co/Cu multilayers grown by MBE on Si (111) using a Cu_3Si buffer [17] and also by other groups [21].

The above observations are best described by a substrate which has undergone step-bunching. In this case the diffuse scatter arises from local, isotropically rough, bunched regions separated by long terraces and which are at an angle to the average interface, as represented schematically in figure 5.14.
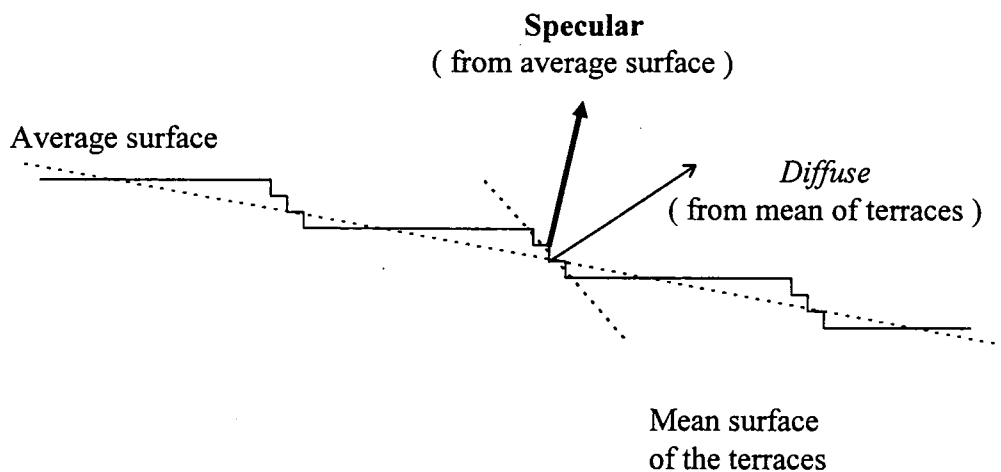
Figure 5.14 - Schematic representation of step-bunching of the Si surface

These bunched regions can have the fractal character implicit in the model with which they have been simulated, in this case h=0.8. The resulting diffuse scatter is offset with respect to the specular peak and on rotation of the sample about its surface normal, the diffuse peak precesses sinusoidally about the specular position whilst remaining unchanged in shape. It is modelled by the GIXS code for a terraced interface [17], where it is noted that the specular peak and the Yoneda wings remain fixed as the azimuthal angle is varied, while the diffuse peak moves sinusoidally. It is noted in both figures 5.9 and 5.10 that the peak in the diffuse scatter is not observed for small scattering angles. This suggests that the correlation length of the top surface is significantly shorter than that of the substrate-film interface and this conclusion is supported by the detailed simulations of the diffuse scatter. Furthermore it suggests that the terracing is confined to the lower interface and that there is little conformality between roughness on the top and bottom interfaces. Such assumptions are entirely consistent with the proposed model of a terraced substrate surface.

Where no offset is observed in the diffuse scatter it is found that a single correlation length is sufficient to fit the experimental data. In addition it is found that the value of the correlation length needed is that of the top surface in the other two samples. Consequently, it is possible to say that there is a factor of three difference in the correlation lengths between the top and bottom surface of the sample when step-bunching has occurred.

Thus the interpretation of the diffuse scatter fits extremely well with the established model for step-bunched Si and the sample preparation methods used were consistent with inducing such an effect.

Since there is great interest, in many areas, in using step-bunched Si substrates as a means of controlling the bulk properties of samples deposited on them, the methods employed here prove it is possible to extract information about the nature of the terracing on the substrates, non-destructively, even after deposition.

References for Chapter 5

[1] A. V. Latyshev, A. L. Aseev, A. B. Krasilnikov and S. I. Stenin Surface Science **213** *157* (1989)

[2] N. C. Bartelt, E. D. Williams, R. J. Phaneuf, Y. Yang and S. Das Sarma J. Vac. Sci. Technol. A **7** (3) *1898* (1989)

[3] E. D. Williams and N. C. Bartelt Ultramicroscopy **31** *36* (1989)

[4] L. Howald, R. Lüthi, E. Meyer and H. -J. Güntherodt Phys. Rev. B **51** (8) *5484* (1995)

[5] Y. Wang and T. T. Tsong Phys. Rev. B **53** (11) *6915* (1996)

[6] D. Y. Noh, K. I. Blum, M. J. Ramstad and R. J. Birgeneau Phys. Rev. B **48** (3) *1612* (1993)

[7] Y. H. Phang, C. Teichert, M. G. Lagally, L. J. Peticolos, J. C. Bean and E. Kasper Phys. Rev. B **50** (19) *14435* (1994)

[8] R. D. Aburano, H. Hong, J. M. Roesler, K. Chung, D. -S. Lin, P. Zschack, H. Chen and T. -C. Chiang Phys. Rev. B **52** (3) *1839* (1995)

[9] M. D. Upward, P. Moriarty, P. H. Beton, S. H. Baker, C. Binns and K. Edmonds Appl. Phys. Lett. **70** (16) *2114* (1997)

[10] A. W. Dunn, P. Moriarty, M. D. Upward and P. H. Beton Appl. Phys. Lett. **69** (4) *506* (1996)

[11] A. Encinas, F. Nguyen Van Dau, M. Sussiau, A. Schuhl and P. Galtier Appl. Phys. Lett. **71** (22) 1997

[12] F. Nguyen Van Dau, M. Sussiau, A. Schuhl and P. Galtier J. Appl. Phys. **81** (8) 1997

[13] D. A. Neumann, H. Zabel and H. Morkoc Appl. Phys. Lett. **43 (1)** 59 (1983)

[14] S. K. Sinha, M. K. Sanyal, S. K. Satija, C. F. Majkrzak, D. A. Neumann, H. Homma, S. Szpala, A. Gibaud and H. Morkoc Physica B **198** 72 (1994)

[15] I. Pape, T. P. A. Hase, B. K. Tanner, H. Laidler, C. Emmerson, T. Shen and B. J. Hickey J. Magn. Mag. Mater **156** 373 (1996)

[16] S. K. Sinha, E. B. Sirota, S. Garoff and H. B. Stanley Phys. Rev. B **38** *2297* (1988)

[17] I. Pape, T. P. A. Hase, B. K. Tanner and M. Wormington Physica B **253** *278* (1998)

[18] J. Grim, V. Holy, J. Kubena, J. Stangl, A. A. Darhuber, S. Zerlauth, F. Schäffler and G. Bauer J. Phys. D **32** *A216* (1999)

[19] V. Holy, C. Giannini, L. Tapfer, T. Marschner and W. Stolz Phys. Rev. B **55** (15) *9960* (1997)

[20] A. Gibaud, R. A. Cowley, D. F. McMorrow, R. C. C. Ward and M. R. Wells Phys. Rev. B **48** (19) *14463* (1993)

[21] A. Pimpinelli, J. Villain and D. E. Wolf J. Phys. I France **3** *447* (1993)

Chapter 6 - Grazing Incidence Scattering Studies of Spin-Valves

Grazing incidence x-ray scattering studies have been performed on a series of Si and SiO$_x$ substrates, and on equivalent spin-valves deposited onto these substrates. Detailed analysis of the x-ray data has been undertaken in order to characterise the roughness of the initial substrates and how this roughness propagates through the subsequently deposited spin-valve. These data are compared with both atomic force microscopy images taken of the samples and magnetoresistance measurements made on the spin-valves. The results discuss the crucial role that roughness, and roughness propagation, play in determining the magnetic properties of such systems.

6.1 Introduction

The use of spin-valves as sensitive magnetic sensors [1] has greatly increased over the last few years, some such devices now being available on the commercial market. In many areas, such as the integration of these sensors with silicon electronics, it is often necessary to incorporate these devices into existing manufacturing processes. The ability therefore, to produce good sensors on a variety of substrates that can withstand key manufacturing processes and survive intensive usage is clearly crucial for their commercial exploitation.

In this study three types of Si substrate are compared, as are the subsequent magnetic and structural properties of equivalent spin-valves deposited on them. Two different forms of silicon oxide (SiO$_x$) substrates were produced. One by the thermal oxidation of a Si (100) wafer and the other by depositing SiO$_x$ onto an identical Si wafer by low pressure chemical vapour deposition (LPCVD). An untreated piece of Si (100) wafer was used as a standard reference. Although both types of oxide substrate studied here

are commonly used for integrated circuit fabrication, the LPCVD oxide is more representative of the typical surface encountered.

Equivalent spin-valves were deposited onto these three types of substrate by sputtering at Leeds University, U.K. The spin-valves have been studied by x-ray scattering, atomic force microscopy (AFM) and magnetotransport measurements. Grazing incidence x-ray scattering measurements have also been made on the bare substrates. The results from this series of measurements have been analysed and are discussed, comparing the structural and magnetic properties of the samples. The implications of the findings are discussed with respect to growing such devices on commercially available substrates and their subsequent integration into the existing Si industry.

Prior to presenting the results of these experiments, a brief overview is given of the GMR effect and how it is used in spin-valves to produce sensitive magnetic sensors.

6.2 Giant Magnetoresistance in Layered Systems

6.2.1 Introduction

Aspects of the GMR effect in granular systems have already been discussed in chapter 4. In this chapter, the nature of the GMR effect is discussed initially in relation to layered systems, and then more specifically with regard to spin-valve structures.

The GMR effect describes the change observed in the resistance of certain materials when placed in an external magnetic field. Such an effect was first observed in magnetic multilayers, where magnetic layers are separated by non-magnetic spacer layers, by Binasch et al [2] studying Fe / Cr / Fe systems grown by Molecular Beam Epitaxy (MBE). Although the effect seen here was indeed enhanced magnetoresistance the changes observed could hardly be described as giant. The first really giant magnetoresistance was reported by Baibich et al [3] where a factor of 2 decrease in

resistivity was observed on the application of a 20kOe magnetic field at 4K in MBE grown Fe / Cr multilayers. Figure 6.1 shows the magnetoresistance of these Fe / Cr multilayers as measured by Baibich *et al* [3].
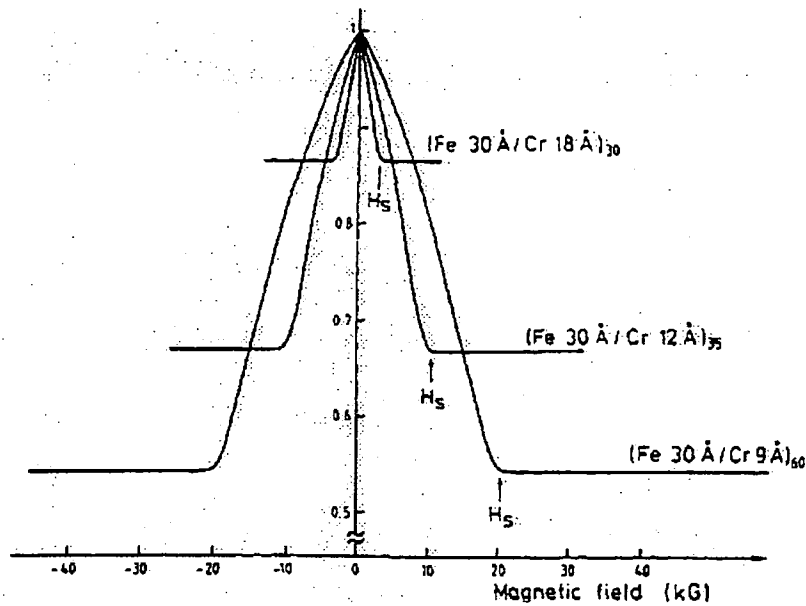

Figure 6.1 - Plot of normalised resistance versus applied magnetic field for three Fe / Cr multilayers measured at 4K (reproduced from Baibich *et al* [3])

Figure 6.1 clearly demonstrates the effect of GMR where it can be seen that a large change in the resistance is observed as a magnetic field is applied to the sample. This change in resistance defines the magnitude of the GMR which is usually given as a percentage as defined in equation (6.1)

$$\%GMR = 100 * \frac{(R_0 - R_{sat})}{R_{sat}} \qquad (6.1)$$

This percentage change can be very high with values greater than 100% having been reported at room temperature and values of around 65% being regularly obtained [4]. Large changes in resistance as a function of magnetic field offer a huge potential in many technological applications such as computer read heads, magnetic field sensors and automotive sensors in cars and consequently, much of the work done in this area has been driven by commercial applications.

6.2.2 Origins of GMR in Layered Systems

The GMR effect is typically observed when two magnetic layers are separated by a non-magnetic spacer. In magnetic multilayers this basic unit of magnetic / non-magnetic layer is usually repeated tens of times to give the full multilayered structure. In an ideal GMR material the magnetisations of the alternate magnetic layers are arranged to be anti-parallel in zero field i.e. they are arranged antiferromagnetically.

In much of the early work on magnetic multilayer systems only ferromagnetic (F) coupling was observed between the magnetic layers. Classically, two ferromagnetic bodies, separated by some distance, would align antiparallel to each other in order to minimise the magnetostatic energy between them. As these bodies are brought into contact they become able to share conduction electrons and align in a parallel orientation. In the 1960's it was shown that such an interaction was not limited to magnetic bodies in contact, and that ferromagnetic films separated by metallic spacers upto a few hundred Å thick would still align ferromagnetically [5]. The first experimental evidence for anomalous (antiferromagnetic (AF) as opposed to F) coupling between the layers came in 1986 with an experiment by Grunberg *et al* on a series of Fe / Cr trilayers [6]. They observed that for a certain thickness of the non-magnetic Cr spacer layer, the magnetic Fe films would exhibit AF coupling. In 1990 Parkin *et al* [7] went on to show that such AF coupling occurred for more than one value of spacer layer thickness and that the type of coupling between the magnetic layers oscillated between F and AF as a function of spacer layer thickness. In addition, Parkin showed that such an effect was not confined to Fe / Cr multilayers but that it was a general trend for transition metal spacers [8], Co / Cu becoming one of the most widely studied systems. For example, the first AF coupling peak in a typical Co / Cu multilayer occurs for a Cu spacer layer thickness of 10Å [9].

Attempts to explain this phenomena of oscillatory indirect coupling began with use of the Ruderman-Kittel-Kasuya-Yosida (RKKY) interaction [10-12]. This interaction describes the effect of placing a point magnetic impurity in an non-magnetic matrix. The conduction electrons of the host matrix rearrange around the impurity in order to screen it out. In doing so the charge density of the rearranged host electrons does not fall off

uniformly but oscillates as a function of distance. If the imbedded impurity is then assumed to have a magnetic moment, an exchange interaction occurs between the unpaired and itinerant electrons, and the spin of the itinerant electrons can align either parallel or antiparallel to that on the magnetic impurity. Consequently, oscillations occur in the spin density which results in either a F or AF interaction between the magnetic impurities, dependent on their separation.

A similar result can be predicted for separated magnetic layers where the interactions between all the atoms on the surface of the two magnetic layers are summed. However if this is calculated, the range of the interaction obtained is of the order of 2Å, far shorter than the 10Å thickness of the spacer layer needed to observe AF coupling experimentally. This apparent discrepancy was resolved by the introduction of an 'aliasing' term into the theory [13] where interactions are only considered at the lattice points of the magnetic layers. This results in a larger interaction range being predicted which agrees excellently with previous experimental observations. More complex theories relating to quantum confinement have also been developed to explain this phenomena [14], but detailed descriptions of these are beyond the scope of this introductory section.

6.2.3 Scattering Processes Involved in GMR

The scattering of electrons by local lattice distortions, or impurities, as they pass through a material is the origin of electrical resistance. The spin dependent nature of this scattering in magnetic materials is the cause of the GMR effect. Current carrying electrons within a metallic material originate from the delocalised s-p hybridised conduction bands. For the electrons to move through a material without being scattered there have to be empty states available into which they can be scattered. Since this only depends on states which are close to the Fermi level this means, for transition metals, we need only consider the 3d bands since all other bands fall well below the Fermi level and are consequently full and play no part in the conduction process.

The spin of an electron is defined as either up or down depending on whether it is aligned parallel or anti-parallel to the magnetisation vector within the magnetic layer. Spin up electrons are more energetically stable meaning the spin up band lies at the lower energy, typically below the Fermi energy, there being no free states into which the electrons can move. Part of the spin down band, however, lies above the Fermi level leaving free states into which spin down electrons can scatter and they are consequently scattered more than those in the spin up state. Both states will be scattered equally in the non magnetic spacer layer as both bands lie below the Fermi level and are consequently not dependent on the spin of the electron.

The reason such a scattering process leads to GMR lies in the difference between the density of states for F and AF coupled systems as shown schematically in figure 6.2.

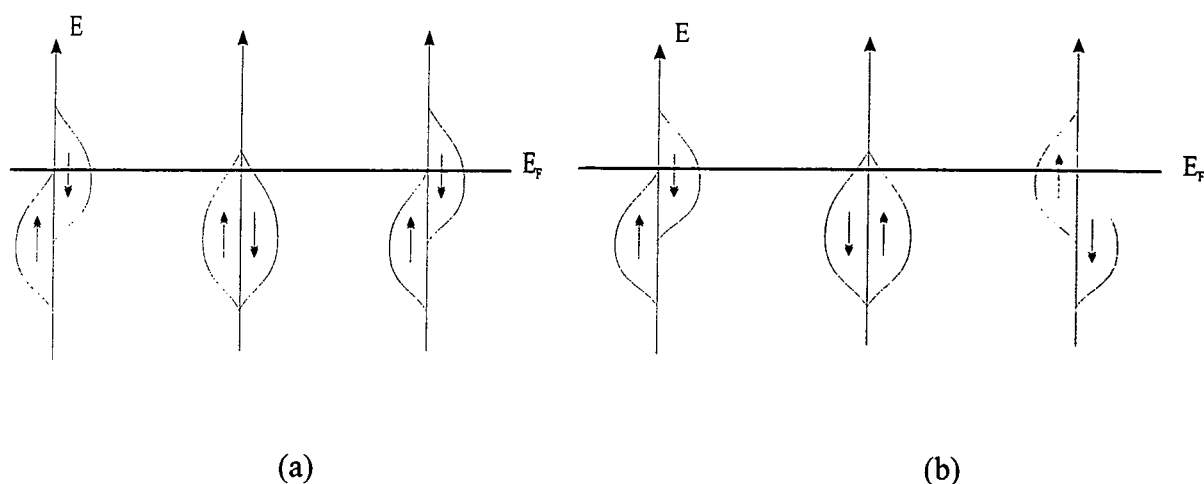(a)   (b)

Figure 6.2 - Schematic of the density of states for the 3d bands for a F (a) and AF (b) coupled spin-valve system. The layers represented in this schematic are, left to right, the first magnetic layer, the non-magnetic spacer and the second magnetic layer.

For a F aligned system, spin down electrons will be scattered in both magnetic layers, whereas the spin up electrons will pass through both layers with minimal scattering. In the case of AF alignment, the density of states in the two magnetic layers will be different, due to the nature of the coupling. In this case the spin down electrons will be scattered in one magnetic layer, and the spin up electrons in the other. This is illustrated in figure 6.3.
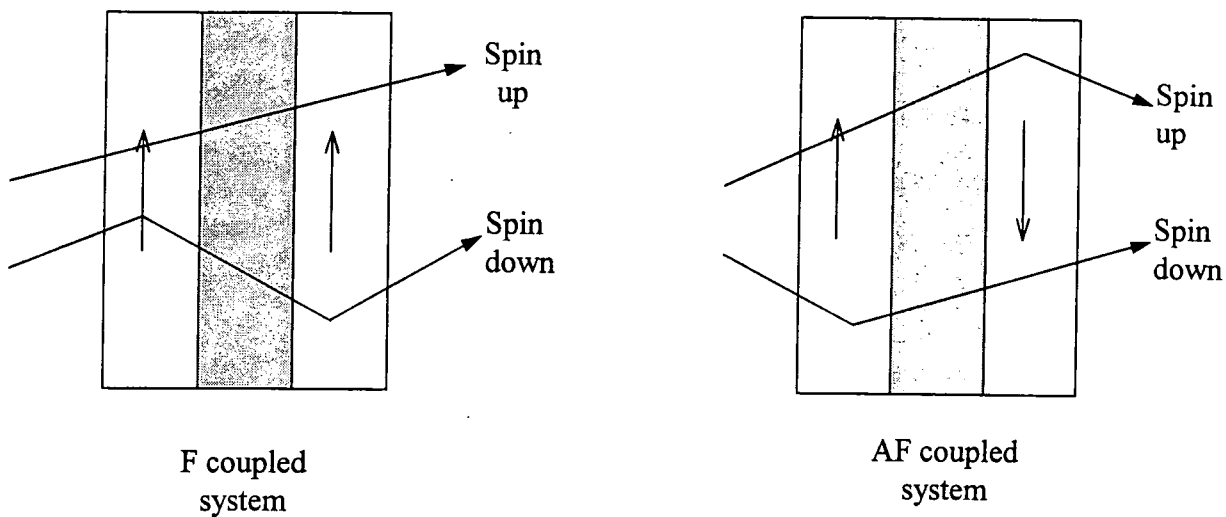
F coupled
system

AF coupled
system

Figure 6.3 - schematic of the scattering process in a F and AF coupled system

If these scattering processes are considered using a simple resistor model, it is clear to see that the scattering in the AF coupled system leads to a higher overall resistive state than the F coupled system. Consequently the ability to switch between these two states allows a large change in the resistance to be realised. For a more detailed review of scattering in GMR materials the reader is refereed to an excellent article by Nesbet [15].

As already discussed, the initial state of a typical GMR material is such that all the layers exhibit AF coupling. On application of a magnetic field the spins opposing the applied field gradually rotate to align with the field and the resistance falls reaching a saturation point when all the layers are aligned ferromagnetically, figure 6.1. If the field is then taken back to zero the spins realign in an AF configuration due to the AF coupling between the layers and the higher resistive state is recovered.

Although very high GMR ratios are achievable using such multilayered structures their sensitivity is small due to the large saturation field involved in aligning the spins ferromagnetically. This large field is due to the strong coupling between the layers. If the layers can be decoupled this coupling strength will decrease and hence the field needed to switch will be reduced and a more sensitive system will have been created. A very commercially important type of system which relies on this principle is that of a spin-valve [16].

6.3 Spin-valves and the GMR Effect

In contrast to the magnetic multilayers discussed previously, a spin-valve has only a 'GMR trilayer' forming the active part of the system. This trilayer, which can be grown in different orientations within the spin-valve, consists of two ferromagnetic layers separated by a non-magnetic spacer layer where, in contrast to magnetic multilayers, the two ferromagnetic layers are ideally not coupled. The mechanism of GMR relies on the ability to achieve both a F and AF state within the system. In the case of a spin-valve this is achieved by pinning one of the magnetic layers within the system with an antiferromagnetic layer. The other ferromagnetic layer in the trilayer is not pinned and is, therefore, free to move in small external fields. This allows the alignment of the spin-valve to be readily changed from AF to F by the application of small fields and consequently a large change in the resistance will be realised. Although the GMR is reduced by having fewer magnetic layers than in a multilayer system (typical GMR values being 4-6% [17]) the sensitivity can be many orders of magnitude higher and as such these systems have a much greater potential in commercial applications.

Figure 6.4 shows a schematic diagram of a typical spin-valve system equivalent to those studied in this chapter. A spin-valve grown in this configuration is known as a top spin-valve as the pinned layer is at the top of the stack. Bottom spin-valves, where the pinning layer is at the bottom, are also used, although they are harder to fabricate since the free NiFe layer is grown on top of a magnetically saturated film. Symmetric spin-valves can also be grown where the free magnetic layer sits between two pinned layers.
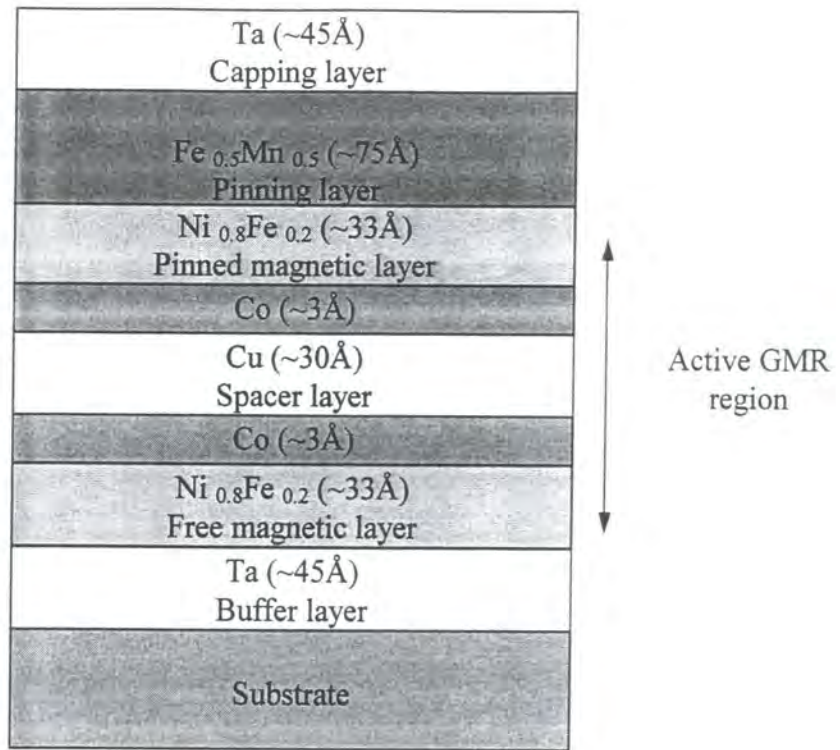
Figure 6.4 - Schematic of a typical spin-valve. Nominal thickness values and materials shown are those used in this study

The materials used in such spin-valves are chosen both for their magnetic properties and for the ease of deposition in the sputtering system. Co is inserted between the spacer and magnetic layers for a dual purpose. Since Cu and NiFe are miscible the Co acts as a diffusion barrier between these layers maintaining a good interface structure. The insertion of Co at the interfaces also leads to a higher GMR ratio [18] .

A Ta buffer is used to induce (111) orientated growth within the stack. This is crucial for the production of the correct form of strongly antiferromagnetic FeMn.

Using this model of a spin-valve it is now possible to consider what happens on the application of an external magnetic field to the system shown in figure 6.4. In zero applied field the thickness of the non magnetic spacer layer is arranged such that the magnetic layers will align ferromagnetically. On the application of a very small field, the coercive field, H_c of the free layer, the moment of the free layer will flip to align with the external field and a high resistance, antiparallel state will be achieved. It is important to note at this stage that an external field applied in the opposite direction will have no effect on the resistance of the sample. Unlike magnetic multilayers this means

that spin-valves are sensitive not only to the magnitude of the applied magnetic field but also to its direction. This high resistance state is stable until the applied field approaches the exchange field exerted on the pinned layer from the AF coupling in the pinning layer. Beyond this, the pinned layer is forced to follow the applied field and the parallel alignment and hence low resistance state is recovered. Such a response to magnetic field is demonstrated in figure 6.5 where a typical magnetisation loop is shown for a spin-valve [19].
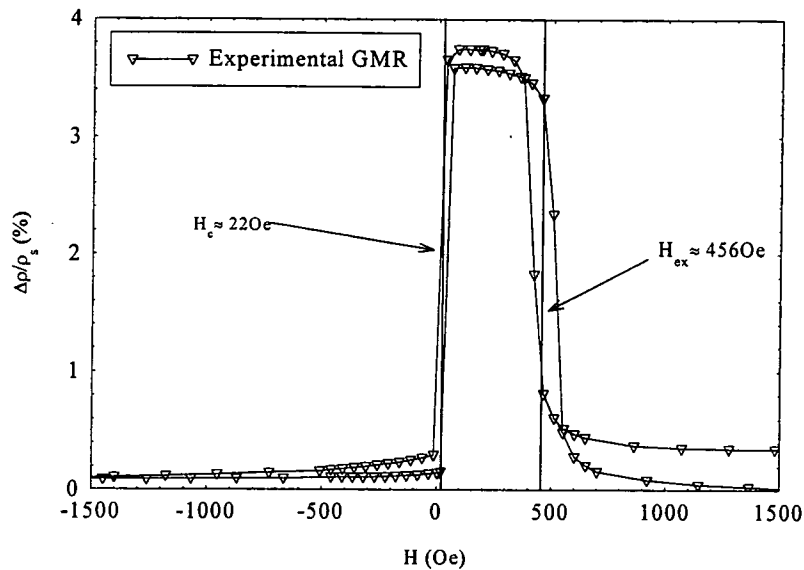

Figure 6.5 - Magnetisation loops for a typical spin-valve system. The coercive field, H_c, and the exchange field, H_{ex} indicated with vertical lines.

The coercive and exchange field are the two key properties, along with the magnitude of the GMR, which must be considered when producing a spin-valve for commercial applications. The coercive field determines the minimum field the device can detect, while the exchange field of the pinned layer is ideally kept as high as possible to ensure the two resistance states are well separated. An exemplary spin-valve will have a minimum of interlayer coupling resulting in a switching point close to zero applied field. The sensitivity of a sensor is increased by a high GMR ratio but can be lost when measures are taken to reduce coupling [20]. A balance between such conflicting properties has to be found in order to create a workable device.

6.4 Experimental Results

6.4.1 Sample preparation

The two types of commercially important substrates which have been investigated in this study were prepared at the Defence Evaluation and Research Agency (DERA) in Malvern, U.K. In growing these substrates it was intended that the typical processing conditions found within the integrated Si industry could be emulated.

The first substrate was produced by baking a (100) Si wafer at 800°C for about 50 minutes in an oxygen / hydrogen mix. The second substrate was prepared using low pressure chemical vapour deposition (LPCVD). Two layers of low temperature SiO_x, a nominally 6500Å undoped layer followed by a 2500Å phosphorous doped layer, were deposited onto a (100) silicon wafer. This form of deposition is representative of that used in a typical 2μm CMOS process within the Si industry. Deposition was followed by a 1050°C anneal in a mixed oxygen / hydrogen atmosphere to reflow the doped layer allowing some smoothing of the deposited surface.

Equivalent spin-valves of the form shown in figure 6.4 were deposited onto these substrates by DC magnetron sputtering in a custom built vacuum system at the University of Leeds, U.K [21]. The system is equipped with six sputtering targets with a base pressure of 2×10^{-8} Torr. At base pressure 90% of the residual gas appears at mass 28 on the RGA which means it is either CO or N_2. A working gas pressure of 5.0mTorr of Ar was used, and deposition rates were typically 3.0Å/s. The substrates investigated were rinsed in organic solvents before being introduced to the vacuum chamber. More aggressive cleaning processes were avoided to leave the substrate oxide layers intact. During growth, the samples were subjected to an external field of 200 Oe which defined the direction of the pinned layer.

In addition to the oxide substrates an equivalent spin-valve was deposited onto an untreated Si (100) wafer so that this and the untreated wafer could be used as control

samples. Samples of both the bare substrates and the spin-valves deposited onto them were studied initially by atomic force microscopy prior to magnetic and x-ray measurements.

6.4.2 Presentation and Comparison of X-Ray and AFM Data

A series of grazing incidence x-ray scattering measurements were performed on the two-circle powder diffractometer at BM16 of the ESRF in Grenoble, the high brilliance of this source allowing excellent quality data to be collected from these systems. A typical reflectivity set-up was used in all the experiments, as described in chapter 3.

Full reflectivity profiles were taken for each sample, the combination of specular and off-specular scans allowing the true specular scatter from the samples to be obtained and modelled, quantifying the roughness and thickness of the layers. Transverse diffuse scans were also taken for the samples in order to further study the nature of the roughness within these systems.

Figure 6.6 shows a comparison of the specular and off-specular scatter from both types of SiO_x substrate and also from the pure reference Si wafer.
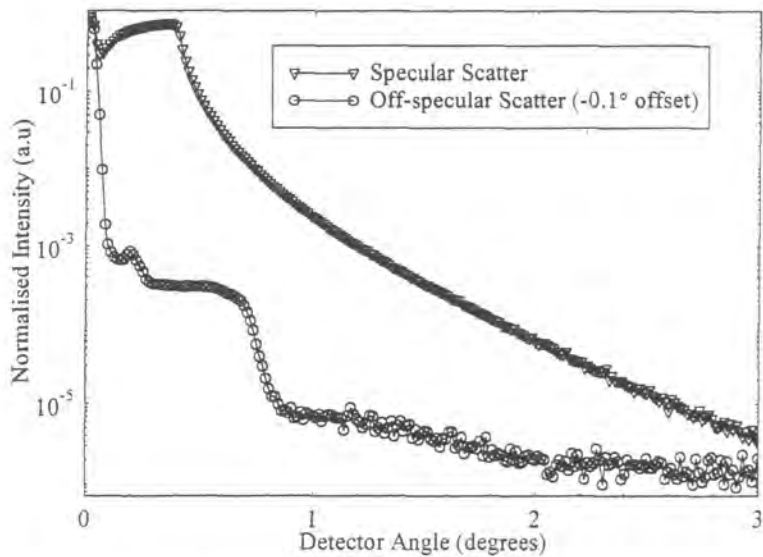

Figure 6.6a - Specular and off-specular scatter from the reference Si wafer taken at a wavelength of 1.392Å

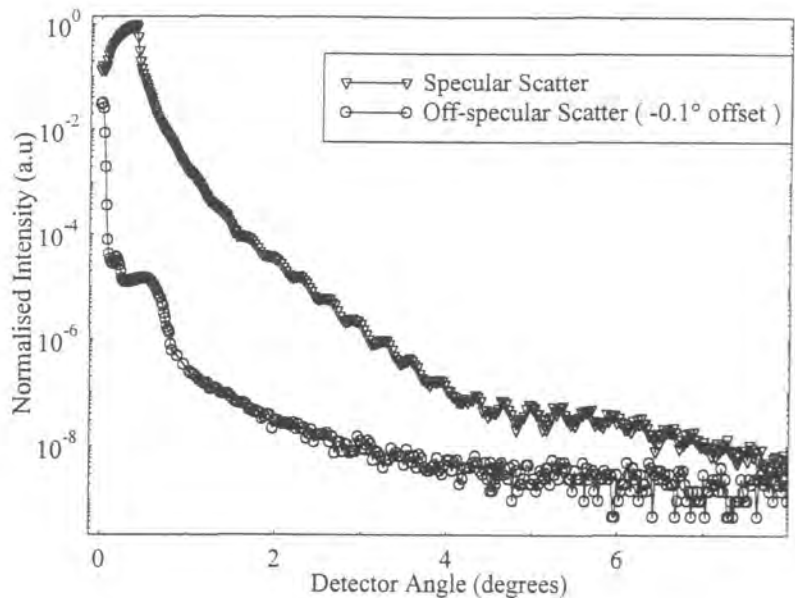Figure 6.6b - Specular and off-specular scatter from the thermally oxidised Si substrate taken at a wavelength of 1.381Å
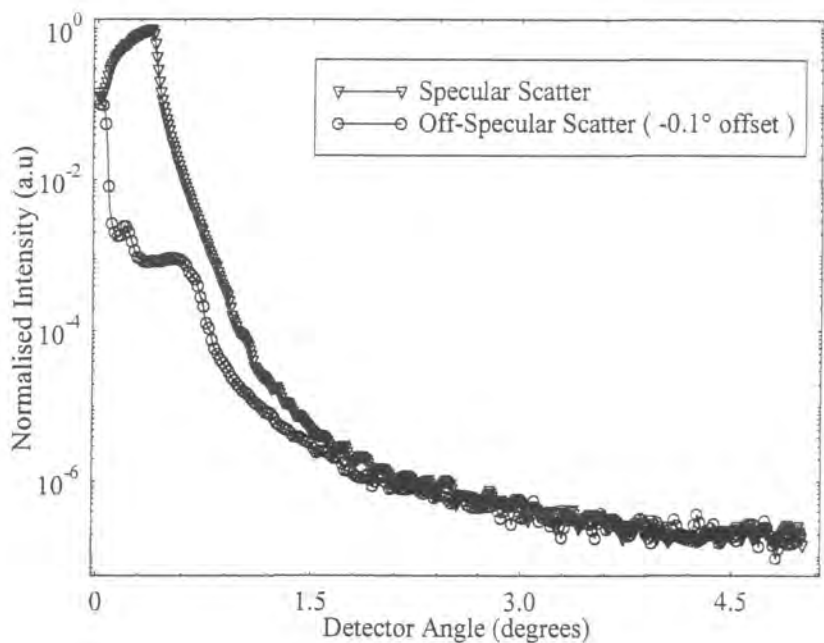

Figure 6.6c - Specular and off-specular scatter from the LPCVD Si substrate taken at a wavelength of 1.381Å

From the higher rate of fall of the specular intensity, in figures 6.6b and 6.6c, it is immediately apparent that the LPCVD oxide is considerably rougher than the thermally

oxidised substrate, both of the SiO_x substrates being rougher than the reference, untreated Si wafer. Simulations of the true specular scatter, obtained using the Bede REFS code, close to the critical angle are shown in figure 6.7. Excellent agreement in the fall-off of intensity between the experimental and simulated data results in precise values for the effective surface roughness (actually mean interface width - see chapter 2) being obtained from the simulation.

The best fit gave a surface r.m.s. roughness of 9 ± 1Å for the thermally oxidised substrate whilst the LPCVD oxide was found to be considerably rougher, with a r.m.s surface roughness of 25 ± 2Å. The r.m.s surface roughness of the reference Si wafer was found to be 5 ± 0.5Å. In each case, the roughness of the Si / SiO_x interface was 2 ± 0.5Å.
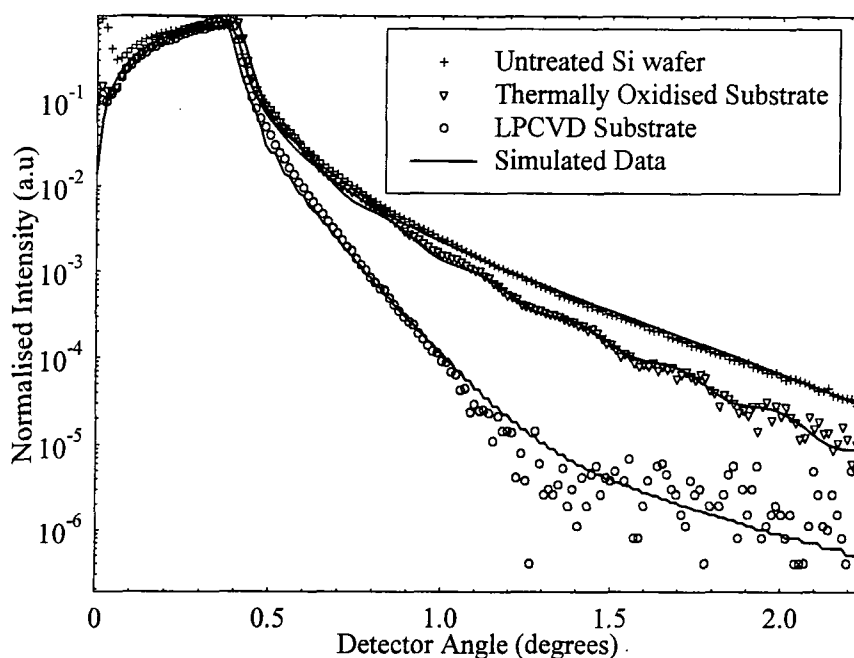
Figure 6.7 - Simulations of the true specular scatter for the three bare substrates shown close to the critical angle

The thickness of the SiO_x layer present on the thermally oxidised substrate was also determined from these simulations by accurately matching the period of the Kiessig fringes in the true specular scatter. The density of the layer was obtained from accurately matching the position of the critical angle, θ_c. A 245 ± 4Å layer of SiO_x was determined with a density of 2.253g/cm³ compared to the bulk value for SiO_2 of 2.65g/cm³. The discrepancy in the densities suggests that pure SiO_2 is not being observed, but that non-

stoichiometric SiO_x is present within the layer. In the case of the LPCVD oxide, Kiessig fringes were observed above a detector angle of 1.5°. The period of these fringes indicate the presence of a 575 ± 5Å buried SiO_x layer of slightly reduced density within the sample. The exact nature of this buried layer is difficult to ascertain from simulations due to the poor scattering contrast between the layers. Simulations show that no Kiessig fringes would be expected for the nominally deposited thickness of 9000Å.

Transverse diffuse scans taken at identical scattering vectors for the two oxide samples are shown in figure 6.8. It is clear to see that the level of the diffuse intensity from the LPCVD substrate is considerably greater than from the thermally oxidised sample while the specular is considerably lower in intensity. Since the level of the diffuse scatter is only related to *true* roughness on the surface of the samples, these measurements provide further, qualitative confirmation that the LPCVD is considerably rougher than the thermally oxidised substrate.
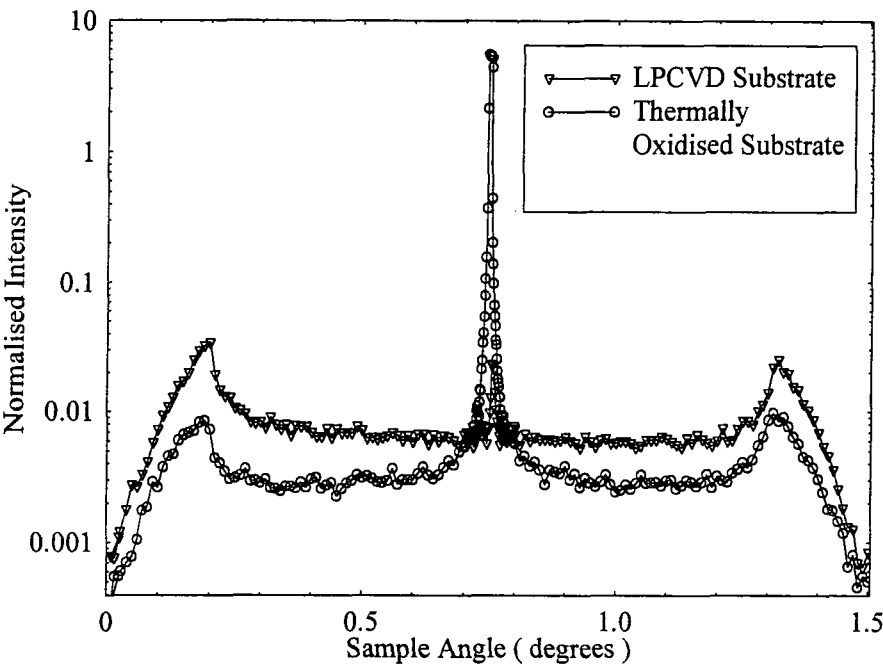

Figure 6.8 - Transverse diffuse scans taken at an identical detector position of 1.5° for the two SiO_x substrates. Wavelength used was 1.381Å.

All these measurements are in excellent agreement with atomic force microscope (AFM) images taken of the samples using a Digital Instruments Nanoscope. The

multimode scanning probe microscope, used in tapping mode, has a maximum range of ~15μm and a sample dependent resolution of <1nm. Images taken of the two treated substrates are shown in figure 6.9.
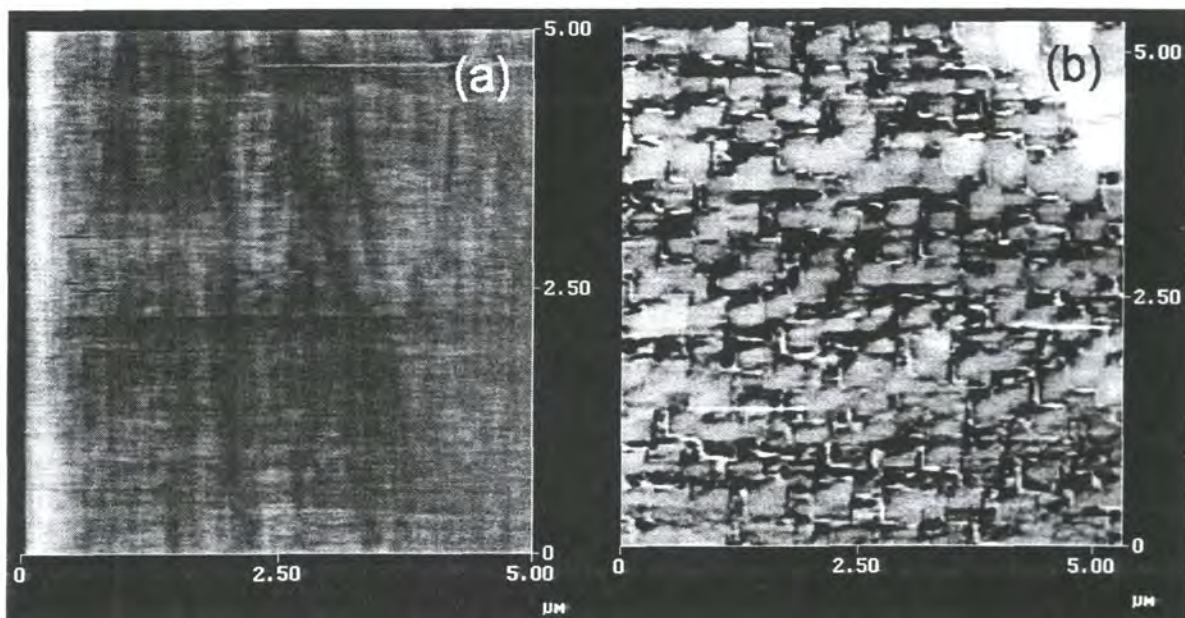
Figure 6.9 - AFM images of the thermally oxidised (a) and LPCVD (b) substrates. Colour contrast from black to white represents 25nm.

The LPCVD substrate appears considerably rougher than the thermally oxidised surface, the surface having a tiled appearance where the tiles have a width of 0.5μm and a height of ~20Å. In contrast the thermally oxidised substrate appears to have a uniformly smooth surface over the area shown.

Figure 6.10 shows the specular and off-specular scatter recorded from the nominally identical spin-valves grown on the three types of substrate. All these scans were taken at a wavelength of 1.48Å.

Figure 6.10a - Specular and off-specular scatter from the spin-valve grown on the untreated Si substrate taken at a wavelength of 1.48Å

Figure 6.10b - Specular and off-specular scatter from the spin-valve grown on the thermally oxidised Si substrate taken at a wavelength of 1.48Å

Figure 6.10c - Specular and off-specular scatter from the spin-valve grown on the LPCVD Si substrate taken at a wavelength of 1.48Å
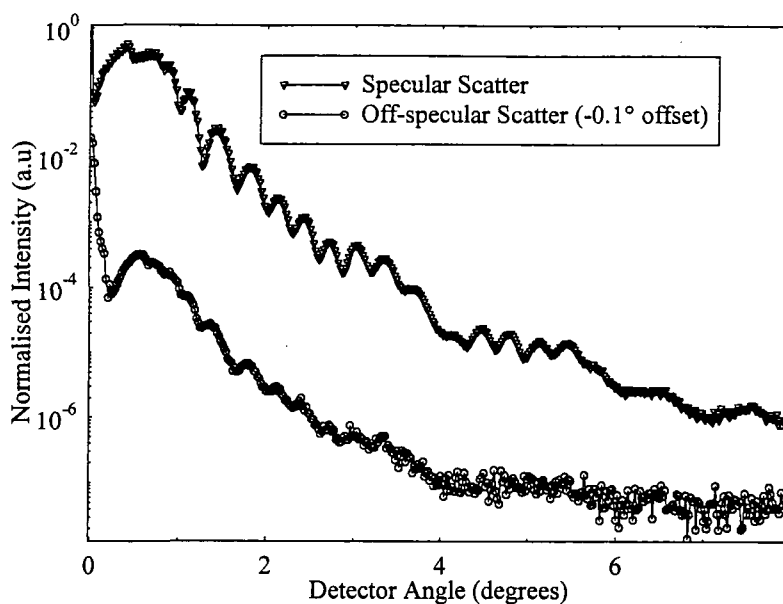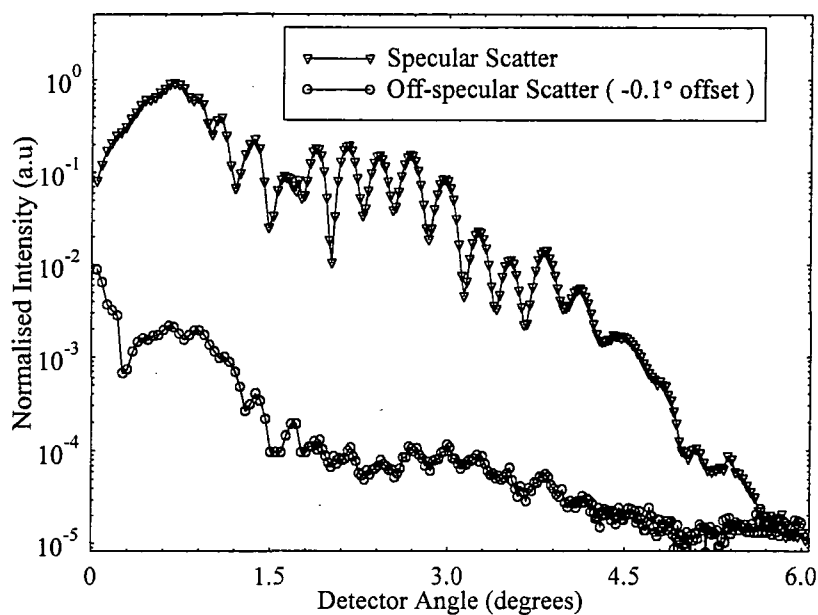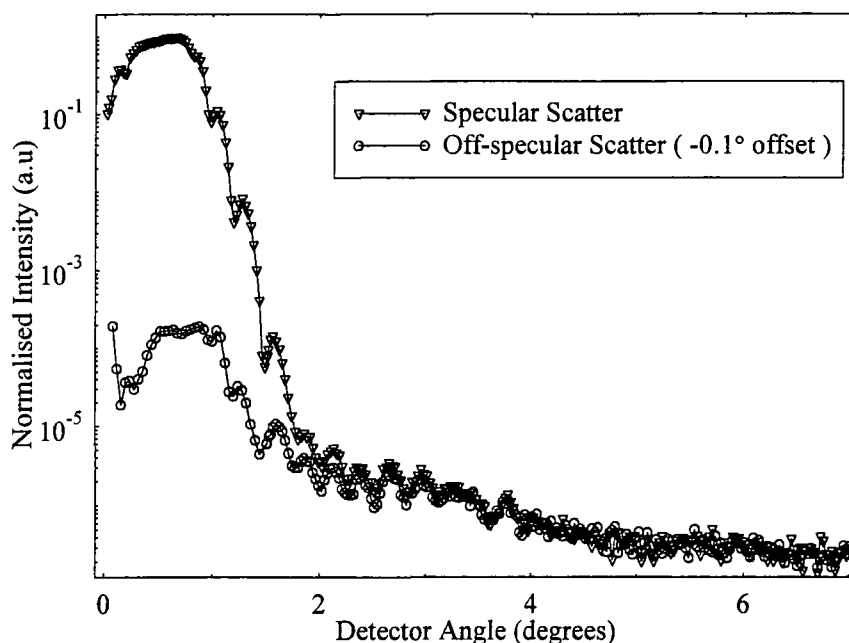
As in the case of the bare substrates it is immediately apparent that the spin-valve grown on the deposited oxide is considerably rougher than that grown on either the thermally oxidised or untreated substrate since the specular scatter is seen to drop off less rapidly in the latter cases. For the spin-valve grown on the LPCVD substrate the true specular scatter has crashed almost to zero by $2\theta=2°$.

For all spin-valve samples prominent Kiessig fringes are present in the off-specular scatter. The period of these fringes corresponds to the total stack thickness and indicates that all systems have a remarkably strong out-of-plane correlation in the roughness between the substrate and top surface [22].The reasons behind this have already been discussed and the reader is referred to chapter 2.5.2.

Ideally it would be possible to model the spin-valve structure and determine the roughness at each of the interfaces confirming, quantitatively, the nature of the roughness through the stack. Unfortunately for the case of spin-valves this is not possible using x-ray scattering alone. It is found that since all the transition metals within the stack are so close together in the Periodic Table, and consequently in scattering power, it is impossible to distinguish between the individual layers. In figure

6.11 the specular scatter from a spin-valve identical to those used in this study has been simulated. For the 'real' spin-valve all the individual layers are defined throughout the stack whereas in the 'pseudo' spin-valve all the layers between the Ta buffers are replaced by a single $Fe_{0.5}Mn_{0.5}$ layer, made to be as thick as the total of the constituent layers it is replacing.
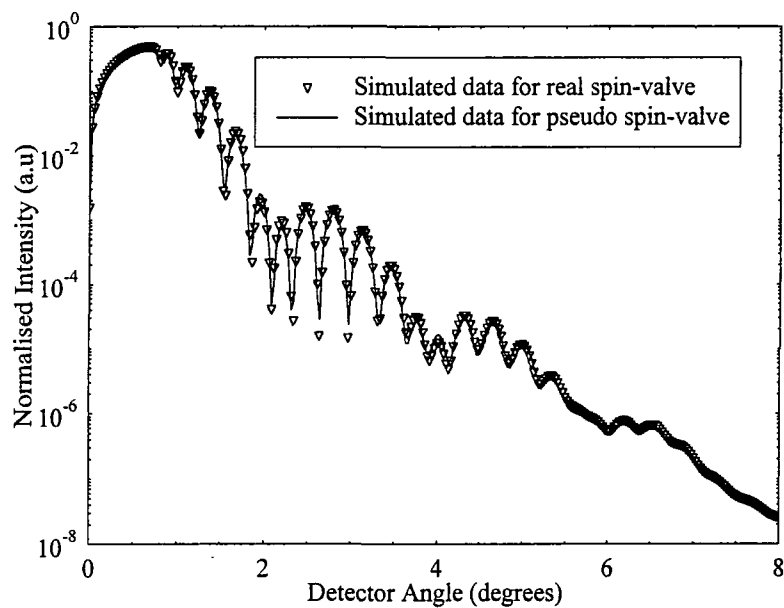
Figure 6.11 - Comparison of the simulated specular scatter form a real and pseudo spin-valve

It is apparent that little, if any, difference is observable between the two sets of simulated data and as such it is very difficult to ascertain, with any certainty, the properties of individual layers within the spin-valve stack. It has been shown elsewhere [23,24] that one possible method to overcome this problem is to combine GIXR with grazing incidence x-ray fluorescence. The fluorescence signals from the individual layers are clearly distinguishable, and it is possible to quantify the amounts of each material present within the stack.

Due to this problem of simulation, the true specular scatter was modelled as a pseudo spin-valve. Figure 6.12 shows the experimental and simulated true specular scatter from the spin-valve grown on the untreated Si wafer, modelled using the Bede REFS code.
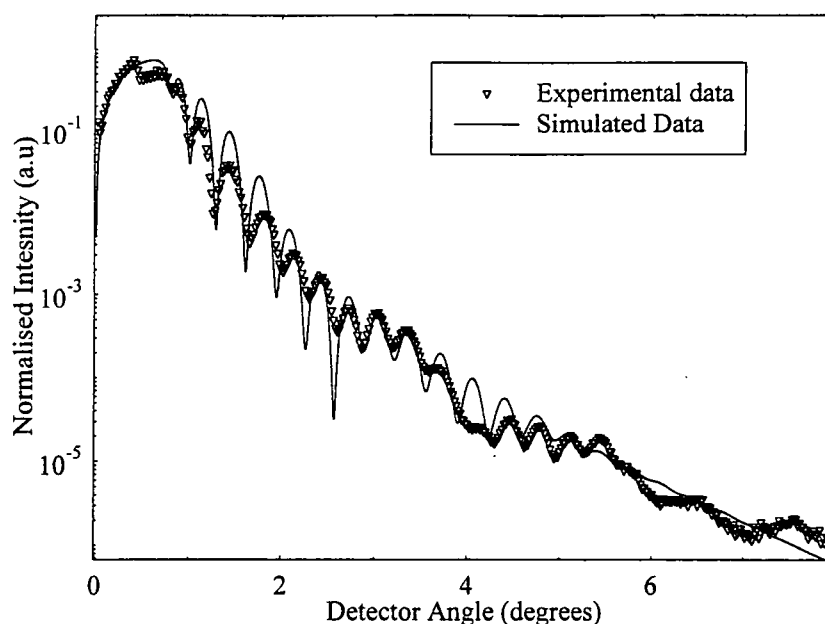
Figure 6.12 - Experimental and simulated true specular scatter from the spin-valve deposited on the untreated wafer at λ=1.48Å

Simulations show that the roughness of the substrate / buffer interface, for all three sample, is comparable to that of the surface of the spin-valve and of a value similar to that obtained for the bare substrate. For the simulation shown in figure 6.12 the following model was used.

Layer	Thickness(Å)	r.m.s Roughness (Å)
SiO_2	-	3 ± 0.5
Ta	41.3 ± 2	6 ± 2
$Fe_{0.5}Mn_{0.5}$	173 ± 5	6.5 ± 2
Ta	30 ± 2	6.5 ± 1.5

These measurements confirm the qualitative interpretation of the off-specular scatter, namely that a large degree of vertical conformal roughness is present within these systems. Further indication of conformality of the roughness comes from comparing the AFM images of the bare substrates with those of the surface of the deposited spin-valves (figure 6.13).
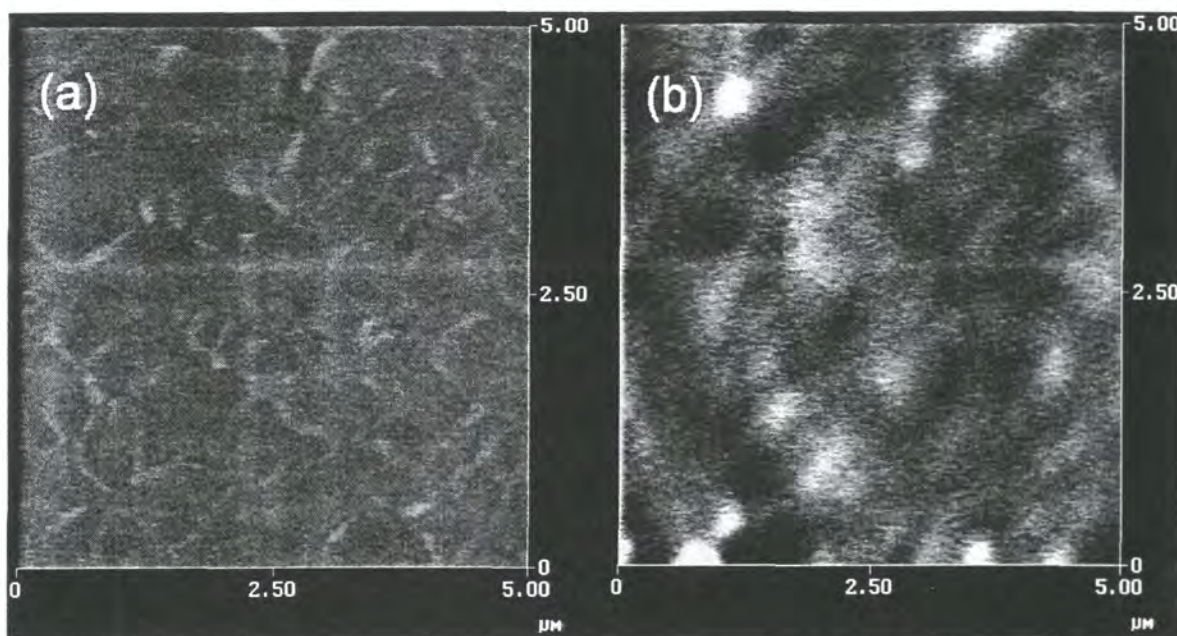
Figure 6.13 - AFM images of the surface of the spin-valves deposited on the thermally oxidised Si substrate (a) and the LPCVD Si substrates (b). Colour contrast from black to white represents 25nm.

With the spin-valves deposited on the two types of SiO_x substrate it is seen from the resulting AFM image that a much rougher surface develops for the LPCVD substrate when compared with the thermally oxidised substrate. This suggests that the 20Å step edges observed in the bare substrates are indeed still having an effect on the roughness after 270Å of sample has been deposited, which is entirely consistent with the x-ray data.

6.5 Discussion of Experimental Results and Comparison with Magnetic Data

When such strongly conformal roughness exists within a layered system it is expected that 'orange-peel' (or Neel) coupling exists. This type of coupling was first postulated by Neel in 1962 [25,26] and since then has received much attention [27-29]. A

schematic representation of the situation expected in such a highly out-of-plane correlated system is shown in figure 6.14.
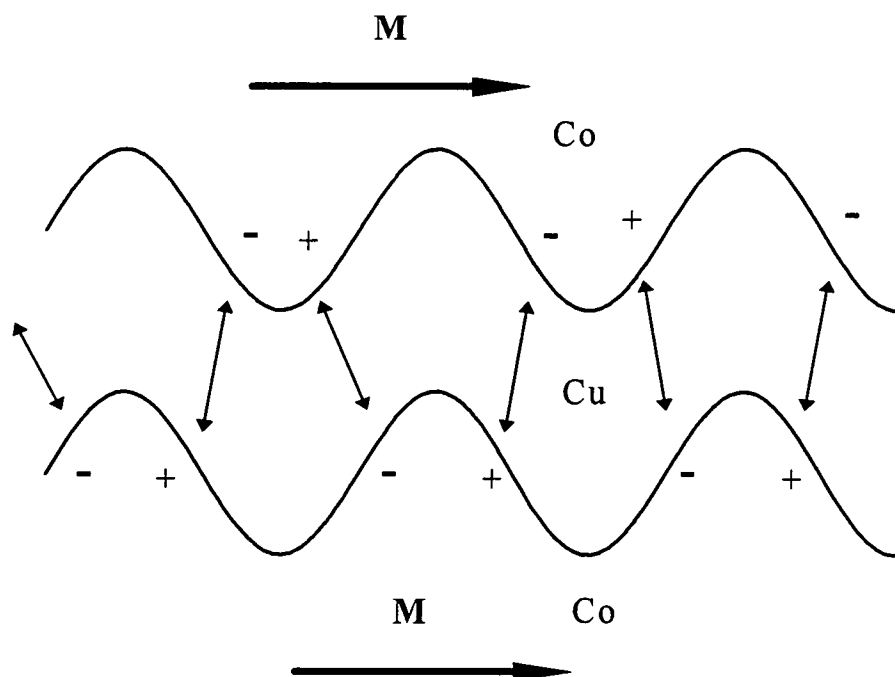
Figure 6.14 - Illustration of the effect of 'orange-peel' coupling

Two magnetic films are separated by a non-magnetic spacer as in the active part of a spin-valve. Assuming the magnetic moment of the layer lies in the plane of the film any 'bumps' in the layer will have magnetic poles on them creating dipole fields across the non-magnetic spacer (figure 6.14). When the roughness within the system is highly conformal out-of-the plane the dipole fields will interact to enhance the ferromagnetic coupling between the magnetic layers.

In the case of a spin-valve, where one of the layers is pinned, this increase in ferromagnetic coupling will act to shift the point at which the free layer switches from ferromagnetic to antiferromagnetic alignment (i.e. the coercive field) further away from zero applied field. The amount by which the coercive field will shift corresponds to the strength of this ferromagnetic coupling interaction, J, which is defined in equation (6.2) [25].

$$J = \frac{\pi^2}{\sqrt{2}} \frac{\sigma^2}{\lambda} (\mu_0 MM') \exp\left(\frac{-2\pi\sqrt{2}t_{NM}}{\lambda} \right) \qquad (6.2)$$

where t_{NM} is the thickness of the non-magnetic spacer and σ is the amplitude of the roughness, λ the wavelength of the roughness and M and M' are the magnetic moments in the two layers.

Consequently, if conformal roughness dominates a system, as has been shown is the case here, it would be expected that the rougher the substrate on which the spin-valve is grown the rougher the subsequently deposited layers and hence the higher the value for σ in the coupling equation. From the x-ray and AFM analysis of these systems it would be expected, therefore, that the spin-valve deposited on the rougher LPCVD substrate would experience the greater interlayer coupling.

Figure 6.15 shows GMR loops for the three spin-valves grown on the different substrates. These measurements were carried out at room temperature using a standard 4-probe DC technique [21] with the field applied in-the-plane of the layers, parallel to the bias direction of the pinned layer.
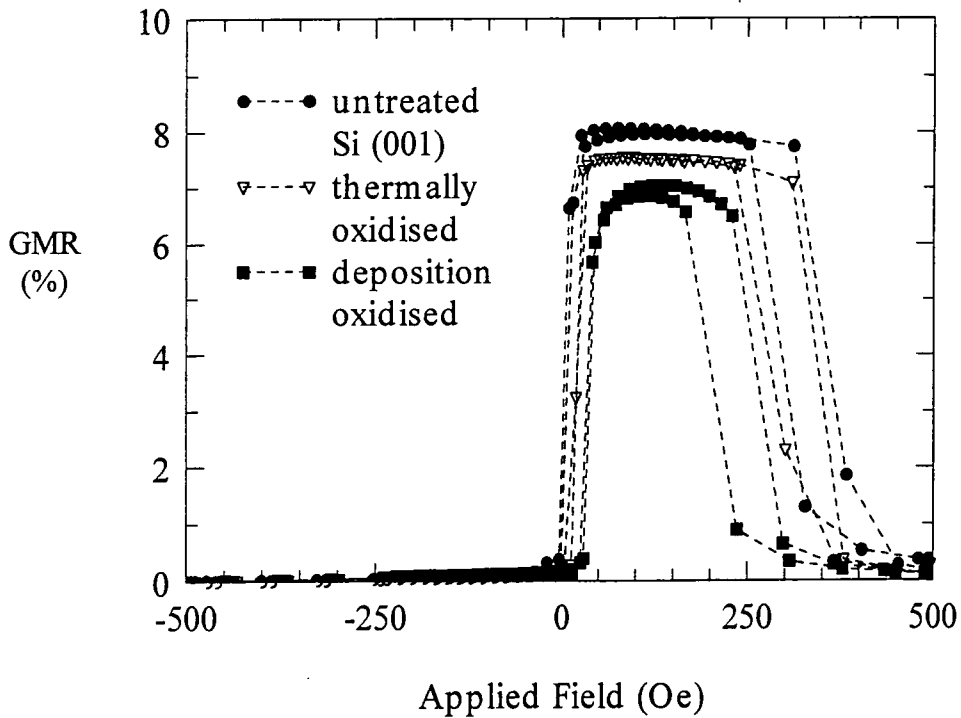

Figure 6.15 - GMR loops for the three nominally identical spin-valves deposited on different forms of Si substrate

For the untreated and very smooth Si substrate the coercive field of the free layer is seen to be very close to zero applied field. As the measured roughness of the substrates increases it is observed that the coercive field shifts away from zero by ~30Oe, a result which is in complete agreement with the proposed model of roughness present in these systems. In addition, a fall in the GMR is observed and the exchange field is seen to fall. All these changes combine to make the spin-valve grown on the LPCVD substrate a potentially much poorer magnetic sensor than either of the others.

A series of experiments have been undertaken at the University of Leeds [30] to attempt to minimise the observed shift in switching field. In one series of experiments Ta buffers of varying thickness were deposited onto the substrates, prior to the active part of the spin-valve, in an attempt to 'smooth out' inherent roughness on the substrate and hence reduce the coupling. This method had no appreciable effect on the movement of the switching field. In a second series of experiments, the thickness of the non-magnetic Cu spacer layer in the active spin-valve was varied. It was observed that for spin-valves grown on the rougher substrates, increasing the thickness of the Cu layer caused the coercive field to decrease.

These results are entirely consistent with the model of roughness proposed from analysis of the x-ray data from these samples. In such a strongly conformal system it would be expected that roughness would replicate through a buffer placed on the substrate and so the roughness at the interfaces in the active part of the spin-valve would be the same irrespective of whether or not a buffer was used. Additionally if the shift in the position of the switching point is indeed due to 'orange peel' type coupling then we can see from equation (6.2) that an increase in the thickness of the non-magnetic spacer layer would indeed lead to a reduction in the dipole interactions and consequently shift the position switching point back towards zero applied field.

6.6 Conclusions

In this chapter grazing incidence x-ray scattering studies have been used to demonstrate and quantify the large difference in roughness between two types of technologically

important SiO_x substrates and compare them with an untreated Si wafer. It has been shown that spin-valves deposited on such substrates, by the process of sputtering, possess a large degree of conformality in their out-of-plane roughness. AFM images of the samples confirm the interpretation of the x-ray data. This form of roughness leads to coupling between the magnetic layers, and hence a reduction in the sensitivity of these systems when used as magnetic sensors. The movement of the coercive field away from zero with increasing substrate roughness has been demonstrated with GMR measurements. The dominance of conformal roughness within these systems provides an explanation of the previously observed results that increasing the Cu spacer layer thickness serves to reduce the effect of coupling.

Since there is strong commercial interest in integrating GMR sensors into existing silicon microelectronics based on materials such as the LPCVD SiO_x described here, this result has important ramifications. It has been demonstrated that if an effective sensor is to be grown on such substrates additional measures must be taken to reduce the large degree of coupling which is present as a consequence of the conformal nature of the roughness, inherent in this deposition process.

References for Chapter 6

[1] J. C. S. Kools I.E.E.E **32** *3165* (1996)

[2] G. Binasch, P. Grunberg, F. Saurenbach and W. Zinn Phys. Rev. B **39** *4828* (1989)

[3] M. N. Baibich, J.M. Broto, A. Fert, F. Nguyen Van Dau, F. Petroff, P. Etienne, G. Creuzet, A. Friederich and J. Chazelas Phys. Rev. Lett. **61** *2472* (1988)

[4] C. H. Marrows, R. Loloee, B. J. Hickey J.M.M.M. 184 *137* (1998)

[5] J. C. Bruyere, G. Clerc, O. Massenet, D. Paccard, R. Montmory, L. Neel, J. Valin and A. Yelon IEEE Trans. Mag. **1** (3) *174* (1965)

[6] P. Grunberg, R. Schreiber, Y. Pang, M. B. Brodsky, H. Sowers Phys. Rev. Lett. **57** (19) *2442* (1986)

[7] S. S. P. Parkin, N. More, K. P. Roche Phys. Rev. Lett. **64** (19) *2304* (1990)

[8] S. S. P. Parkin Phys. Rev. Lett. **67** (25) *3598* (1991)

[9] M. A. Rudermann and C. Kittel Phys. Rev. **96** *99* (1954)

[10] T. Kasuya Prog. Theor. Phys. **16** *45* (1956)

[11] K. Yosida Phys. Rev. **106** *893* (1957)

[12] P. Bruno, C. Chappert Phys. Rev. B **46** (1) 261 (1992)

[13] J. Mathon, M. Villert, D. M. Edwards and R. B. Muniz J. Magn. Mag. Mat **121** *242* (1993)

[14] S. S. P. Parkin, R. Bhadra, K. P. Roche. Phys. Rev. Lett. **66** *2152* (1991)

[15] R. K. Nesbet IBM J. Res. Develop. **41** *53* (1998)

[16] B. Dieny J.M.M.M **136** *335* (1994)

[17] J. C. S. Kools I.E.E.E Trans. Mag. **32** (4) *3165* (1996)

[18] S. S. P. Parkin Appl. Phy. Lett. **60** *512* (1992)

[19] Courtesy of C. H. Marrow, University of Leeds

[20] W. F. Egelhoff et al J. Appl. Phys. **79** (1) *282* (1996)

[21] C. H. Marrows, PhD Thesis, University of Leeds (1997)

[22] D. E. Savage, J. Kleiner, N. Schimke, Y. -H. Phang, T. Jankowski, J. Jacobs, R. Kariotis and M.G. Legally, J. Appl. Phys. **69** (No. 3) *1411-1424* (1991)

[23] T. P. A. Hase, B. K. Tanner, P. Ryan, C. H. Marrows and B. J. Hickey, IEEE Trans. Magn. **34** (4 Pt1) 831 (1998)

[24] T. P. A. Hase PhD Thesis University of Durham (1999)

[25] L. Néel, Comptes Rendus Acad Sci **255** *1545* and *1676* (1962)

[26] A. Yelon, Physics of Thin Films (Academic Press, New York) **6** *205* (1971)

[27] T. G. S. M. Rijks, R. Coehoorn, J. T. F. Daemen and W. J. De Jonge J. Appl. Phys. **76** *1092* (1994)

[28] J. C. S. Kools, J.Appl. Phys. **77** *2993* (1995)

[29] R. D. K. Misra, T. Ha, Y. Kadmon, C. J. Powell, M. D. Stiles, R. D. McMichael and W. F. Egelhoff Jr. Mat. Res. Soc. Symp. **384** *373* (1995)

[30] F. E. Stanley, C. H. Marrows, E. W. Hill and B. J. Hickey   Sensors and Actuators A (in press)

Chapter 7 - <u>Grazing Incidence X-Ray Scattering Studies of</u> <u>Laterally Modulated Structures</u>

It has been observed that when a light emitting polymer is grown on a laterally modulated structure the photoluminescence from the sample is enhanced. The ability, therefore, to measure the propagation of roughness from this substrate through the deposited film, non-destructively, is crucial to the development of such systems. Grazing incidence x-ray scattering studies have been made on thin polymer films grown on laterally modulated substrates and also on a GaAs, etched grating. Both grating structures have a period of ~4000Å. A semi-kinematical theory has been developed to account for the coherent scatter from such structures and its ability to correctly predict the scatter from both types of grating studied is presented and discussed.

7.1 Introduction

In recent years, the use of laterally modulated structures in x-ray science has become more common, the monochromation of soft x-rays at many synchrotron sources [1-3] and focusing in x-ray telescopes [4,5] being two important examples.

More recently, the effect of lateral microstructures on light emitting polymers has been investigated. Conjugated polymers have, for a long time, been recognised as having huge potential in such devices as LED displays [6] and a large amount of research has gone into developing their photoluminescent properties. Unfortunately, a large proportion of the light generated in such devices is waveguided and lost, greatly reducing their efficiency [7]. Consequently, the control of waveguided modes in such light emitting materials has been become an important goal. A collaboration between the polymer groups of Durham and Exeter Universities has approached this problem by using laterally modulated substrates, onto which the polymers are deposited, to control the waveguided modes. A strong modification in the photoluminescence is observed from identical polymer films grown on laterally modulated substrates compared with

those deposited on planar ones [8]. These corrugated structures are designed to scatter the waveguided light into the forward viewing direction and so enhance the emission of the device. Since control of the lateral modulations is the key to enhancing the emission from such devices, it is useful to be able to study the form of the laterally modulated substrate and how this lateral modulation propagates through the deposited polymer to the surface of the sample. Grazing incidence x-ray scattering provides a non-destructive tool for determining both surface and sub-surface roughness of such devices and in determining the extent of both vertical and lateral correlations within the sample.

The first x-ray scattering experiments using gratings began in the late 1980's and early 1990's. Several groups observed, independently, modulations in the x-ray scatter in the vicinity of Bragg reflections from the sample. These modulations were found to be strongly influenced by the surface grating properties of the sample [9-15]. Some model calculations were presented alongside these observations but no real quantitative analysis of the data were presented.

The first real attempts at modelling the modulations in the scatter around these Bragg peaks were made by Tolan, Press, Brinkop and Kotthaus [16] whose calculations were based on the kinematical crystal truncation rod (CTR) theory [17-19]. This kinematical CTR theory had been shown elsewhere [20] to provide good quantitative agreement with experimental data, providing the area in the direct vicinity of the Bragg reflection itself was ignored, since here dynamical effects were no longer negligible. Fits of the experimental data by Tolan et al led to the determination of not only the mesoscopic grating parameters but also the roughness values of the grating surfaces.

Alongside these investigations, other groups were using the effects of grating structures to investigate the coherence properties of x-ray sources, an area which, with the development of third generation synchrotron sources, was beginning to attract a large amount of interest. Whilst Tolan at al [21] performed these experiments around the Bragg reflections from the samples, as had all the previous groups, Salditt et al [22] began to look at the x-ray scattering from such structures under the condition of grazing incidence. Unlike experiments taken around the Bragg reflections, those performed under the condition of grazing incidence are not sensitive to the crystalline nature of the samples, and so opened up possibilities for investigating the properties of non-

crystalline grating structures. Tolan *et al* [23] developed a model based on dynamical scattering theory which was able, to some extent, to provide a quantitative analysis of the experimental data from their samples.

Using this dynamical theory, studies were extended to examine the effect of depositing layers on such laterally modulated structures in order to study conformal roughness [24,25]. Since the use of gratings led to the enhanced, coherent scatter, in the form of diffraction orders, correlated roughness could be examined more easily in such samples as opposed to conventional multilayers. In the last two years work by Mikulik and Baumbach has extended these dynamical theories to include the scatter from multilayer grating structures [26-29]. Their experimental results have been compared with a variety of methods of analysis.

Whilst such dynamical theories do allow good quantitative analysis of the data obtained from grating structures, they are complex and mathematically involved. This investigation aimed to study the scatter from short period laterally modulated structures and construct a simpler, more physically intuitive model for the coherent scatter which could be combined with the usual form of the incoherent diffuse scatter.

To develop and test the model, experimental data were taken on two types of laterally modulated structure. The first consists of the laterally modulated substrates used in light emitting polymer fabrication. The bare substrate has been studied as have samples where, in one case aluminium and the other polymer, has been deposited onto the substrate. The structure of the lateral modulations in these cases is reasonably complicated (as will be discussed further in section 7.2) so in addition, an almost perfectly rectangular, GaAs grating has also been studied. This sample has provided a more ideal grating structure on which to test the limits of validity of various parts of the theory.

In discussing the development of the semi-kinematical model, the simpler case of a single surface will first be considered. The model of the coherent scatter will be developed for this case and the various corrections which are needed to account for the experimental configuration will be discussed. The theory will then be extended to consider a single layer deposited on a laterally modulated substrate and it will be

demonstrated how the diffuse scatter, generated using the Bede REFS model can be incorporated into the overall model. The validity and success of the model will then be examined.

7.2 The Samples and their Fabrication

The corrugated substrates, onto which the polymer films were spin coated, were prepared at the University of Exeter. A photoresist was deposited onto a silica coated slide and subsequently exposed to the interference pattern from two laser beams [8]. These lasers were set-up to give a resulting grating structure with a period of ~4000Å. Figure 7.1 shows an atomic force microscope (AFM) image of a prepared substrate kindly provided by Prof. J. P. S. Badyal of the Department of Chemistry, Durham University.
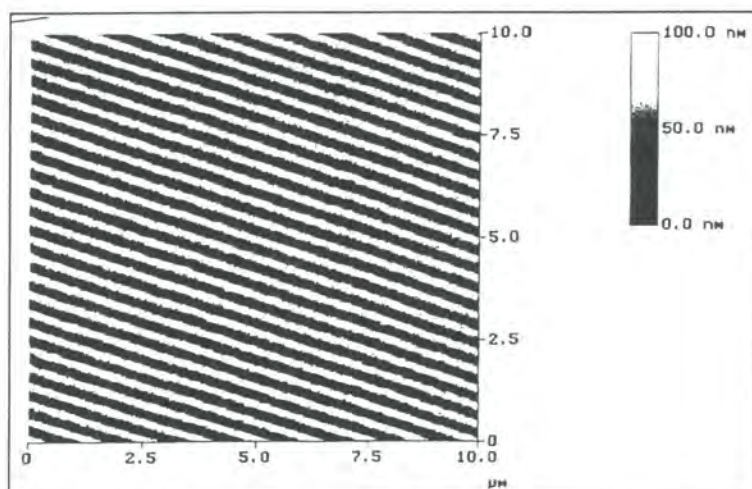
Figure 7.1 - AFM image taken of the etched photoresist substrate.

The grating structure of this substrate is evident in this picture with a period, measured from this image, of 4000 ± 40Å. In addition the grating structure appears to be very regular across a large length scale.

In order to make a light emitting device the polymer poly *(2-methoxy-5-(2'-ethylhexoxy)-p-phenylenevinylene)* (MEH-PPV) [30] was subsequently spin coated

onto this substrate at the University of Durham. For the purpose of these studies three samples were investigated :-

(1) - Bare, etched photoresist substrate

(2) - Etched substrate with MEH-PPV spin coated onto it.

(3) - Etched substrate with aluminium evaporated onto it.

Sample (3) was prepared as it was hoped that the aluminium would serve to enhance the scattered x-ray signal, making the modelling more simple. The typical thickness of the deposited layer was in the region of 150nm while the depth of the grating on the bare, etched photoresist was ~50nm.

The GaAs sample studied was prepared at the University of Potsdam in Germany. The sample was produced by electron beam lithography and subsequent dry etching of a GaAs / InGaAs / GaAs layered structure grown epitaxially on a GaAs epi-ready substrate. The nominal structure of the grating is shown schematically in figure 7.2.
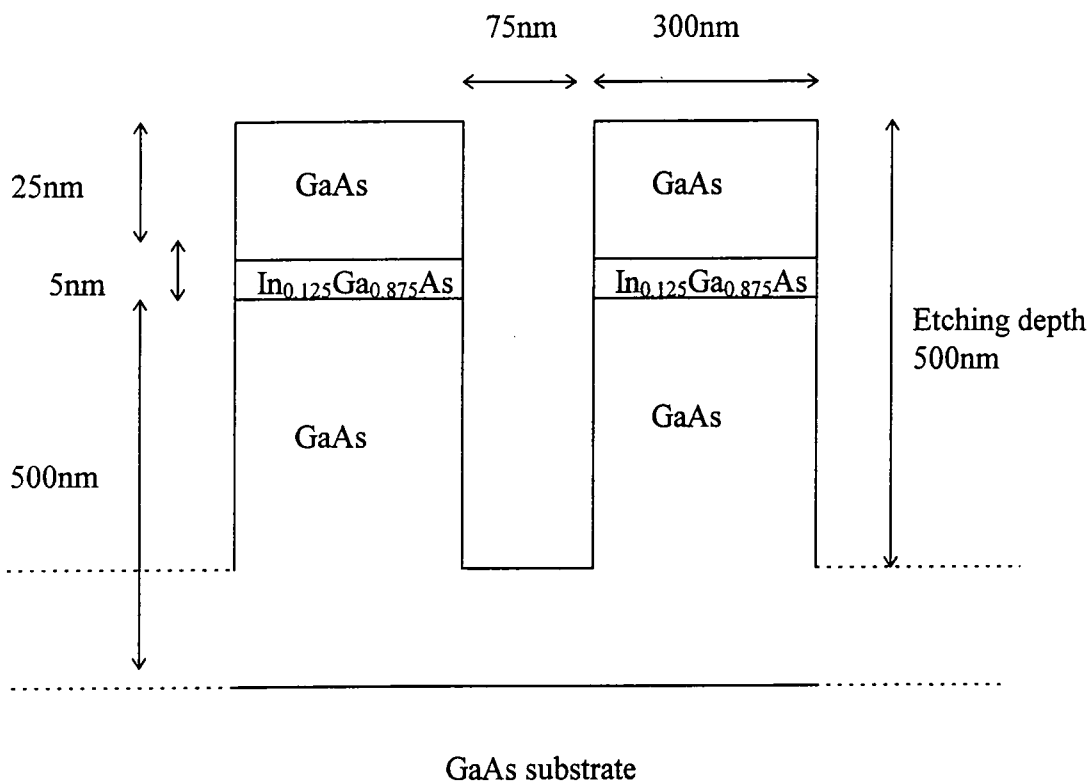

Figure 7.2 - Schematic representation of the GaAs Grating (all numbers are the nominal 'as grown' values)

Figure 7.3 shows an scanning electron microscopy (SEM) image of the sample, taken at the University of Potsdam, Germany.
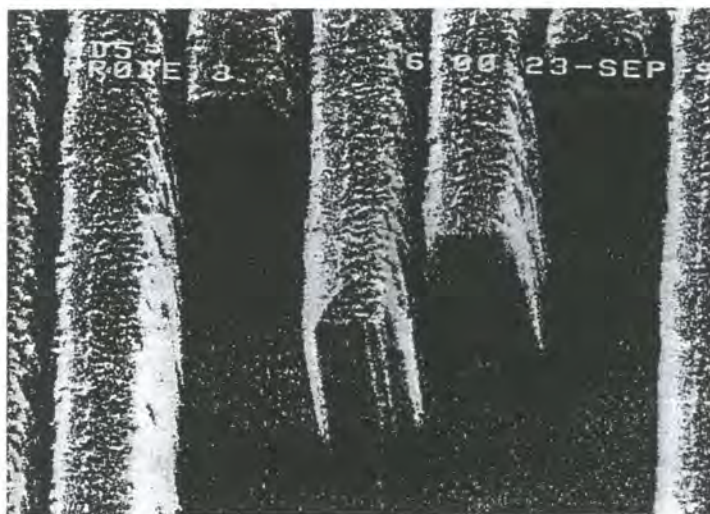

Figure 7.3 - SEM image taken of the surface of the GaAs grating

From a comparison of figures 7.1 and 7.3 it can be seen that the structure of the GaAs grating has an almost perfectly rectangular shape with narrow, deep troughs between the grating elements. In contrast, the photoresist substrate is slightly more corrugated in nature with shallower and more open troughs between the grating elements. Consequently, it was expected that the GaAs grating would exhibit more 'ideal' grating behaviour. In addition, since the layers within the GaAs have almost identical scattering powers it was expected that, to first order, this grating could be treated as a simple, single surface.

7.3 Experimental Methods

GIXS measurements were performed on these samples on the standard powder diffractometer of station 2.3 at the Daresbury SRS and also on the Bede GXR1 reflectometer at the laboratory in Durham. Experiments on the GaAs grating were carried out both in the laboratory and the SRS where a wavelength of 1.393Å was used for consistency. The polymer samples exhibited much weaker diffraction peaks so were

only studied at the SRS where a wavelength of 1.3Å was selected which corresponds to the maximum flux of the station. Typical reflectivity set-ups were used for each experiment with the experimental parameters being kept constant between sample runs. The majority of the data presented here were obtained at the Daresbury SRS where a 4mm by 100μm high beam was defined in front of the sample and the resolution slits in front of the detector were varied from 100μm to 500μm.

Unlike previous studies on such structures, where the period of the grating was sufficiently large to allow coherent diffraction orders to be observed with x-rays incident perpendicular to the grating structure [e.g. 16 or 23], the period of these gratings was so small no diffraction orders were observed in this orientation. In order to observe the coherent scatter the sample was rotated about its azimuthal axis thus increasing the effective grating period. This was performed on the GXR1 by utilising a standard axis on the reflectometer which rotates the sample table. At Daresbury a manual rotation stage was constructed to fit onto the sample arm of the diffractometer. This rotation table allowed manual rotation of the sample to a resolution of ±0.5° which was considered sufficient for this experiment. In retrospect, an accurate, mechanically driven table would have been more useful as the exact azimuthal angle was to prove crucial in later experiments.

By noting at which orientation visible light was diffracted, each sample was initially mounted on the rotation stage such that an azimuthal angle of 0° on the sample stage corresponded to the x-rays being incident perpendicular to the direction of the grating structure. The convention for this azimuthal angle is shown schematically in figure 7.4. This nomenclature will be used throughout to describe the azimuthal angle of the sample, ϕ. Since this initial setting was performed by hand, an inherent error of a few degrees often existed between the azimuthal angle of 0° and the true 0° of the grating. This offset varied from sample to sample.
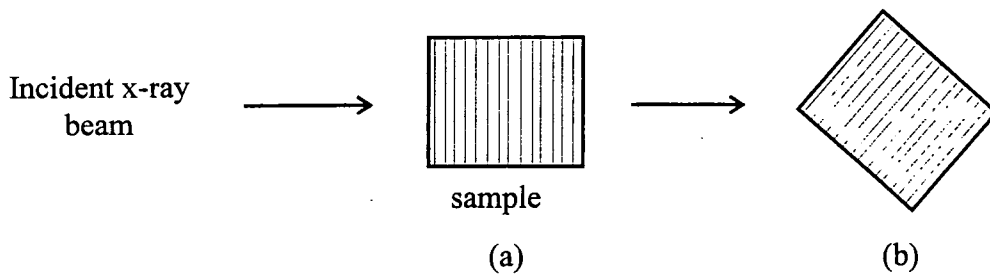
Figure 7.4 - Schematic representation of the alignment of the grating on the sample stage showing the sample at an azimuthal angle of (a) 0° and (b) 45°.

7.4 Experimental Data

In presenting these data the emphasis is given to the data from the polymer samples. In certain cases, however, the data from the GaAs grating will be shown since the coherent scatter is typically more intense and certain effects are emphasised more clearly.

Specular and off-specular scans were taken for all the samples as a function of azimuthal angle. Figure 7.5 shows examples of the specular and off-specular scatter taken for the polymer deposited onto the etched photoresist substrate.

Figure 7.5 - Specular (upper curves) and off-specular (lower curves) for the MEH-PPV deposited on the etched photoresist substrate for two sample azimuthal angles.

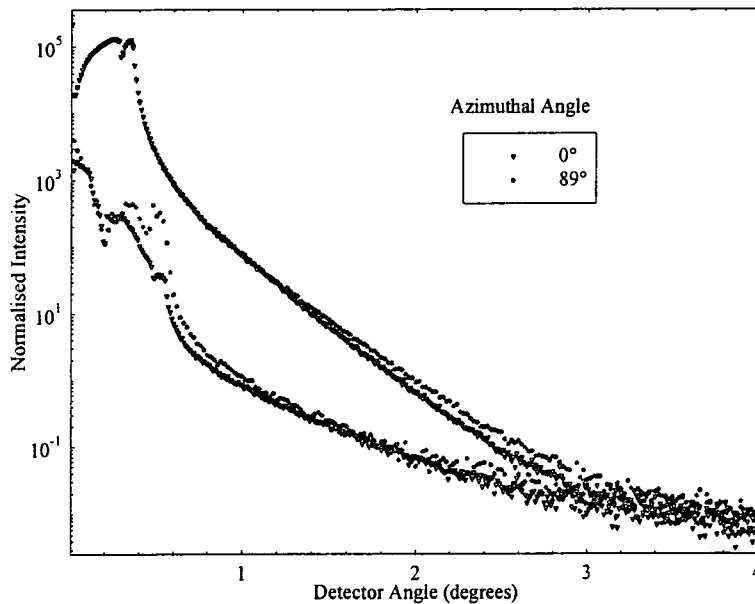As can be seen from figure 7.5, the specular and off-specular scans are very similar for both azimuthal angles. For all the samples studied in these experiments it was found that the true specular scatter was in fact invariant as a function of sample azimuth. This is further demonstrated in figure 7.6 where the true specular scatter from the GaAs grating is shown at three azimuthal angles.
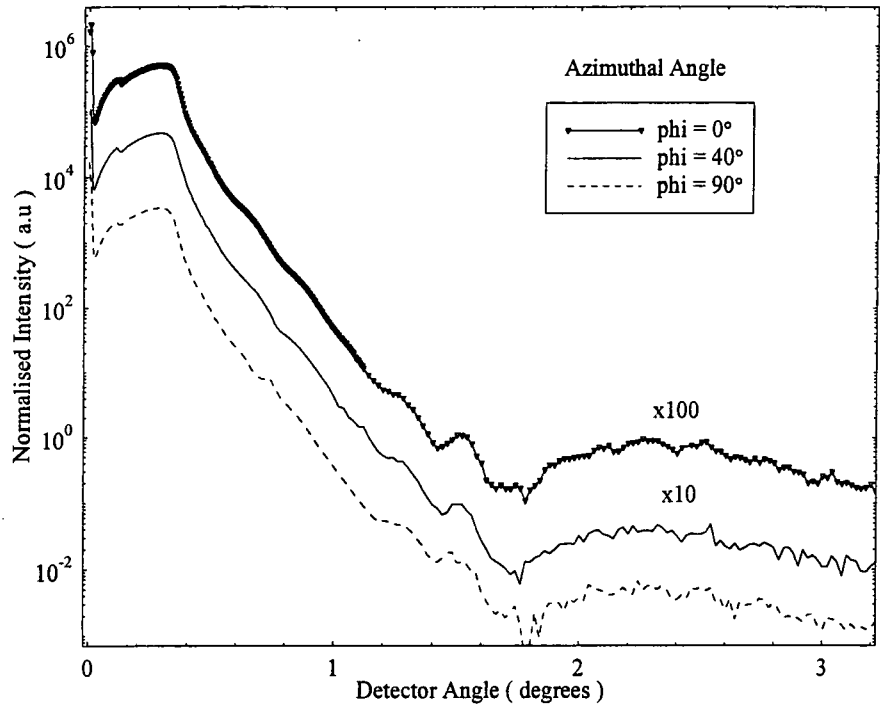
Figure 7.6 - True specular scatter from the GaAs grating taken for three azimuthal angles. Curves are offset for clarity.

As for the polymer grating, there is no observable change in the true specular scatter from the GaAs grating as a function of azimuthal angle. It is noted in both figures 7.5 and 7.6 that a double critical angle is observed in the true specular scatter. Such a feature is typical of a grating structure and has been observed and modelled previously by other groups [23,31]. In addition it was observed that, for all the samples, the critical angle, in the specular scatter, always corresponded to that of an average surface where the density of the 'average surface' was given by the ratio of the gratings surface to hole width.

Figure 7.7 demonstrates this effect, where simulations close to the critical angle are shown for the true specular scatter from the GaAs grating.
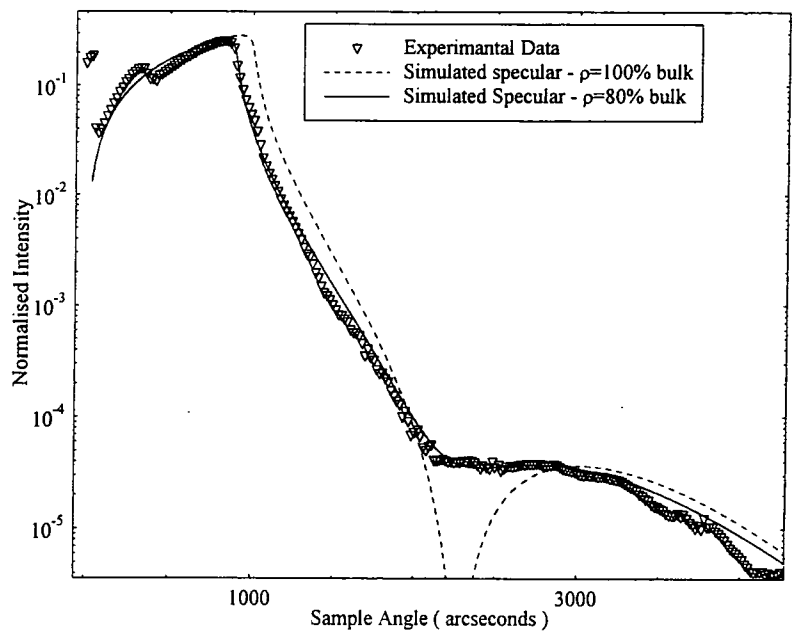
Figure 7.7 - Experimental true specular scatter from the GaAs grating with simulations performed with both the bulk density (dotted line) and density of an average surface (full line). All other sample parameters were unchanged between simulations.

As can be seen from the simulations in figure 7.7 it is crucial that the average density of the surface is used if a realistic simulation is to be obtained. For the case of the GaAs shown here a density of 80% bulk GaAs was used. If the nominal parameters of the grating from figure 7.2 are used it can be seen that the ratio of surface to 'holes' is ~ 4/1 or, in other words, only 75% of the surface is present. Given the errors in the measurements of these parameters from the AFM and SEM images, the agreement between this value and the one which is used to obtain the average density is excellent. Such an effect has been observed previously, both in gratings [31] and in ground, lapped and polished ceramic samples [32,33].

Transverse and detector only scans were performed on all the gratings. It was found that the diffraction orders, due to the coherent scatter from the gratings, could only be

observed at azimuthal angles close to 90° where the apparent period of the grating increased significantly. These diffraction orders were seen to be symmetric about the specular ridge (m = 0 diffraction order) in the transverse diffuse scans and the peaks moved systematically on rotation of the sample about its surface normal. This is demonstrated extremely well in figure 7.8 where a series of transverse diffuse scans as a function of azimuthal angle are shown.
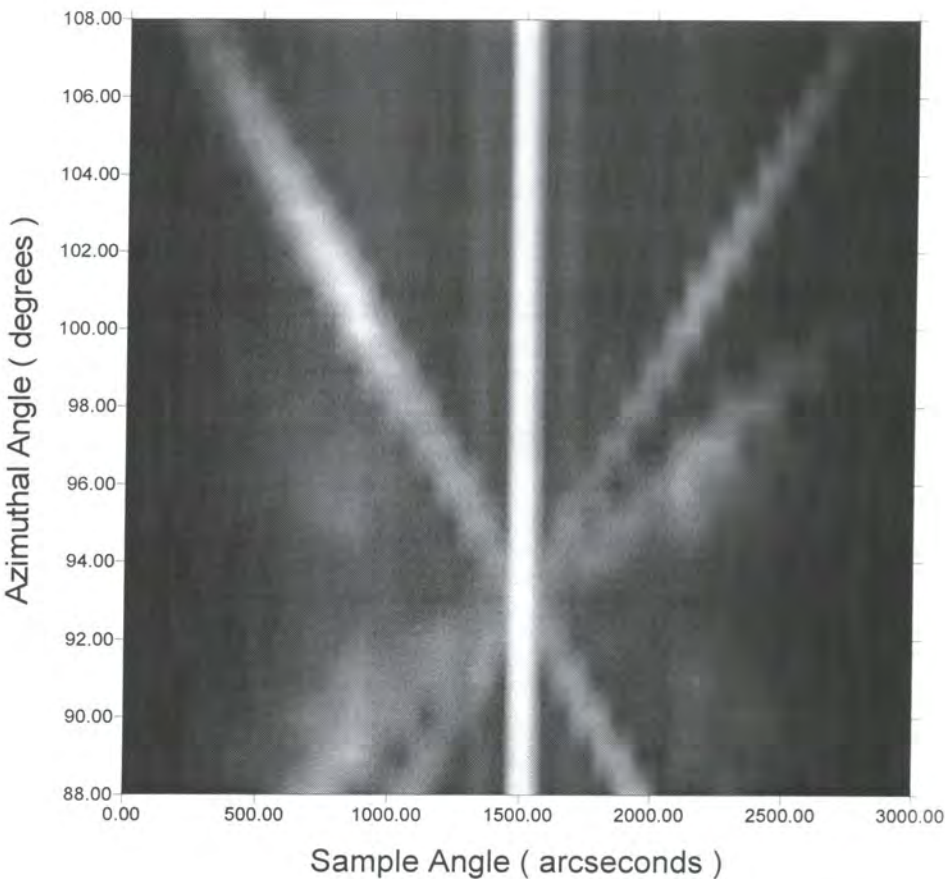
Figure 7.8 - Pixilated image of a large number of transverse diffuse scans taken as a function of azimuthal angle. All transverse scan were taken at a fixed scattering angle of 3000''.

The specular ridge in figure 7.8 (or m = 0 diffraction order) is the intense band running down the middle of the image at a sample angle of 1500''. The m = ±1 (coherent) diffraction orders cut the image diagonally. The position these diagonals cross is where the azimuthal angle is such that the x-rays are passing straight down the grooves of the grating. Consequently the apparent period of the grating tends to infinity and no such

coherent scatter is observed. Around this point the weak m = ±2 diffraction orders can also be observed. It should be noted that the azimuthal angle at which these lines intersect is not exactly 90° and this is for reasons of sample misalignment, as discussed previously.

Transverse diffuse scans were also taken for the samples with the etched photoresist substrates. An example of typical transverse diffuse scans from both the polymer and aluminium on the etched substrate are shown in figures 7.9a and 7.9b and compared to a typical transverse diffuse scan from the GaAs grating in figure 7.9c.

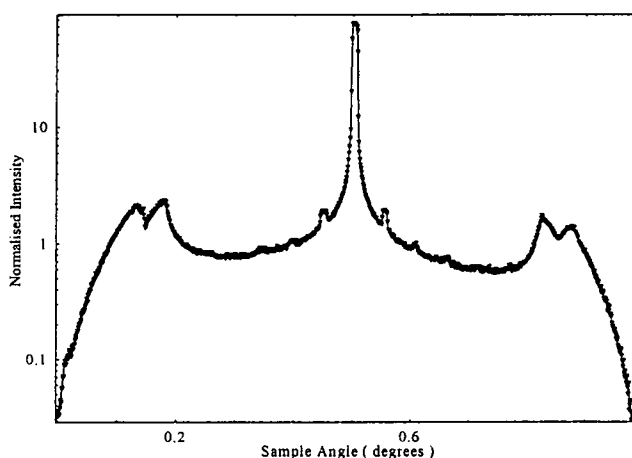Figure 7.9a - Transverse diffuse scan from the polymer deposited on the etched photoresist substrate. Scattering angle of 1.0° was used.
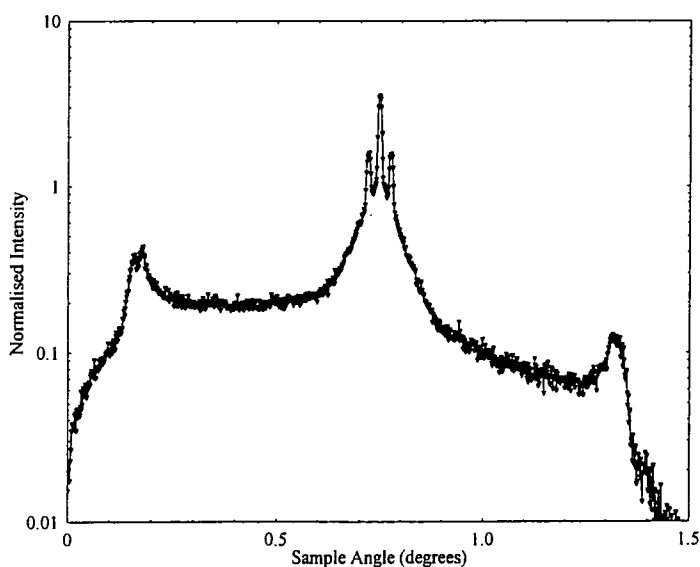

Figure 7.9b - Transverse diffuse scan from the aluminium deposited on the etched photoresist substrate. Scattering angle of 1.5° was used.
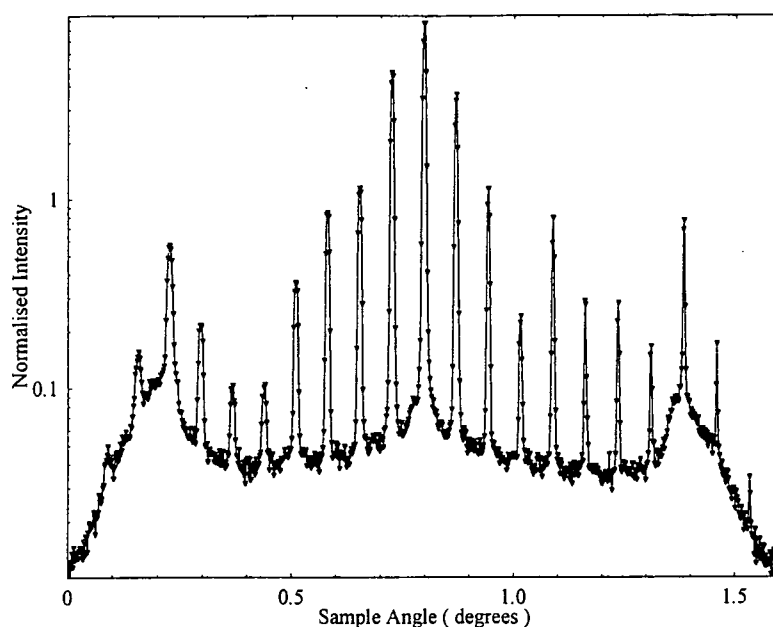
Figure 7.9c - Transverse diffuse scan from the GaAs grating. A scattering angle of 1.6°
was used.

The intensity of the coherent scatter from the GaAs grating is considerably higher than
that from the polymer grating. Consequently the number of visible diffraction orders for
the GaAs is much greater than for either the polymer or aluminium samples with all the
orders up to m = ±10 being observed in the former whilst only the m = ±1 orders are
clearly visible for the others, the m = ±2 and ±3 being faintly seen. The incident
intensity and count times were comparable for all experiments. This large difference in
intensity is due not only to the more ideal grating shape of the GaAs sample, but also to
the greater scattering factor of the GaAs compared to the other samples. In addition, it
would be expected that due to the different growth techniques, the GaAs grating would
have a smoother surface and, as such, have more intense diffraction orders. The polymer
sample seems to show a good surface grating structure with several weak, but
observable, diffraction orders being present. In contrast only two diffraction orders are
visible with the aluminium sample suggesting the periodicity is variable. This could,
perhaps, be a result of the grating structure of the substrate having been washed out by
the deposition of the aluminium. The shape of the overall diffuse scatter from this
sample would also suggest it is dominated by a long correlation length roughness (see

136

chapter 2.4.3), an interpretation which would be consistent with the washing out of the grating structure.

Whilst an image such as figure 7.8 provides an excellent qualitative summary of the type of scatter expected from such a structure, more useful, quantitative results have been obtained from an interpretation of the individual scans. Figure 7.10 shows a series of detector only scans taken from the etched photoresist substrate as a function of azimuthal angle.
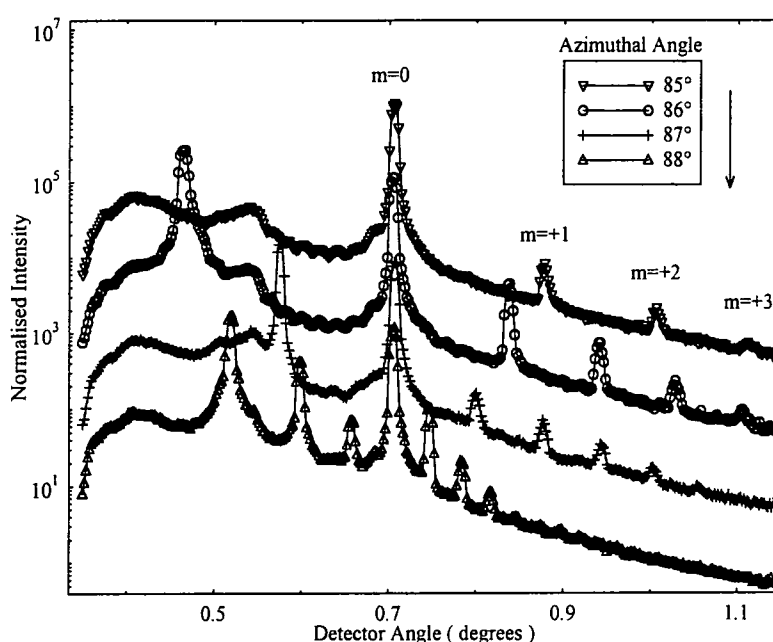
Figure 7.10 - Detector only scans taken from the etched photoresist substrate at various azimuthal angles. A fixed sample angle of 0.35° was used for all scans. Subsequent scans are offset for clarity. The diffraction orders are marked for the first curve.

Figure 7.10 demonstrates several important features which are observed in the scatter from such a laterally modulated structure. It is seen that when the sample is rotated to an azimuthal angle of 85°, several diffraction orders are seen in the scatter. These diffraction orders move together as the sample is rotated towards an azimuthal angle of 90° and the number of visible peaks increases. If all the data from this experiment were to be shown, similar behaviour to that observed in figure 7.8 would be seen. As the sample is rotated through 90°, all the diffraction peaks get closer together and disappear

before reappearing and spreading out again. Beyond an azimuthal angle of ~65° no diffraction orders are visible in the scatter. This corresponds to apparent grating spacing of ~ 10000Å, similar to the real period of gratings used by other groups [e.g. 16 or 23].

From a simple geometrical analysis, the apparent spacing of the grating, d', is related to the true spacing of the grating, d, by

$$d' = d / \cos\phi \quad - (7.1)$$

where ϕ is the azimuthal angle of the sample as has been defined for these experiments.

It was found that the position of these diffracted orders followed the standard grating equation [e.g. 21] very closely, which states that the position of the diffracted orders depends on the apparent spacing of the grating such that,

$$d' (\cos\theta_{incident} - \cos\theta_{exit}) = m . \lambda \quad - (7.2)$$

Where m is the order of the diffraction peak and λ the incident wavelength

From the type of scan shown in figure 7.10, the apparent grating spacing can be calculated as a function of azimuthal angle using these equations and consequently the real period of the grating can be accurately determined. Figure 7.11 shows the results of such an analysis for the etched photoresist sample.
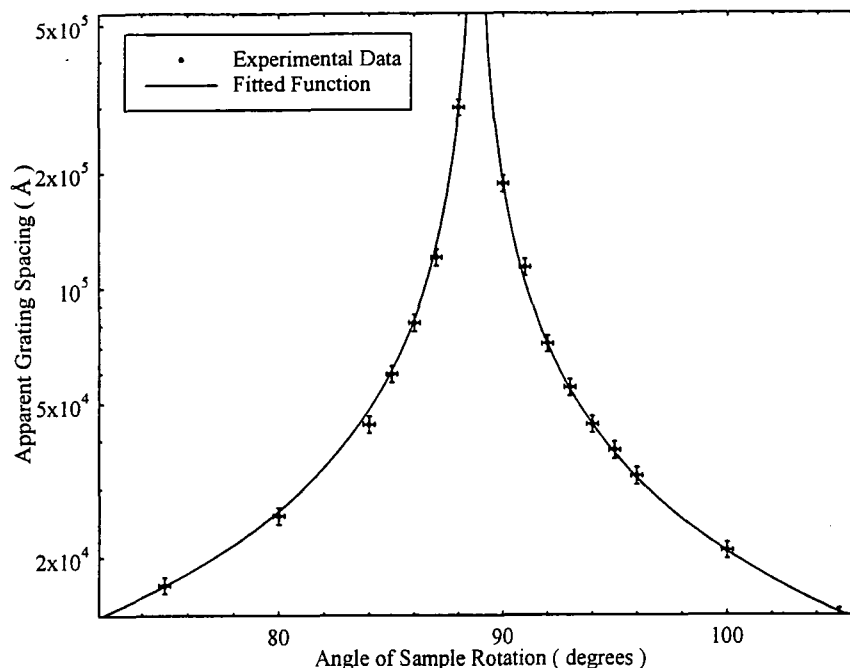
Figure 7.11 - Apparent spacing of the grating as a function of azimuthal angle. Experimental data points are fitted to a 1 / cos relation.

As can be seen from figure 7.11 excellent agreement is obtained between the experimental and fitted data. The resulting true grating period, d, which is obtained from this analysis is 4018 ± 50Å which agrees extremely well with that obtained from the AFM image.

Using an identical analysis technique the periods of the other gratings were also determined. With aluminium deposited on the photoresist the true period of the grating was determined to be 3758 ± 100Å and that with MEH-PPV deposited was found to have a period of 3868 ± 150Å. The larger associated errors with these latter samples are due to the weaker diffraction peaks which are observed and consequently the poorer statistics in the fit. It is interesting to note, however, that in both cases, when a layer is deposited onto the etched substrate, a smaller grating period is observed than for the bare substrate itself. Additionally, within the experimental errors, the period of the deposited samples are the same.

Such analysis demonstrates the ability of x-rays to determine accurately the period of such laterally modulated structures and shows how well the results agree with experimental data. In order to obtain much more useful information, such as surface and

sub-surface roughness and an indication of correlation between the interfaces, a more detailed way of modelling the coherent scatter is required.

7.5 Modelling the Coherent Scatter

7.5.1 Single Surface

In developing the model for the coherent scatter, the case for a single surface will first be developed. These ideas will then be extended to consider the case of a layer deposited onto a laterally modulated surface. The derivation presented here is closely based on that of Morrison [34] where the coherent scatter is analysed in an analogous manner to that for a grating operating with visible light. In using this treatment it is assumed that the grating structure is substantially larger than the wavelength of the incident light and effects of polarisation in the incident wave are neglected.

For the case of a single surface a structure has been assumed as is shown schematically in figure 7.12.
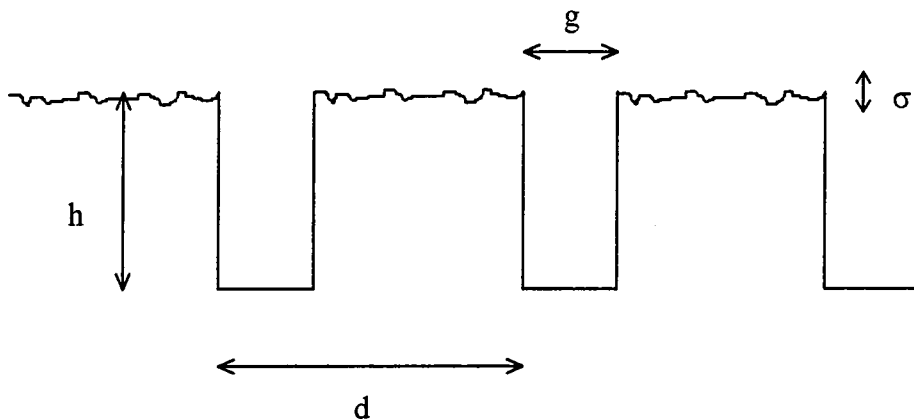
Figure 7.12 - Schematic representation of the single surface assumed in the model for the coherent scatter from a laterally modulated surface.

In this model a real grating spacing, d, has been assumed where g is the width of the holes between adjacent grating elements. These holes have a depth of h and a Gaussian

distribution of height fluctuations, σ, is assumed about the mean surface of each grating element.

In this model it is further assumed that the point of observation is in the far field regime (extreme Fresnel) such that all the waves can be regarded as plane waves within the model and the diffracted amplitude is simply proportional to the Fourier transform of the function which describes the grating structure.

Each of the rectangular grating elements is considered to act as a point scatterer, as shown schematically in figure 7.13.
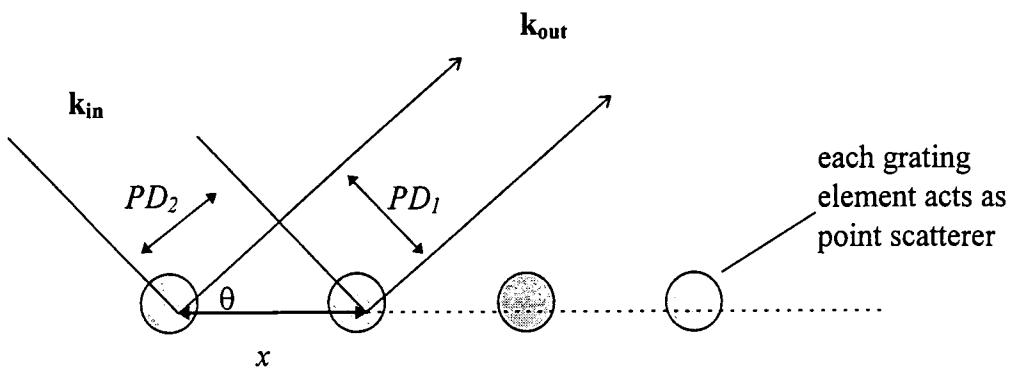
Figure 7.13 - Schematic representation of each grating element acting as a point scatterer on the surface of the sample.

In this case, each grating element is separated by a distance x and path differences of PD_1 and PD_2 are introduced into the reflected and incident wavefront respectively, for an angle of incidence θ. $\mathbf{k_{in}}$ and $\mathbf{k_{out}}$ are the wavevectors of the incoming and outgoing waves respectively.

So, from the geometry of the situation in figure 7.13, it can be seen that for the outgoing wave the path difference, PD_1, is given simply by,

$$PD_1 = x.\cos\theta - (7.3)$$

By relating this to the difference in phase introduced into the reflected wavefront and, similarly, the phase difference in the incoming wave, an expression is reached for the total change in phase, ϕ_T, where

$$\phi_T = \text{x.q}_\text{x} \qquad \text{-}\,(7.4)$$

For a plane wave incident on a surface such as shown in figure 7.13, the coherently reflected intensity as a function of q_x will be given [35] by,

$$E(q_x) = E_0 \int_{-\infty}^{\infty} f_N(x)[\exp(-i.q_x.x)]dx \qquad \text{-}\,(7.5)$$

where $f_N(x)$ is a function which describes the surface of the grating and E_0 is the incident electric field intensity. For this particular case a perfectly rectangular surface is assumed and the depths of the holes are considered to be infinite such that reflections from the lower surface can be ignored. By looking at the SEM image, figure 7.3, this can be seen to be a valid approximation for the GaAs grating.

For this assumption, therefore $f_N(x)$ can be written as

$$f_N(x) = \sum_{n=0}^{n=N-1} f(x) \otimes \delta(x - x_n) \qquad \text{-}\,(7.6)$$

where $f(x)$ is either 1 or 0 and $\delta(x - x_n)$ is a series of delta functions and N is the number of coherently illuminated grating elements. Hence, by carrying out the convolution in (7.6) a series of 'bars' are obtained which represent the scattering surfaces of the grating elements.

Substituting (7.6) into (7.5) gives,

$$E(q_x) = E_0 \int_{-\infty}^{\infty} \left[\sum_{n=0}^{n=N-1} f(x) \otimes \delta(x - x_n) \right] [\exp(-i.q_x.x)]dx \qquad \text{-}\,(7.7)$$

However, since this equation represents the summing of various phases $\int_{-\infty}^{\infty} \exp(-i.q_x.x)$ is actually defining a Fourier transform and since the Fourier transform of a convolution is simply the multiplication of the individual Fourier transforms,

142

equation (7.6) can be rewritten so that the individual Fourier transforms are calculated separately.

The two separate Fourier transforms therefore simplify to become,

(a) $\int\limits_{-\infty}^{\infty} f(x)\exp(-i.q_x.x)dx = F(q_x)$ which can be evaluated, and

(b) $\int\limits_{-\infty}^{\infty}\left|\sum\limits_{n=1}^{n=N-1}\delta(x-x_n)\right|\exp(-i.q_x.x)dx = \sum\limits_{n=1}^{n=N-1}\exp(-i.q_x.x_n)$ since $\delta(x-x_n)$ is either 1

or 0 by definition.

The expression for (b) is a simple geometric series which has a standard result [34] where,

$$\sum\limits_{n=1}^{n=N-1}\exp(-i.q_x.x_n) = \frac{\sin N.d.(q_x/2)}{\sin d.(q_x/2)} \qquad - (7.8)$$

The evaluation of (a) is slightly more complex although relying only on simple integration. Following Morrison [34], the grating surface is described as, $f(x) = 1$ for $g/2 < |x| < d/2$ and $= 0$ elsewhere. Therefore,

$$F(q_x) = \int\limits_{-d/2}^{-g/2}\exp(-i.q_x.x)dx + \int\limits_{g/2}^{d/2}\exp(-i.q_x.x)dx$$

$$= \frac{-2}{q_x}\left[\frac{\exp(i.q_x.g/2)-\exp(-i.q_x.g/2)}{2i}\right] + \frac{2}{q_x}\left[\frac{\exp(i.q_x.d/2)-\exp(-i.q_x.d/2)}{2i}\right]$$

$$= \frac{-2}{q_x}\left[\sin(q_x.g/2)-\sin(q_x.d/2)\right]$$

A final, compact expression for $F(q_x)$ is obtained, namely,

$$F(q_x) = \frac{\sin(q_x.d/2)-\sin(q_x.g/2)}{q_x/2} \qquad - (7.9)$$

143

To obtain a final expression for $E(q_x)$ equations (7.8) and (7.9) are substituted into (7.7) such that,

$$E(q_x) = E_0 \left[\frac{\sin(q_x.\frac{d}{2}) - \sin(q_x.\frac{g}{2})}{\frac{q_x}{2}} \right] \cdot \left[\frac{\sin N.d.(\frac{q_x}{2})}{\sin d.(\frac{q_x}{2})} \right]$$

The intensity, $I(q_x, q_z)$ is, therefore,

$$I(q_x, q_z) = E_0^{\,2} \cdot \left[\frac{\sin(q_x.\frac{d}{2}) - \sin(q_x.\frac{g}{2})}{\frac{q_x}{2}} \right]^2 \cdot \left[\frac{\sin^2 N.d.(\frac{q_x}{2})}{\sin^2 d.(\frac{q_x}{2})} \right]$$

which can be rewritten as,

$$I(q_x, q_z) = |R(q_z)|^2 \cdot \left[\frac{\sin(q_x.\frac{d}{2}) - \sin(q_x.\frac{g}{2})}{\frac{q_x}{2}} \right]^2 \cdot \left[\frac{\sin^2 N.d.(\frac{q_x}{2})}{\sin^2 d.(\frac{q_x}{2})} \right] \text{ - (7.10)}$$

where $R(q_z) = R_f \exp\left[-q_z^{\,2}\sigma^2\right]$. Using this formalism allows the effect of roughness to be included into the model. The value for $R(q_z)$ can be evaluated using the Bede REFS software for a particular sample since it is simply the absolute value for the reflectivity amplitude at a given q_z.

Finally, equation (7.10) must be normalised so that as q_x tends to zero, the expression returns a value of $R(q_z)^2$. By evaluating the expression in this limit it is found that the normalisation term is $\left(\dfrac{1}{N^2(d-g)^2}\right)$. Consequently, the final expression for the intensity of the coherent scatter as a function of q_x from a laterally modulated, single surface is,

$$I(q_x, q_z) = |R(q_z)|^2 \cdot \left(\frac{1}{N^2(d-g)^2}\right) \left[\frac{\sin(q_x.\frac{d}{2}) - \sin(q_x.\frac{g}{2})}{\frac{q_x}{2}} \right]^2 \cdot \left[\frac{\sin^2 N.d.(\frac{q_x}{2})}{\sin^2 d(\frac{q_x}{2})} \right]$$

$$\text{- (7.11)}$$

Whilst the expression itself is relatively simple, some of the terms within the expression need further consideration and in order to model successfully the coherent scatter the effects of the instrument resolution must also be considered.

7.5.2 Calculating N

As is obvious from equation (7.11), the intensity of the coherent scatter is strongly dependent on N, the number of coherently illuminated grating elements. Two factors have to be addressed in its calculation. The first is simply a geometric argument since as the angle of incidence is increased, the projected coherent footprint of the beam will cover a smaller area of the sample and the total number of illuminated periods will decrease.

The second factor is slightly more complex as for coherent scattering to occur, N must reflect the number of grating elements which lie within a coherence length at any given angle. Grating elements lying outside this coherence length will not interfere and therefore not add to the coherent scatter. Recently, detailed work has been published on the effects and meaning of coherence [36] where both coherence and instrumental effects have been considered.

In this model, the question has been addressed from two standpoints. Initially, the number of coherently illuminated periods has been calculated using the coherence length of the incident beam. In addition, the number of periods which are seen to be coherently emitting at the detector has also been calculated.
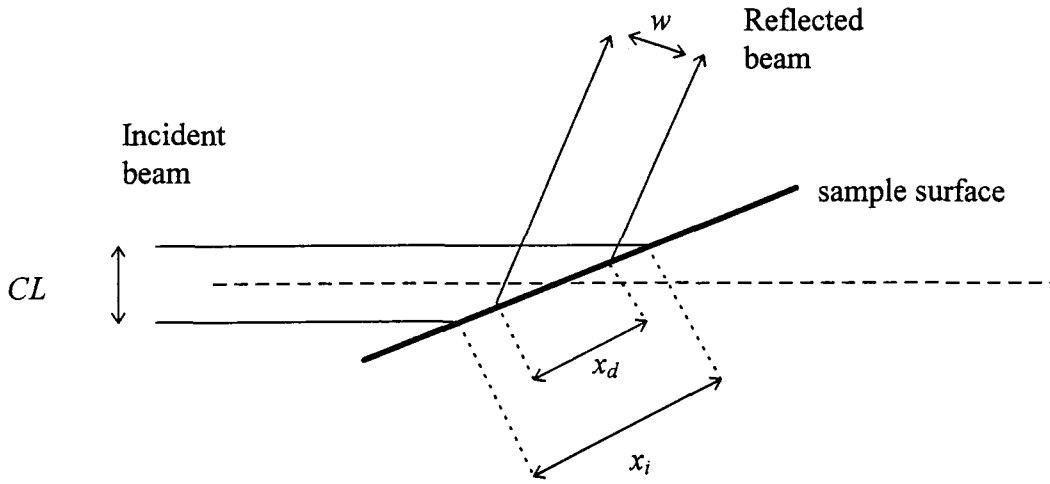
Figure 7.14 - Schematic representation of the geometry of the incident and reflected beam on a sample.

In the geometry of figure 7.14, the incoming beam is incident on the sample at an angle θ_i and observed by a detector, a distance z away, at an angle of θ_d. The apparent period of the grating, d' is given by equation (7.2) and CL and w are the 'coherence lengths' of the incoming and outgoing beams respectively.

For the incident beam, the coherence length is simply calculated in the standard way [e.g. 22] where,

$$CL = \frac{\lambda.r}{r_s} \qquad - (7.12)$$

where r is the source - sample distance and r_s is the size of the source. It is therefore easy to calculate geometrically the number of coherently illuminated periods, N_i, since,

$$\sin\theta_i = \frac{CL}{x_i} \quad \text{and therefore}$$

$$N_i = \frac{x_i}{d'} = \frac{CL}{d'.\sin\theta_i} \qquad - (7.13)$$

The calculation of the number of coherently observed periods, N_d, is slightly more involved. Consider a point emitter on the surface of the sample. Two points, A and B, lie on the emitted plane wavefront, a distance x apart and are said to be a certain amount,

ρ, out of phase. The distance from the point source to A is r' and that to B is r. With the wavevector of the wave defined as $k = 2\pi/\lambda$ then the phase between these two points is simply,

$$\rho = kr - kr' = 2\pi/\lambda (r - r')$$

but $r^2 + x^2 = r'^2$, so

$$\rho = \frac{2\pi.r}{\lambda} - \frac{2\pi}{\lambda}(r^2 + x^2)^{0.5}$$

which gives the expression relating the distance, x, between two points which are ρ out of phase. Since, in the definition of the problem, w has been defined as the reflected coherence length it can be shown that,

$$w = \frac{\rho.\lambda}{\pi}\left(\frac{1}{4} - \frac{\pi.r}{\rho.\lambda}\right)^{\frac{1}{2}}$$

where the value of ρ can be varied to give the outgoing coherence length for any particular value of phase difference, meaning the model is not restricted to a particular definition of 'outgoing' coherence.

It follows, geometrically, that

$$N_d = \frac{\rho.\lambda}{\pi.d'.\sin(\theta_d - \theta_i)}\left(\frac{1}{4} - \frac{\pi.z}{\rho.\lambda}\right)^{\frac{1}{2}} \quad \text{- (7.14)}$$

To obtain the actual value of N used in the calculation for the coherent scatter, N_d and N_i are calculated for each sample angle (figure 7.15) and the smallest possible value of N, for any particular sample angle, is used.
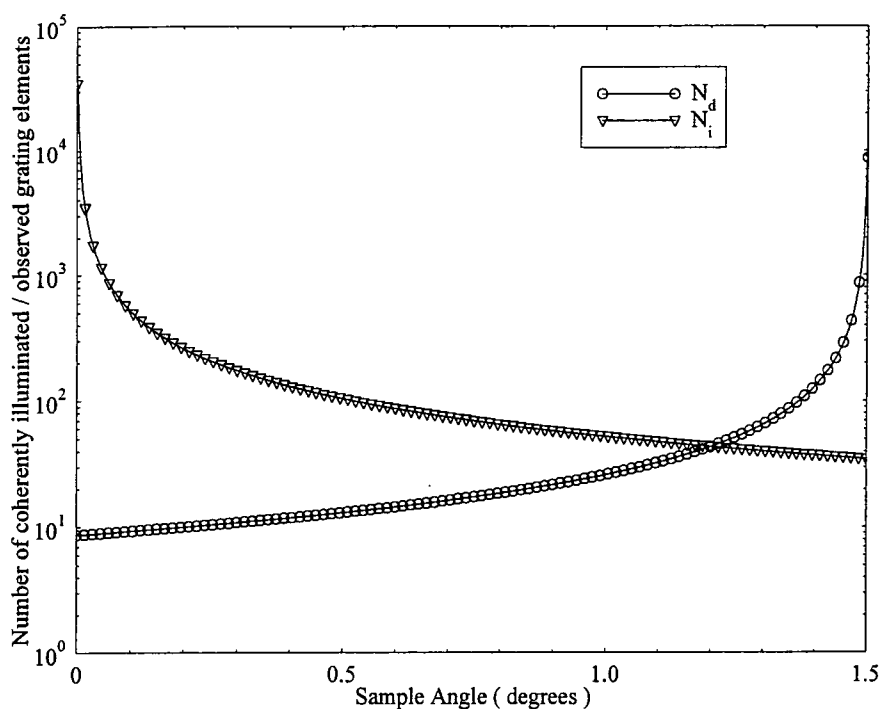
Figure 7.15 - Calculated values for N_i and N_d as a function of sample angle. The value of N used is least value from the two curves at any given sample angle.

These curves have been calculated for a fixed detector angle of 1.5°and a wavelength of 1.393Å. The sample has a nominal period of 4000Å with a hole size of 300Å and is at an azimuthal angle of 85°. A source size of 5×10^{-4}m has been specified and a source to sample distance of 15m. These parameters are typical values for a synchrotron source where the 'source' of the x-rays is considered to be where they are first generated not at the last piece of optics in the beamline. This assumption is justified as the coherence length of the beam is always much smaller than any of the slits in the optics of the beamline, resulting in no diffraction taking place. In addition the only reflections which take place within the optics are from symmetric, Bragg reflecting crystals meaning there is no effect on the shape of the wavefront or mixing of wavelengths. Consequently, photons of any particular wavelength travel from the source to the sample without a change in their coherent properties. For the outgoing wave, in this calculation, a minimum phase difference of $\pi/100$ has been specified in the calculation of N_d. This value has been chosen after detailed analysis of the effect of varying this parameter on the calculated coherent scatter. From figure 7.15 it is noted that the final value for N

which is used in the calculation of the coherent scatter varies from a minimum of ~10 to a maximum of ~50.

7.5.3 Additional Correction Terms

Several other corrections must also be taken into consideration in order to ensure the correct form of the coherent scatter is obtained.

7.5.3.1 Fresnel Transmission Coefficients

As in the case of the usual diffuse scatter, the coherent scatter must also be multiplied by the Fresnel transmission coefficients to account for the increase in intensity when the critical angles for the incoming and reflected beam are satisfied.

From a general consideration of the propagation of electromagnetic radiation, Fresnel's and Snell's laws are used in the small angle approximation to express the refractive index of the sample in terms of angles.

It is found that the ratio of the transmitted amplitude, A_T, and the incident amplitude of the waves, A_I, can be expressed as,

$$\frac{A_T}{A_I} = \frac{2\theta_1}{\theta_1 + \theta_2} \qquad \text{- (7.15)}$$

where θ_1 and θ_2 are the incident and exit angles respectively.

Assuming that absorption can be neglected it can be shown that [37],

$$\theta_2 = \sqrt{\theta_1^2 - \theta_c^2} \qquad \text{for } \theta_1 \geq \theta_c \text{ and}$$

$$\theta_2 = i\sqrt{\theta_c{}^2 - \theta_1{}^2} \qquad \text{for } \theta_1 \le \theta_c$$

Substitution of these expressions into equation (7.15) results in two expressions for the intensity correction being calculated, one for angles less than the critical angle, θ_c, and one for angles greater than θ_c. For angles less than θ_c the correction term is calculated to be

$$\left|\frac{A_T}{A_I}\right|^2 = 4 \cdot \frac{\theta_i{}^2}{\theta_c{}^2}$$

where θ_i is the angle of incidence. For angles greater than θ_c the correction term is calculated to be

$$\left|\frac{A_T}{A_I}\right|^2 = \frac{4\theta_i{}^2}{2\theta_i(\theta_i{}^2 - \theta_c{}^2)^{\frac{1}{2}} + 2\theta_i{}^2 - \theta_c{}^2}$$

These expressions are then calculated for a given θ_c which is measured from the specular scatter for the sample in question and the resulting values are in complete agreement with those calculated by Lengeler [37]. The form of the correction term, as a function of sample angle, generated for the same model as figure 7.15, is shown in figure 7.16. A critical angle of 0.245°, which was the measured critical angle for the GaAs sample, is used in the calculation.
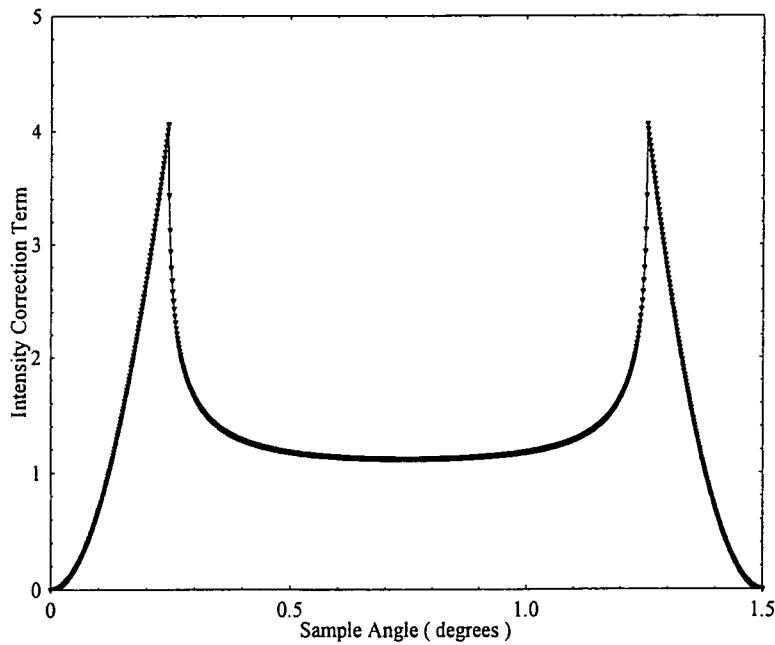

Figure 7.16 - Form of the Calculated Fresnel Correction Term

7.5.3.2 Beam Spill-off

Another geometric correction is made to account for the fact that at low angles not all the beam is incident on the sample. This correction term is only applied when,

$$\frac{b}{\theta_i} > L$$

where b is the height of the incident beam and L is the length of the sample. In this case the intensity of the coherent scatter is multiplied by,

$$\theta_i \cdot \left(\frac{A}{b}\right)$$

Where this correction is not needed the correction factor is set to unity. This correction is a direct consequence of the conservation of energy.

7.5.4 Instrument Resolution

When carrying out transverse diffuse scans on the samples it was observed that the width of the diffraction orders changed as a function of sample angle. A study was made of how the width of these peaks changed as a function of the size of the detector slit. The size of the incident beam was kept constant at 4cm by 100μm high and the height of the detector (or resolution) slits was varied. Figure 7.17 shows the results of this experiment for the GaAs grating, where the effects were the most pronounced.
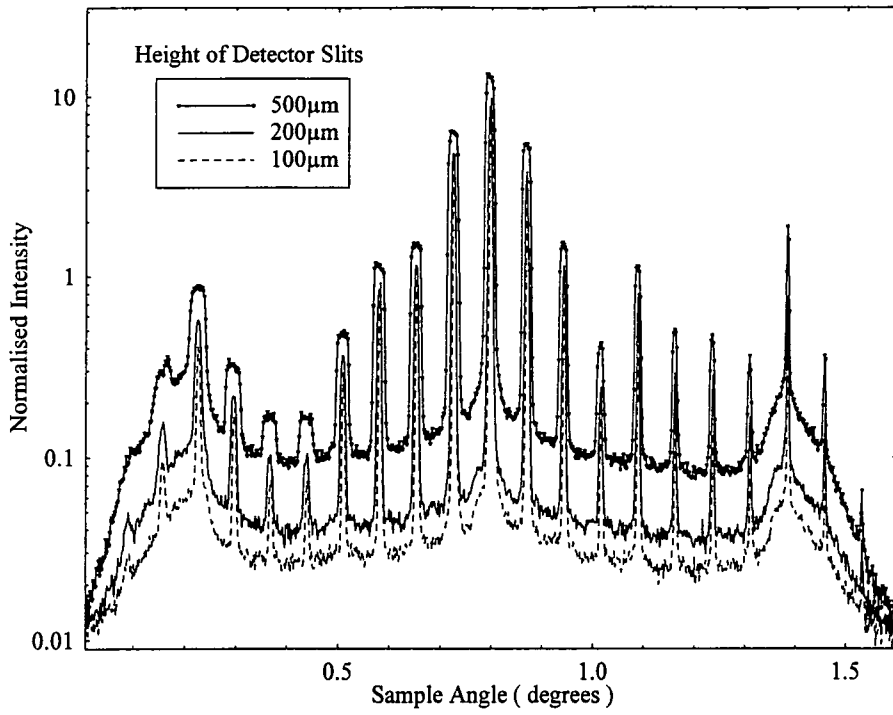
Figure 7.17 - Transverse diffuse scans taken for the GaAs grating as a function of detector slit height. A constant detector angle of 1.6° was used and the azimuthal angle was 87°.

As can be seen from figure 7.17 the width of the diffraction orders decreases as the sample angle increases in all cases. As the height of the detector slits is increased the width of the diffracted orders also increases.

This change in the width of the diffraction orders has been explained elsewhere [38] by a complex analysis of the resolution of the instrument and coherence of the beam.

Here a more simple approach is taken. It is assumed that there are uncertainties in the incident and exit angles due to the finite divergence of the incident beam and the finite angular acceptance of the detector slit. The uncertainties in the incident and exit angles, $\Delta\alpha_i$ and $\Delta\alpha_f$ respectively, are assumed to be random quantities which follow a Gaussian distribution where α_i and α_f denote the incident and exit angles with respect to the surface of the sample.

A particular scattering vector, $\mathbf{q}$, can be expressed in terms of the incident and exit wave vectors, $\mathbf{k_i}$ and $\mathbf{k_f}$ respectively as $\mathbf{q} = \mathbf{k_f} - \mathbf{k_i}$. For the case of elastic scattering the

152

magnitudes of these wave vectors does not change and therefore the component of **q** parallel to the surface of the sample can be expressed as,

$$q_x = k\left(\cos\alpha_f - \cos\alpha_i\right)$$

where, again, $k = 2\pi/\lambda$ is the magnitude of the wave vectors. The errors in α_i and α_f can now be combined in quadrature to give an expression for the error in q_x namely,

$$\left(\Delta q_x\right)^2 = k^2\left[\sin^2\alpha_f(\Delta\alpha_f)^2 + \sin^2\alpha_i(\Delta\alpha_i)^2\right] \qquad - (7.16)$$

This derivation assumes that the wavelength dispersion, $\Delta\lambda/\lambda$ is negligible.

Consequently the full width half maximum (FWHM) of the diffraction orders at a particular sample angle can be calculated from this expression given the divergence of the incoming beam and the geometry of the detector slits where,

$FWHM(radians) = \Delta q_x \cdot \dfrac{\lambda}{4.\pi.\alpha_i}$. Figure 7.18 shows the measured FWHM of the diffraction orders in figure 7.17 with fits generated from equation (7.16). An incoming beam divergence of 15'' is assumed and the sample to detector distance is 0.78m.
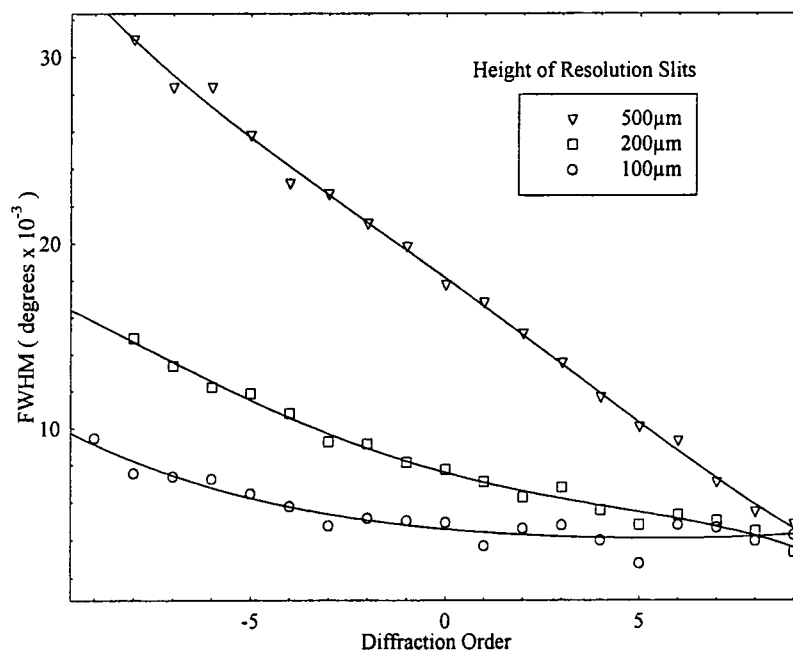

Figure 7.18 - Graph showing the measured FWHM of the various diffraction orders as a function of the detector slit height. Fitted functions are generated using equation (7.16).

As can be seen from figure 7.18 excellent agreement between experimental and simulated data is obtained using this method of analysis. Equation (7.16) can thus be used to give the correct width to the diffraction orders generated in the model of the coherent scatter. The resolution function generated from this equation was expressed as a 4th order polynomial and then convolved with the simulated data.

7.5.5 Results of the Model

The corrections, which have been just discussed, are subsequently combined with the model for the coherent scatter as presented in equation (7.11). Figure 7.19 gives an example of the simulated scatter generated using code written within the MATLAB or EXCEL environment. These curves have been generated for a GaAs grating with nominal features as presented in figure 7.2. The instrument parameters are those found experimentally at station 2.3 at Daresbury SRS with a detector slit height of 500μm and a wavelength of 1.393Å.
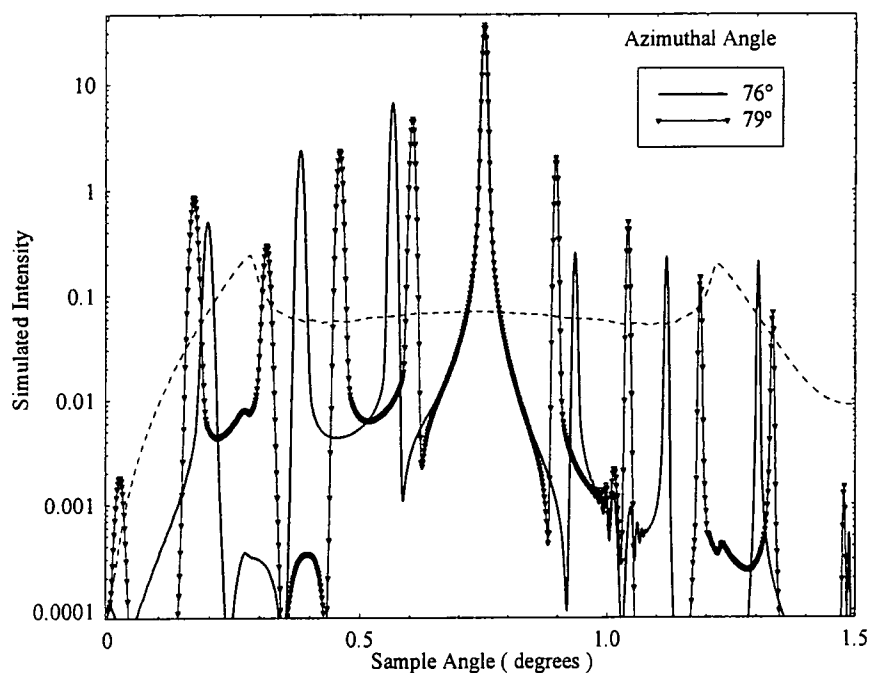

Figure 7.19 - The simulated form of the coherent scatter for two azimuthal angles. The dotted line shows the approximate level of simulated diffuse scatter for this sample.

The solid curves in figure 7.19 show the pure coherent scatter generated by the code. Sharp diffraction peaks are observed which are seen to move as the azimuthal angle of the sample is changed. Whilst the diffraction orders change upon rotation, the specular ridge (m=0 diffraction order) is not seen to change in shape, position or intensity. In addition, the width of these diffraction orders is seen to change as a function of sample angle. The level of the simulated diffuse scatter to which this coherent scatter is added is also shown. The majority of the coherent scatter lies well below the level of the incoherent diffuse scatter with just the tops of some diffraction orders showing, as observed experimentally.

When the simulated diffuse and coherent scatter are combined, the resulting simulated transverse diffuse scan in generated. A typical example of such a simulation for the GaAs grating is shown in figure 7.20.
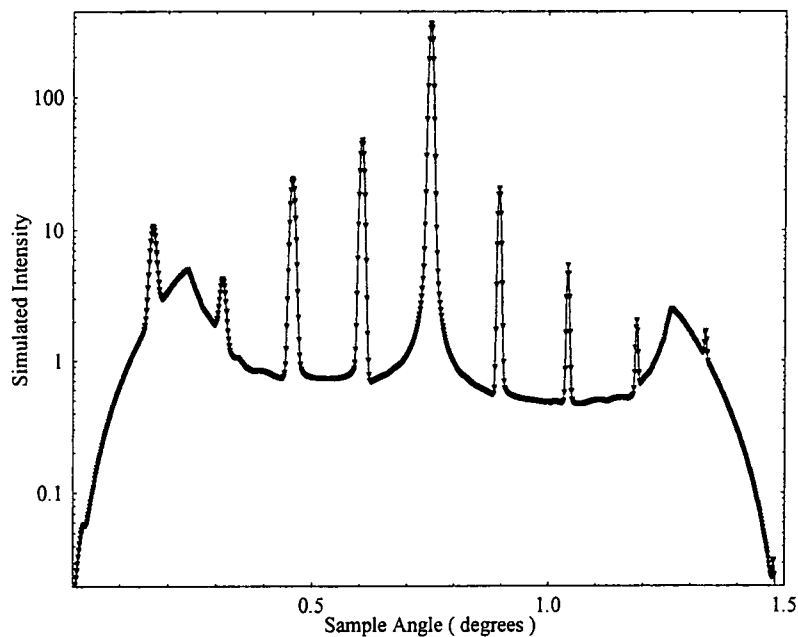
Figure 7.20 - Simulated transverse diffuse scan for a GaAs grating generated using the Bede REFS code and the model developed for the coherent scatter from a single surface.

As can be seen, the overall form of the simulated scatter closely resembles that from the GaAs grating. All the general trends observed in the experimental data are replicated in this simulation. Figure 7.21 shows the best fit simulation obtainable, using this code, for

155

the GaAs grating. The transverse scan being simulated was taken at a scattering angle of 1.6° with the detector slits set to 500μm.
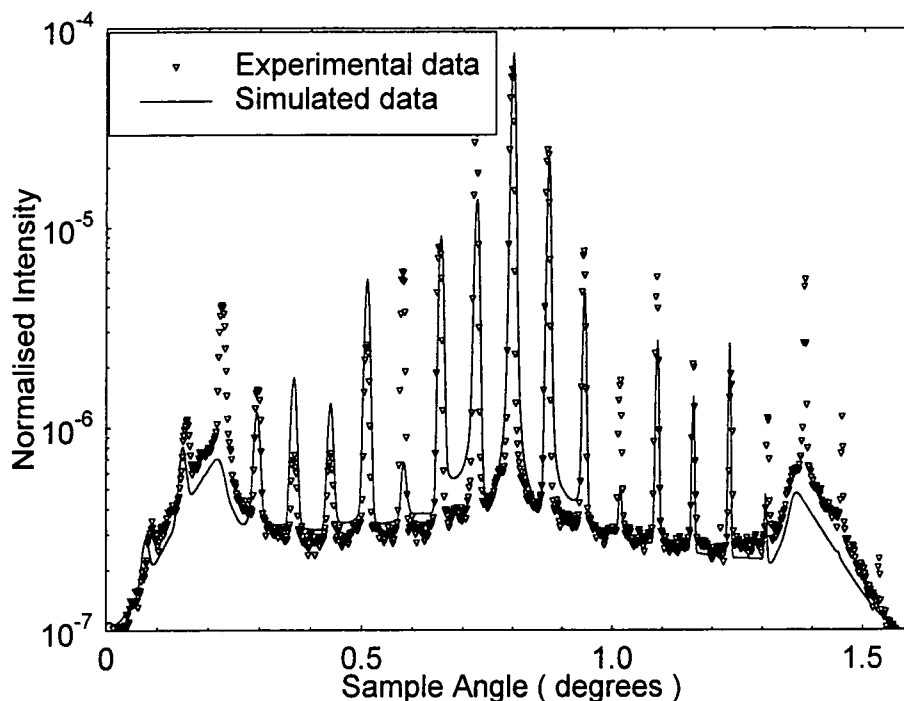

Figure 7.21 - Best fit simulation using the single surface model for the GaAs grating.

As can be seen from figure 7.21 a reasonable fit is obtained using the model for a single surface. The position and width of the diffraction orders are in excellent agreement with the experimental data and the overall shape of the diffuse scatter agrees extremely well. The problem arises when trying to match the intensities of the diffraction orders. These intensities are governed by an envelope function which is extremely sensitive to small changes in the grating function used. In the model, it was assumed that the grating had a rectangular profile. Although this is true when viewed perpendicular to the grating structure the majority of these experiments were taken close to an azimuthal angle of 90°. At such an azimuthal angle, a cross section taken along the path of the coherent x-ray beam does not result in a perfectly rectangular shape, although in any one line adjacent scattering points would lie in a straight line of apparent period d' (as was demonstrated in the ability to accurately determine the period of the grating). However, this said, the fact that in the experiment a true rectangular grating shape is not the dominant grating shape will lead to miscalculation of the envelope function.

In conclusion, therefore, it has been demonstrated that the main ideas behind this model of a single surface work. It is thought that the inability to obtain a perfect fit is due, in part, to the approximation to a rectangular structure at high azimuthal angles and also to the high intensity of the coherent scatter which results in the kinematical approximations made in the code breaking down.

7.5.6 The Addition of a Layer

Whilst the model for a single surface was used as a starting point to this discussion, the real aim was to look at the effect of depositing a single layer on such a laterally modulated surface in order to model the polymer gratings.

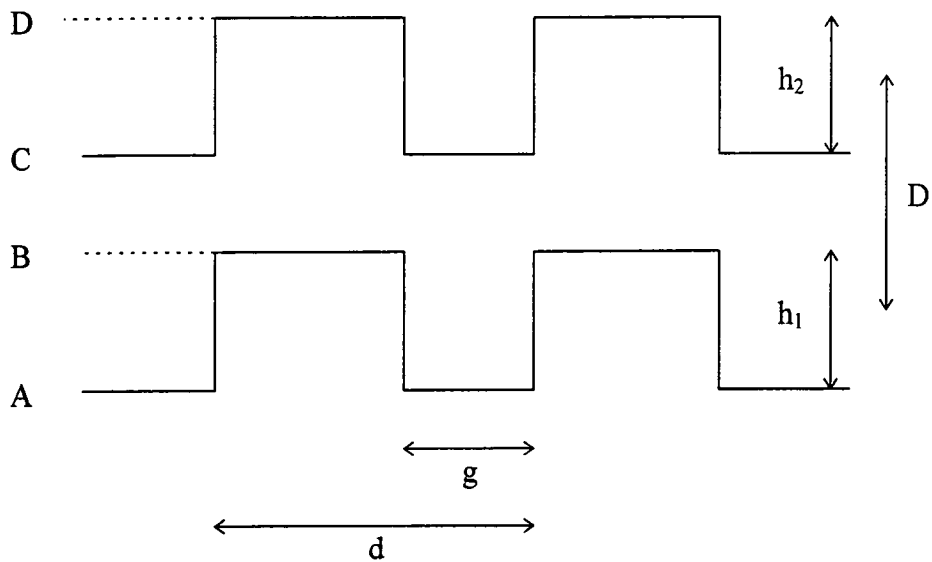Figure 7.22 - Schematic representation of the case of a single layer deposited onto a laterally modulated substrate.

Such a system is represented schematically in figure 7.22 where it is assumed both the upper and lower surfaces have a rectangular grating shape with period d and hole width g. The depth of the holes on the upper surface are h_2 and those on the substrate h_1. The mean separation of the two interfaces is D.

The effect of adding this layer to the model is, in fact, to introduce four surfaces, A, B, C, and D, into the problem. Each surface will contribute to the coherent scatter. In order to derive a model, consistent with that for a single surface, the same form of derivation is carried out where the contribution from each surface is considered in turn. The main difference in this derivation is that the values of q_z at each interface will be different due to refraction effects within the medium. The differences in q_z come about from a consideration of Snell's law at the interfaces. At the first interface there will be an angle of incidence which will be related to the transmitted angle into the next layer by the refractive index of the material. Consequently, the angle of transmittance will become the angle of incidence for the next interface and so on down the stack. These different values of q_z can therefore be calculated relatively simply using this idea. Q_x will, by definition, remain constant throughout. By definition, in this problem the values for q_z will be defined as:-

$q_z(1)$ - between surface C and D

$q_z(2)$ - between surface B and C

$q_z(3)$ - between surface A and B

As for the single surface, each interface is now considered as a series of point scatterers, located at the positions of the grating elements, and the phase difference is calculated for the entire system.

Consequently the expression for $E(q_x)$ is the same as equation (7.7), where the Fourier transform (b) has already been evaluated, namely,

$$E(q_x) = E_0 \frac{\sin N.d.\left(\frac{q_x}{2}\right)}{\sin d\left(\frac{q_x}{2}\right)}.F(q_x)$$

However in this case the expression for $F(q_x)$ is more complex as it involves a contribution from each of the 4 interfaces. Now,

$$F(q_x) = f_A(q_x) + f_B(q_x) + f_C(q_x) + f_D(q_x)$$

where,

$$f_A(q_x) = \int_{-g/2}^{g/2} \exp(-i.q_x.x)dx$$

$$f_B(q_x) = \left[\exp(i.h_1.q_z(1))\right]\left[\int_{g/2}^{d/2} \exp(-i.q_x.x)dx + \int_{-g/2}^{d/2} \exp(-i.q_x.x)dx\right]$$

$$f_C(q_x) = \left[\exp\left\{i\left(d + \frac{h_1}{2} - \frac{h_2}{2}\right)\right\}q_z(2)\right] \cdot \left[\int_{-g/2}^{g/2} \exp(-i.q_x)dx\right]$$

$$f_D(q_x) = \left[\exp\left\{i\left(d + \frac{h_1}{2} + \frac{h_2}{2}\right)\right\}q_x(3)\right] \cdot \left[\int_{g/2}^{d/2} \exp(-i.q_x)dx + \int_{-d/2}^{-g/2} \exp(-i.q_x x)dx\right]$$

These integrals are the same as those for the single surface with an additional phase factor in front of them. Each integral describes the particular surface it is representing.

After lengthy manipulation, a final expression for $I(q_x, q_z)$ is obtained, namely,

$$I(q_x, q_x) = \left|R_f(q_z)\right|^2 \cdot \frac{2}{N^2} \cdot \frac{\sin^2(N.d.\frac{q_x}{2})}{\sin^2(d.\frac{q_x}{2})} \cdot (T + S) \quad - (7.17)$$

where,

$$T = A^2 + B^2 + A(B\cos(E) + A\cos(F) + B\cos(G))$$

$$S = B(A\cos(E - F) + B\cos(E - G) + A\cos(F - G))$$

$$A = \frac{1}{g} \cdot \frac{\sin(g.\frac{q_x}{2})}{\frac{q_x}{2}}$$

$$B = \frac{1}{(d-g)} \cdot \left[\frac{\sin(d.\frac{q_x}{2}) - \sin(g.\frac{q_x}{2})}{\frac{q_x}{2}}\right]$$

$$E = h_1.q_z(3)$$

$$F = h_1.q_z(3) + (D - \frac{h_1}{2} - \frac{h_2}{2}).q_z(2)$$

$$G = h_1.q_z(3) + (D - \frac{h_1}{2} - \frac{h_2}{2}).q_z(2) + h_2.q_z(1)$$

Once again a program has been written which evaluates this expression for particular values of q_x and q_z using the package MATLAB. All the additional correction terms which were described for a single surface still apply and are included into this model accordingly.

One further correction which is taken into account in this code is that of absorption. In the case of a single layer it is not necessary to account for this effect whereas for a layer it is crucial. The absorption coefficient for the particular material is calculated [39] and the absorption occurring over the path length of the x-rays through that particular material evaluated. This correction is then included into the model so that the scatter from the buried interfaces will have been modified.

7.5.6.1 Result of the Code

Initially a comparison of this new code was made with that calculated for a single surface. Values of h_1, h_2 and D were chosen such that an approximation was made for a single surface in the layered model (i.e. $h_1 = 0$, $h_2 = 5000$Å and $D = 100000$Å). All experimental parameters were kept the same between the two models. Figure 7.23 shows the comparison of the coherent scatter from the two models.
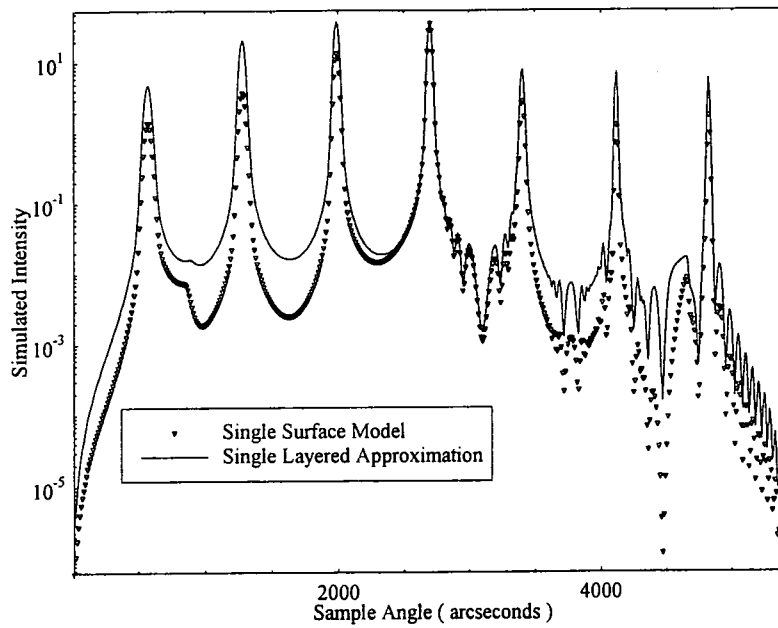
Figure 7.23 - Comparison of the coherent scatter between the single surface model and the layered model, approximated to a single surface.

As can be seen from figure 7.23 good agreement is obtained between the models in this approximation. This suggests that the model for the layer on a laterally modulated surface is indeed giving the correct form of the coherent scatter.

The code has been used to model the transverse diffuse scans taken on the polymer gratings. Figure 7.24 shows the best fit simulation obtained, using this code, for the single layer of polymer deposited on the laterally modulated photoresist.

The model used to generate this scatter assumes a grating structure, as in figure 7.22, with the parameters,

$$g = 15000\text{Å}$$
$$d = 78100\text{Å}$$
$$D = 7000\text{Å}$$
$$h_1 = 100\text{Å}$$
$$h_2 = 510\text{Å}$$

These values for d and g correspond to a grating with period 4018Å and a hole width of 777Å at an azimuthal angle of 87°.

In addition the thickness of the layer used was the same as that used to generate the diffuse scatter in the Bede REFS code. This code also assumed a fractal parameter of 0.2, a lateral correlation length of 1200Å and a r.m.s surface roughness, σ, of 35 ± 5Å.
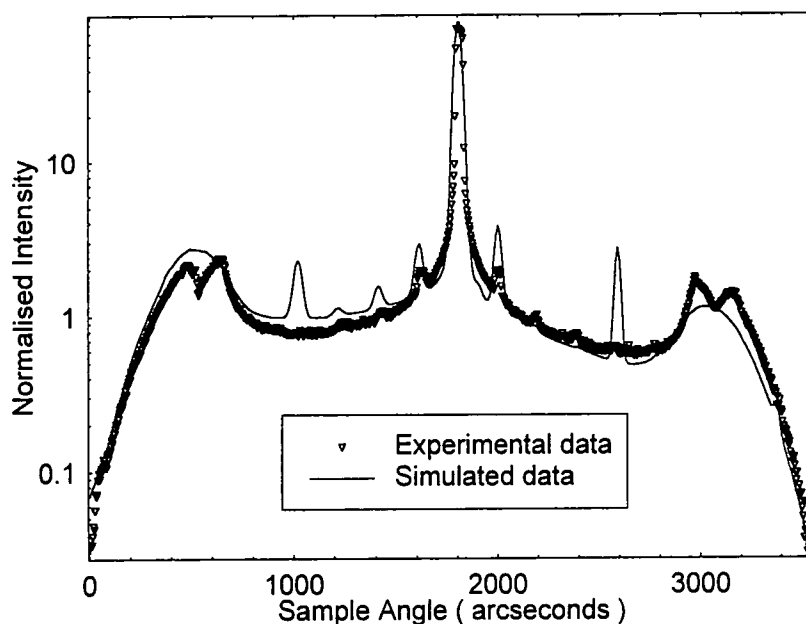
Figure 7.24 - Best fit simulation, obtained using the model of a single layer, to the transverse diffuse scatter from the polymer grating.

As can be seen from figure 7.24 the agreement between experimental and simulated data using this model is far from perfect. As in the case of the single surface the positions and widths of the diffraction orders are reproduced accurately in the simulated data. The problem again lies in the modulation of the intensities of the orders as a function of sample angle. It is found that the shape of the coherent scatter is extremely sensitive to small changes in the sample parameters, namely d and g, thus making it very difficult to find a simulation which is truly at a global minimum.

Once again, the main reason why this model fails is almost certainly due to the approximation of a rectangular grating. Whilst, for the GaAs grating, it could be considered a reasonable approximation it is much less valid in the case of the layered samples where, from a study of the AFM images of the surface, it can be seen that the actual form is much more corrugated in nature.

This said, it is possible to use this model to obtain certain information about the sample being studied. The shape of the incoherent diffuse scatter, generated using the REFS software, fits well to the experimental data giving a firm indication of the surface roughness, σ, and both the lateral correlation length, ξ and the fractal parameter h. It must be assumed that such parameters are representative of the surface of the grating elements.

Fitting the position of the diffraction orders gives an accurate value for the period of the grating and the range of the hole width, g, can be tied down to $\pm$ 10%, as outside of this range the shape of the coherent scatter deviates strongly from that of the experimental. The values for D, h_1 and h_2 are much more difficult to obtain accurately as the model is extremely sensitive to small changes in these parameters. It is still possible, however, to narrow the values of these parameters down to a physically realistic range using this model and, for example, comparing the value of D with that obtained from the REFS simulation

7.6 Conclusions

A large range of high quality experimental data has been taken on a variety of laterally modulated structures. These data have been successfully analysed to determine accurately the period of these grating structures. A semi-kinematical code has been developed in an attempt to model the coherent scatter from both a laterally modulated single surface and a layered system. As well as addressing the coherent scatter from the sample, the effects of coherence and instrument resolution have been comprehensively included in a simple but realistic manner. The fit between the output of this code and experiment is not completely successful. However, the period and hole width of such structures can be accurately determined from these simulations as can the thickness of the layer and the depths of the holes, albeit to a lesser degree of accuracy.

Since the majority of the key features in the experimental data are reproduced accurately by this model, for example peak positions, peak widths and the general 'form' of the scatter, it can be concluded that the basis behind the code is justified. The failure of the

model has been attributed, in part, to an unrealistic approximation of the grating structure and it is thought that through a more complex analysis of this shape function, a far more realistic model could be achieved and used to model successfully the scatter from such laterally modulated structures.

References for Chapter 7

[1] Y. W. Zhang, L. S. Sheng, G. B. Zhang, H. Gao J. Synch. Rad. **5** (3) *559* (1998)

[2] F. Senf, K. J. S. Sawheny, R. Follath, M. Scheer, F. Schafers, J. Bahrdt, A. Gaupp, W. Gudat J. Synch. Rad. **5** (3) *747* (1998)

[3] M. A. Holland, J. Q. Harrington, M. I. Weston Rev. Sci. Intrs. **63** (1 - Pt. 2b) *1274* (1992) and http://srs.dl.ac.uk/XUV-VUV/12.html

[4] L. Vanzi, M. Sozzi, G. Marcucci, A. Marconi, F. Mannucci, F. Lisi, L. Hunt, E. Giani, S. Gennari, V. Biliotti and C. Baffa Astron. Astrophys. Suppl. Ser. **124** *573* (1997)

[5] J. W. Brosius, J. M. Davila, R. J. Thomas Astrophys. Journ. **497** (2 - Pt. 2) *L113* (1998)

[6] D. D. C. Bradley Current Opinions in Solid State and Materials Science **1** *789* (1966)

[7] N. C. Greenham Adv. Mat. **6** (6) *491* (1994)

[8] B. J. Matterson, M. G. Salt, W. L. Barnes and I. D. W. Samuel Synthetic Metals **101** (1-3) *250* (1999)

[9] A. T. Macrander and S. E. Slusky Appl. Phys. Lett. **56** *443* (1990)

[10] L. Tapfer and P. Grambow Appl. Phys. A **50** *3* (1990)

[11] M. Gailhanou, T. Baumbach, U. Marti, P. C. Silva, F. K. Reinhart and M. Ilegems Appl. Phys. Lett. **62** (14) *1623* (1993)

[12] V. V. Aristov, A. I. Erko, A. Yu. Nikulin and A. A. Snigerv Opt. Commun. **58** *300* (1986)

[13] V. V. Aristov, A. Yu. Nikulin. A. A. Snigerv and P. Zaumseil Phys. Status Solidi A **95** *81* (1986)

[14] V. V. Aristov, U. Winter, A. Yu. Nikulin, S. V. Redkin, A. A. Snigerv, P. Zaumseil and V. A. Yunkin Phys. Status Solidi A **108** *651* (1988)

[15] P. van der Sluis, J. J. M. Binsma and T. van Dongen Appl. Phys. Lett. **62** *3186* (1993)

[16] M. Tolan, W. Press, F. Brinkop and J. P. Kotthaus J. Appl. Phys. **75** (12) *7761* (1994)

[17] M. von Laue Ann. Phys. (Leipzig) **26** *55* (1936)

[18] S. R. Andrews and R. A. Cowley J. Phys. C **16** *6427* (1985)

[19] I. K. Robinson Phys. Rev. B **33** *3830* (1986)

[20] A. T. Macrander, E. R. Minami and D. W. Berreman J. Appl. Phys. **60** *1364* (1986)

[21] M. Tolan, D. Bahr, J. Sussenbach, W. Press, F. Brinkop and J. P. Kotthaus Physica B **198** *55* (1994)

[22] T. Salditt, H. Rhan, T. H. Metzger, J. Peisl, R. Schuster, J. P. Kotthaus Z. Phys. B **96** *227* (1994)

[23] M. Tolan, W. Press, F. Brinkop and J. P. Kotthaus Phys. Rev. B **51** (4) *2239* (1995)

[24] M. Tolan, G. Vacca, S. K Sinha, Z. Li, M. H. Rafailovich, J. Sokolov, H. Lorenz and J. P. Kotthaus Appl. Phys. Lett. **68** (2) *191* (1996)

[25] M. Tolan, G. Vacca, S. K Sinha, Z. Li, M. H. Rafailovich, J. Sokolov, H. Lorenz and J. P. Kotthaus J. Phys. D **28** *A231* (1995)

[26] P. Mikulik - PhD thesis 1997

[27] P. Mikulik and T. Baumbach Phys. Rev. B **59** (11) *7632* (1999)

[28] T. Baumbach and D. Lubbert J. Phys. D **32** (6) *726* (1999)

[29] P. Mikulik and T. Baumbach Physica B **248** *381* (1998)

[30] I. D. W. Samuel Synthetic Metals **84** *497* (1997)

[31] M. Tolan, G. Konig, L. Brugemann, W. Press, F. Brinkop and J. P. Kotthaus Europhys. Lett. **20** (3) *223* (1992)

[32] I. Pape *et al* Submitted to Phil. Mag A

[33] I. Pape - PhD Thesis, University of Durham (1997)

[34] X-Ray Science and Technology - ed. A. G. Michette and C. J. Buckley (IOP) 1993 - chap. 8

[35] Principles of Optics - Born and Wolf (Pergamon Press) 1959

[36] S. K. Sinha, M. Tolan, A. Gibaud Phys. Rev B **57** (5) *2740* (1998)

[37] Photoemission and Absorption in Solids and Interfaces with Synchrotron Radiation - B. Lengeler (North Holland) 1990

[38] A. Gibaud, J. Wang, M. Tolan, G. Vignaud and S. K. Sinha J. Phys. I France **6** *1085* (1996)

[39] http://www-cxro.lbl.gov/optical_constants/

Chapter 8 - Summary and Outlook for Further Work

In this chapter the salient points of the entire thesis are summarised and possible directions for future work, following on from the studies presented here, are suggested.

8.1 Summary

The underlying theme of this thesis has been the use of x-ray scattering techniques to study the effect of depositing thin film samples on surfaces which have some form of periodic structure, as well as studying such surfaces directly. As it has been shown, such a growth method can lead to significant changes in the macroscopic properties of the samples in question. Through detailed study of the surfaces and interfaces of these samples, subtle changes in sample properties have been linked to changes in the magnetic properties of thin granular films and spin-valve systems, and the photoluminescent properties of thin film polymers.

Chapter 4 introduced a series of CoAg, granular thin films which were studied in both chapters 4 and 5. Using high angle diffraction techniques, the evolution of the Co grains within the Ag matrix was observed as a function of Co concentration. Detailed analysis of the out-of-plane size of the Co crystallites was compared with the measured amount of Co diffracting from the samples. It was concluded that the Co crystallites were growing preferentially along the plane of the film, as more Co was added to the system, and this conclusion was backed up by measurements of grain size and strain within the Ag matrix. This proposed growth method was further supported by detailed magnetic measurements made on the samples. Since such materials could potentially form the basis for high density media storage materials, the ability to characterise satisfactorily their growth mechanisms is clearly crucial.

In chapter 5 grazing incidence scattering studies were performed on this same series of granular films in order to determine accurately their thickness and roughness. In studying the diffuse scatter from these samples it was observed that there was an asymmetry present in the diffuse scatter. A detailed investigation of this asymmetry was carried out on the pure Ag film as this possessed the simplest structure for modelling. It was seen that the diffuse scatter was actually offset from the specular condition and that the position of this offset varied sinusoidally upon rotation of the sample about its azimuthal axis. The observed behaviour was explained in terms of step-bunching of the Si (111) substrate where long, flat terraces were interspersed with bunches of atomic steps where the steps were at an angle to the average surface. After modifications had been made to the commercial Bede code which is used for modelling the diffuse scatter, the offset was accurately simulated and the results agreed with the qualitative physical interpretation. Since the step-bunching of Si (111) can be a very useful method of changing the properties of a thin film deposited onto it, the ability to measure this phenomena non-destructively, after deposition, is clearly important.

Chapter 6 took the theme a step further by examining the effect of depositing spin-valve structures onto a variety of Si substrates. In particular, the effect of depositing such devices onto Si substrates similar to those used in the Si processing industry was investigated. Such substrates were seen to be very rough and tiled in a periodic manner. Detailed analysis of the experimental data taken from both the bare substrates and deposited films, showed that out-of-plane, conformal roughness dominated such systems. Consequently, the roughness and nature of the substrate used was of critical importance since it was seen that the nature of the substrate roughness propagated up through the deposited layers. The x-ray data were related to magnetic measurements taken on the samples and it was seen that the proposed growth mode was entirely consistent with the magnetic behaviour observed from the samples. The work concluded that if spin-valves were to be deposited onto such rough, Si substrates for commercial applications, measures would have to be taken to reduce the effect of the highly conformal roughness.

Chapter 7 investigated the nature of laterally modulated surfaces, and thin films deposited onto them, in much greater detail. It had been observed that light emitting polymer films, deposited onto laterally modulated substrates, underwent strong

modifications in their photoluminescence spectra. Detailed analysis of these samples along with samples of the bare, laterally modulated substrate, were undertaken. From these measurements the period of the grating structures were determined very accurately and seen to be in excellent agreement with AFM images. In order to model further the propagation of the lateral modulations, and shorter length-scale roughness, from the substrate through the deposited film, it was necessary to model the coherent scatter. To do this, existing scattering theory was modified and a semi-kinematical code developed. In addition to considering the coherent scatter, the model also included detailed instrumental resolution functions which were obtained in a mathematically simple way and were in excellent agreement with the experimental data. A model, which also included the incoherent diffuse scatter, was developed for a single surface and attempts were made to match this model to experimental data taken from an almost ideal, GaAs, etched grating. Reasonable agreement was seen between the model and the experimental data, the model being extended to include a single layer deposited onto a modulated substrate. Although it was found that some modifications would have to be made to the code to get a fully satisfactory fit to the experimental data, the model allowed the period and hole width of the grating to be determined very accurately along with the surface roughness and both the fractal parameter and lateral correlation length of the surface.

8.2 Further Work

Following on from the work undertaken in these chapters two key areas of further work present themselves. Firstly, the use of spin-valves in magnetic sensors is a rapidly growing area with many important, technological applications already being available. If, however, spin-valves are to be incorporated usefully into Si integrated circuits, further work has to be undertaken to reduce the inherent coupling between the magnetic layers highlighted in these studies. One possible approach to this problem would be the use of surfactants. It is known that the use of, say indium, as a surfactant, can lead to a reduction in the coupling between the magnetic layers. It would be interesting to see if this could be applied to the spin-valve systems studied here and whether the overall conformality of the roughness was reduced by the use of the surfactant. In addition, the studies presented here highlight the fact that although it is possible to infer the

roughness of the buried interfaces from knowledge of the initial substrate and final surface roughness and how that roughness propagates, it is not possible to obtain individual layer characteristics. This is due to the very close scattering powers of the constituent layers. It was suggested, in chapter 6, that one way of tackling this problem was to incorporate grazing incidence scattering measurements with depth sensitive fluorescence. Whilst it has been demonstrated already, in the group at Durham University, that this can lead to determination of individual layer thickness no measurements have been made, to date, on specific layer roughness. If in combing these two techniques, possibly with very energy specific scattering experiments, it was found to be possible to determine individual layers roughness, this would open up a key area of research with many technologically important applications. Additionally, it may be possible to obtain this information through the use of grazing incidence neutron scattering. Since the scattering powers for neutrons are different to those of x-rays the problems of indistinguishability would not arise. It may also be possible to observe the magnetic structure of these samples if polarised neutron scattering were used.

The second area for further work, which follows on logically from this thesis, is the study of laterally modulated structures and in particular the polymer samples which were discussed extensively in chapter 7. It has been shown throughout the thesis the pronounced effect that depositing samples on a laterally modulated structure can have on the properties of the sample, so the motivation for further work in this area is great. The model which was developed in chapter 7 to simulate the coherent scatter from such grating structures failed to reproduce satisfactorily the exact form of the experimental data. However, all the trends and major features seen in the experimental scatter were reproduced with a high degree of accuracy. This suggests that the basis for the code is not without foundation and only minor changes to the way in which it is used would be necessary to simulate accurately experimental data from such structures. The first modifications to the code must certainly be in the shape factor used to describe the grating structure. Whilst a simple rectangular grating shape was used throughout the models, detailed images of the sample surface indicate that, certainly in the case of the polymer, this is not an accurate representation of the samples surface. Since this form factor strongly governs the shape of the overall envelope function of the coherent scatter (and this was where the model was really seen to fail) subtle changes in the exact shape function used could lead to an accurate model being developed. With the ability then, to

describe the coherent scatter in an simple and non-mathematically involved way, and combine it with a model for the diffuse scatter, the potential to model the propagation of both large and short scale roughness modulations through a deposited sample is great, with many immediately obvious applications.

In summary, therefore, it has been demonstrated, throughout this thesis, that x-ray scattering techniques offer a unique and powerful, non-destructive method to accurately probe the surface and buried interface structure of thin film samples. Since such parameters have been shown to play a key part in determining the properties of various materials for potential applications, the need to continue developing and furthering the accuracy of the experimental techniques and modelling procedures has never been greater.